

**Carnegie Mellon University**  
**MELLON COLLEGE OF SCIENCE**

**THESIS**

SUBMITTED IN PARTIAL FULFILLMENT OF THE REQUIREMENTS  
FOR THE DEGREE OF

**DOCTOR OF PHILOSOPHY IN THE FIELD OF PHYSICS**

TITLE: "Lambda Baryon Spectroscopy and Pion-Pion Scattering with Partial Wave  
Mixing in Lattice QCD"

PRESENTED BY: Jacob Fallica

ACCEPTED BY THE DEPARTMENT OF PHYSICS

COLIN MORNINGSTAR	09/12/18	
COLIN MORNINGSTAR, CHAIR PROFESSOR		DATE

SCOTT DODELSON	09/15/17	
SCOTT DODELSON, DEPT HEAD		DATE

APPROVED BY THE COLLEGE COUNCIL

REBECCA DOERGE	09/22/17	
REBECCA DOERGE, DEAN		DATE

# **Lambda Baryon Spectroscopy and Pion-Pion Scattering with Partial Wave Mixing in Lattice QCD**

by  
Jacob Fallica

Submitted in partial fulfillment of the  
requirements for the degree of  
Doctor of Philosophy  
at  
Carnegie Mellon University  
Department of Physics  
Pittsburgh, Pennsylvania

Advisor: Colin Morningstar

September 15, 2017

# Abstract

The spectrum of  $\Lambda$  three-quark excitations and  $\pi\pi$  scattering, with partial-wave mixing, are studied using lattice QCD. These low-lying stationary-state energies in QCD are calculated as correlation lengths in a statistical field theory. Monte Carlo methods with importance sampling estimate the multidimensional path integral, with 412 gauge configurations generated according to a clover-improved Wilson action with  $2 + 1$  flavors of quarks. A matrix of single- and multi-hadron correlators is used to extract excited-state energies in the  $\Lambda$ -flavored isoscalar strange symmetry channels. Replacing infinite-volume spin are irreps of the double-point-octahedral group; in this case  $G_{1g}, G_{1u}, H_g$  and  $H_u$ . Dirac matrix inverses on a  $32^3 \times 256$  lattice and a pion mass of  $\approx 240$  MeV are estimated with the stochastic LapH (Laplacian-Heaviside) method. A generalization of the Luscher quantization condition is used to relate  $\pi\pi$ -energies in finite volume to a  $\pi\pi$ -scattering  $K$ -matrix. The width and mass of the  $\rho(770)$  are determined using a relativistic Breit-Wigner parametrization of the  $K$ -matrix. This parametrization allows for nonzero  $L = 1, 3$  and  $5$  partial waves. The formalism used completely generalizes to multiple inelastic channels and non-identical particles of nontrivial spin.

# Dedication

For my partner, Gabrielle Tiede, and for my mother, Nancy Lewin.

This work would not be possible without my dear colleagues and fellow graduate students, especially Andrew Hanlon, Ben Hörz and Ruairí Brett. Anything I know, I know only after extensive discussion with these individuals.

Finally, I wish to thank my advisor, Professor Colin Morningstar, for the immeasurable help and insight for this research, and particularly the concept of renormalization.

# Contents

<b>1</b>	<b>Introduction</b>	<b>1</b>
1.1	Correlation Functions . . . . .	1
1.2	Perturbation Theory . . . . .	2
1.3	Lattice Field Theory . . . . .	3
1.4	QCD, Hadrons, and Quarks . . . . .	4
1.5	Spectroscopy and Scattering . . . . .	6
<b>2</b>	<b>Lattice QCD Lagrangian</b>	<b>8</b>
2.1	The QCD Lagrangian . . . . .	8
2.1.1	The Fermionic Sector . . . . .	8
2.1.2	Gauge Invariance . . . . .	10
2.1.3	The Bosonic Sector . . . . .	11
2.1.4	Wick-Rotating the QCD Lagrangian . . . . .	12
2.2	Naive Discretization . . . . .	13
<b>3</b>	<b>Action Improvement</b>	<b>15</b>
3.1	Fermion Doubling . . . . .	15
3.1.1	Wilson Fermions . . . . .	16
3.2	Symanzik Improvement . . . . .	17
3.3	Tadpole Improvement and Stout Smearing . . . . .	17
3.4	Anisotropic Improved Action . . . . .	18
3.5	Parameter Tuning . . . . .	20
3.5.1	Heavy Pion . . . . .	20
3.5.2	Anisotropy . . . . .	21
3.5.3	Gauge-coupling . . . . .	21

<b>4</b>	<b>Operator Construction</b>	<b>23</b>
4.1	Single Hadrons . . . . .	23
4.1.1	Elemental Components . . . . .	23
4.1.2	Covariant Displacements . . . . .	24
4.1.3	Hermiticity . . . . .	25
4.1.4	Stout Smearing . . . . .	28
4.1.5	Quark Smearing . . . . .	29
4.1.6	Basic Building Blocks . . . . .	30
4.2	Symmetries . . . . .	31
4.2.1	Flavor Structure . . . . .	31
4.2.2	G-Parity . . . . .	33
4.2.3	Time-Reversal . . . . .	34
4.2.4	Cubic Symmetry . . . . .	36
4.2.5	Moving Frames . . . . .	38
4.2.6	Projection onto Symmetry Sectors . . . . .	38
4.3	Multi-Hadron Operators . . . . .	40
<b>5</b>	<b>Monte Carlo Sampling</b>	<b>42</b>
5.1	Fermions and Correlators . . . . .	42
5.1.1	Matrix Inversion . . . . .	44
5.1.2	Noise Dilution . . . . .	45
5.1.3	Factorization . . . . .	45
5.2	Importance Sampling . . . . .	47
5.3	Configuration Generation . . . . .	48
5.3.1	Markov Chains . . . . .	48
5.3.2	Hybrid Monte Carlo . . . . .	50
<b>6</b>	<b>Correlator Analysis</b>	<b>53</b>
6.1	Excited States . . . . .	53
6.2	Single Rotation . . . . .	54
6.3	Pruning . . . . .	56
6.4	Overlaps . . . . .	57
6.5	Temporal Wrap-Around . . . . .	58
6.6	Fitting . . . . .	58
6.6.1	Fit Forms . . . . .	58

6.6.2	Statistical Error . . . . .	59
6.6.3	Correlated Fits . . . . .	60
<b>7</b>	<b>Phase Shifts and the Luscher Method</b>	<b>62</b>
7.1	Luscher Quantization Condition . . . . .	62
7.2	K-matrix Method . . . . .	68
7.3	The Box Matrix . . . . .	68
7.4	Fitting . . . . .	70
<b>8</b>	<b>Results</b>	<b>71</b>
8.1	Computational Details . . . . .	71
8.2	$G_{1g}$ Spectrum on $32^3 \times 256$ . . . . .	72
8.3	$G_{1u}$ Spectrum on $32^3 \times 256$ . . . . .	81
8.4	$H_g$ Spectrum on $32^3 \times 256$ . . . . .	90
8.5	$H_u$ Spectrum on $32^3 \times 256$ . . . . .	99
8.6	$\pi\pi$ Scattering Results . . . . .	106
<b>9</b>	<b>Conclusion</b>	<b>116</b>

# Chapter 1

## Introduction

### 1.1 Correlation Functions

Quantum field theory and the Standard Model of particle physics have been enormously successful at describing the various processes seen in accelerator experiments and cosmic rays. The key concept is that fields and physical states act as carrier spaces for representations of fundamental symmetries of nature. Lorentz symmetry allows particles to carry properties like mass and spin, with other quantum numbers like electric charge dictated by internal symmetries.

These fields are organized into an action  $S$ , and any particular field history has a probability amplitude of  $e^{iS/\hbar}$ . In the limit of vanishing  $\hbar$ , only those fields satisfying the equations of motion add constructively, reproducing classical mechanics. Quantum corrections are the nonzero contributions that appear for nonvanishing  $\hbar$ . In this regard quantum physics is like thermal physics, with a unimodular probability amplitude rather than a real probability weight. Both types of fluctuations are regarded as statistical:

$$\begin{aligned}\langle 0|\hat{A}|0\rangle &= \frac{1}{Z}\mathrm{Tr}Ae^{iS/\hbar}, \\ \langle A\rangle &= \frac{1}{Z}\mathrm{Tr}Ae^{-H/T}.\end{aligned}\tag{1.1}$$

The basic questions of quantum mechanics, such as “what are the stationary states” and “what are their energies,” amount to solving for moments and correlation functions using this statistical distribution. For example, the mass of a particle is identified not with a parameter  $m$  appearing in  $S$ , but with the location of a pole in

a two-point correlation function:

$$\langle 0 | \hat{\phi}(\mathbf{p}) \hat{\phi}^\dagger(\mathbf{p}) | 0 \rangle \sim \frac{i}{p^2 - m^2}. \quad (1.2)$$

## 1.2 Perturbation Theory

The usual strategy pursued is perturbative. That is, the full theory is treated as a small perturbation to an exactly solvable free theory and corrections to this solution approximate the full solution as a power series in the coupling. For some field theories, often when the coupling is small, this method is able to produce very nearly exact results. The usual example is Quantum Electrodynamics (QED), the theory of how photons interact with charged particles, where the power series is in terms of the very small parameter  $\alpha$ , which is  $\sim \frac{1}{137}$  at typical energies.

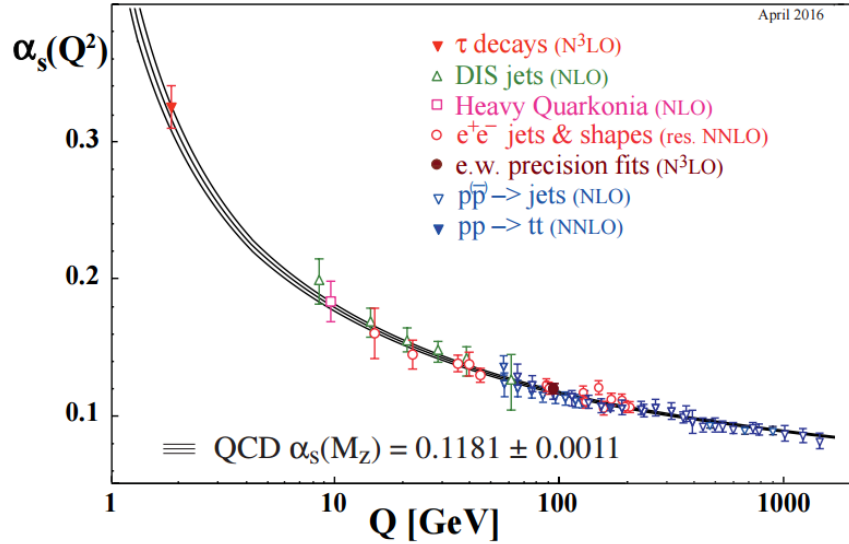


Figure 1.1: Running of the strong coupling with energy. Level of perturbation theory used is given in parentheses. [1]

It is often the case, however, that the relevant coupling parameter is *not* small, and corrections in the perturbative series grow in magnitude rather than shrink. The coupling, as defined by a three-point correlation function, actually changes with energy so it is even possible that a theory which is perturbative in one energy range

could be nonperturbative in another. We have already mentioned QED, which is weakly coupled at low energies but seems strongly coupled at higher energies; a theory satisfying the reverse situation, strongly coupled at low energies but weakly coupled at high energies, can be found in QCD, or Quantum Chromodynamics [2] [3]. In order to calculate in a regime of strong coupling, we need a nonperturbative approach.

## 1.3 Lattice Field Theory

When perturbation theory is not sufficient, we can resort to approximating the integral with Monte Carlo sampling. It is not easy to define a discrete version of the action  $S$  amenable to computer calculation, and even harder to prove that it converges properly as the discretization is made progressively smaller. This discretized theory is known as a lattice field theory. In spite of the hurdles, these computational strategies provide the most rigorous definition of many quantum field theories.

Energies correspond to the frequencies in the Fourier transform of temporal correlators, which become decay rates when we Wick-rotate into imaginary time:

$$\begin{aligned}\langle 0|\hat{A}(t)\hat{B}^\dagger(0)|0\rangle &= \sum_n \langle 0|\hat{A}|n\rangle \langle n|\hat{B}^\dagger|0\rangle e^{-iE_n t} \\ &\Rightarrow \sum_n Z_A^n Z_B^{n*} e^{-E_n \tau}.\end{aligned}\tag{1.3}$$

Such a rotation is necessary for  $e^{-S}$  to be used as a probability weight in Monte Carlo sampling. A particular correlator gives rise to a functional in the Monte Carlo integrand; the value of this functional is importance-sampled according to  $e^{-S}$ . In order to extract multiple energies we form a large matrix of correlators, where each entry corresponds to the average of some  $O[\phi]$  weighted by  $e^{-S}$ . We calculate this average by generating a random set of configurations  $\phi$  distributed according to  $e^{-S}$ , accomplished with a stochastic Markov chain, designed so that its fixed point corresponds to this distribution.

Bosonic variables produce functionals which can be directly related to the fundamental fields in the action because the corresponding variables of integration are complex number-valued. Fermionic variables, however, are anticommuting, so it is more difficult to relate their ultimately complex-valued integrands to the Grassmann-valued fundamental fields. Fortunately, the quark fields appear quadratically in the

action as  $\bar{\psi}M\psi$  so the integration over these fields can be done exactly. The integral over the gauge variables  $G$  remains, with probability weight  $\det M[G]e^{-S_g[G]}$ ; integrating the fermions gives rise to a matrix determinant, and quark fields in correlators leave behind elements of a matrix-inverse  $M^{-1}[G]$  in the integrand. This is a prodigiously large matrix and it is computationally infeasible to compute it exactly, for each set of gauge variables  $G$ . Instead we implement a novel stochastic method, Stochastic LapH, to evaluate these objects efficiently on large lattices [4] [5].

## 1.4 QCD, Hadrons, and Quarks

In QED, the fundamental quantities are photons, and charged particles like electrons and positrons. We will also consider protons, which from the perspective of low-energy QED are not too dissimilar from heavy positrons. We commonly find these objects bound together, into positronium or hydrogen. Inside this proton is the realm of QCD. There, the fundamental degrees of freedom are gluons, quarks and antiquarks; these entities are analogous to the QED particles. In the language of symmetry groups, the matter-type particles like electrons and quarks transform in the fundamental representation of a local  $U(1)$  or  $SU(3)$ -gauge symmetry whereas the photons and gluons transform in the adjoint representation of the local gauge symmetry group [6]. Just as the fundamental constituents of QED form bound states of positronium or hydrogen, the proton is itself a bound state of quarks and gluons. Neutrons are the same way, as are every strongly-interacting particle seen in accelerators and cosmic rays.

So, QCD controls the formation of these particles, as well as the interactions among them. Hundreds of years ago, Kepler believed that the mysteries of the cosmos could be explained by nesting platonic solids in spheres. Now, we describe the patterns of observed hadrons (baryons and mesons) by using representations of an  $SU(3)$ -flavor symmetry [7] [8], found by *e.g.* stacking triangles on top of each other (see Figure 1.2).

The  $SU(3)$ -flavor symmetry arises from the near degeneracy of the up, down and strange quark masses, compared to typical energy scales of the hadrons they form. This symmetry dictates their general behavior, responsible for the similarities and differences between a pion and a kaon (both mesons in the octet) or a proton and a lambda (both baryons in the octet). We might write these in the form of fields

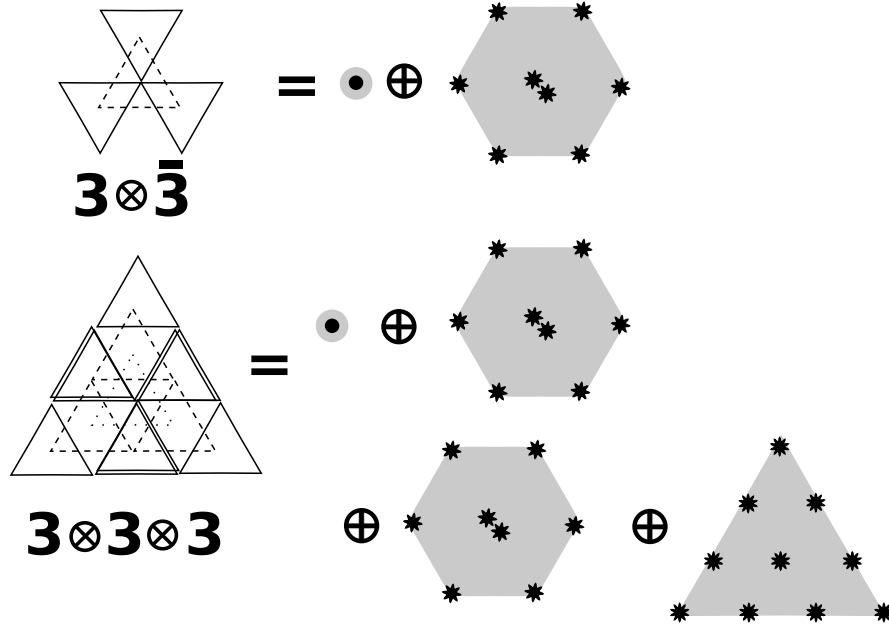


Figure 1.2: (Top) Tensor product of fundamental (quark) and antifundamental (antiquark) representations decomposes into nine light mesons. (Bottom) Tensor product of three quarks decomposes into eight states of spin-1/2 and ten of spin-3/2. Overall antisymmetry prevents a baryonic singlet and keeps only one octet.

carrying particular symmetry properties, as

$$\begin{aligned}
M^{(0)} &\Leftrightarrow C_{fg}^{(0;3\bar{3})} q^f \bar{q}^g = \delta_{fg} q^f \bar{q}^g \\
M_a^{(8)} &\Leftrightarrow C_{afg}^{(8;3\bar{3})} q^f \bar{q}^g = \lambda_{fg}^a q^f \bar{q}^g \\
B_a^{(8)} &\Leftrightarrow C_{afgh}^{(8;333)} q^f q^g q^h \\
B_\eta^{(10)} &\Leftrightarrow C_{\eta fgh}^{(10;333)} q^f q^g q^h,
\end{aligned} \tag{1.4}$$

where the coefficients  $C$  accomplish the tensor product decompositions shown in Figure 1.2. The coefficient for the decouplet is totally symmetric, and as spin- $\frac{3}{2}$  it is symmetric in spin as well. It seems we are violating total antisymmetry for fermions, but an additional internal quantum number explains the discrepancy. This internal quantum number must give rise to an additional antisymmetry that allows the decouplet to satisfy spin-statistics. Because it is unobserved, we require mesons and baryons transform trivially; noting that singlets appear in both  $3 \otimes \bar{3}$  and  $3 \otimes 3 \otimes 3$ ,  $SU(3)$  seems to satisfy our needs; certainly the coefficient  $C_{ABC}^{(0;333)} = \epsilon_{ABC}$  is antisymmetric, as desired. So, in terms of quark and antiquark fields these mesons

and baryons are

$$\begin{aligned} M &\Leftrightarrow C_{AB}^{(0;33)_C} C_{fg}^{(;\bar{3}3)_F} q_A^f \bar{q}_B^g = \delta_{AB} C_{fg}^{(;\bar{3}3)_F} q_A^f \bar{q}_B^g \\ B &\Leftrightarrow C_{ABC}^{(0;333)_C} C_{fgh}^{(;\bar{3}33)_F} q_A^f q_B^g q_C^h = \epsilon_{ABC} C_{fgh}^{(;\bar{3}33)_F} q_A^f q_B^g q_C^h, \end{aligned} \quad (1.5)$$

where  $(\cdot)$  indicates 0, 8 or 10 as appropriate. This local gauge symmetry is named  $SU(3)$ -color, because a primary (RGB) color and its complement (CMY) make white, a meson, and a mix of all three make white as well, a baryon – the designation of *white* is meant to reflect the trivial transformation property.

In fact there seem to be six flavors of quarks, but the three least massive quarks are much lower in mass than the three highest, so one is able to consistently neglect the presence of these higher mass quarks in many circumstances. The  $SU(6)$  versions of the above diagrams are very hard to draw, and the symmetry is more badly broken.

## 1.5 Spectroscopy and Scattering

In this work, Monte Carlo methods are applied to spectroscopy, or energy extraction, in the isoscalar strange  $G_{1g}, G_{1u}, H_g$  and  $H_u$  baryonic symmetry channels, which contain the  $\Lambda$  particle and its resonances. (See chapter 4 for a discussion of these symmetry groups.) A particularly interesting resonance in these channels is the  $\Lambda(1405)$ , and we explore some qualitative methods to describe these states in terms of finite-volume energies. A direct identification here is not always possible, because ultimately the physical resonances are unstable and can decay, whereas our extracted stationary-state energies do not decay.

A more rigorous description is possible, which we develop in chapter 7 and apply to the simple case of  $\pi\pi$  scattering. There is a relationship, developed by Martin Lüscher, between finite-volume spectra and infinite-volume scattering processes [9] [10] [11]. This scattering information enables the lattice practitioner to extract the mass and even decay width of unstable resonances. We examine the  $L = 1, 3$  and 5 scattering phase shifts for the  $\rho(770)$  resonance in  $\pi\pi$  scattering using correlators in the isovector nonstrange  $T_{1u}^+, A_1^+, E^+, B_1^+$  and  $B_2^+$  mesonic channels. This is the first time that the higher partial waves are not neglected in any lattice QCD study, and the technique can be readily applied to baryonic resonances as well. We perform the entire calculation on a large  $32^3 \times 256$  anisotropic lattice with an unphysically heavy pion.

This thesis is organized as follows: Chapter 2 introduces the QCD Lagrangian and discretizes and Wick-rotates it to define the lattice version. Chapter 3 discusses improvements to the action and the tuning of its various free parameters. Chapter 4 details our method of operator construction, focusing on spatial smearing and symmetry properties. Chapter 5 details the Monte Carlo procedure and discusses the highly nontrivial incorporation of fermions as Grassmann variables in a computational model. Chapter 6 gives further details regarding the manipulation of correlation matrices and the extraction of the excited state energies from these correlators. Chapter 7 introduces the Luscher method for scattering phase shifts and resonance data and details our generalization to include more decay channels and partial waves. Finally, chapter 8 details the results of our spectroscopy and scattering analysis.

# Chapter 2

## Lattice QCD Lagrangian

In this chapter we give the Lagrangian density  $\mathcal{L}$  of Quantum Chromodynamics in continuous, infinite Minkowski space and discuss the Wick-rotation into Euclidean space. We also discuss the formulation of the theory on a space-time lattice.

### 2.1 The QCD Lagrangian

#### 2.1.1 The Fermionic Sector

In the previous chapter, we introduced the action  $S$  and briefly discussed the symmetries it ought to feature; we now pursue this in more detail. Quarks are spin- $\frac{1}{2}$  particles with charge and mass, so the relevant Lagrangian for free quarks is

$$S[\psi, \bar{\psi}] = \int d^4\mathbf{x} \mathcal{L} = \int d^4\mathbf{x} \bar{\psi}(\mathbf{x}) (i\gamma^\mu \partial_\mu - m) \psi(\mathbf{x}). \quad (2.1)$$

With only these fields, any other term renders the Lagrangian non-renormalizable.

The above Lagrangian contains one type of quark,  $\psi^\alpha$ , which contains an index ranging from one to four that counts over left- and right-handed chirality as well as spin up and down. It seems nature contains *six* flavors of quarks, so we ought to write

$$S[\{\psi_f, \bar{\psi}_f\}] = \int d^4\mathbf{x} \mathcal{L} = \int d^4\mathbf{x} \sum_{f=1}^6 \bar{\psi}_f (i\gamma^\mu \partial_\mu - m_f) \psi_f, \quad (2.2)$$

but three of the flavors have a prodigiously high mass  $m_f$ , such that their effect on the low energy spectrum is negligible. Because of this, we use only the first *three*

flavors, called *up*, *down*, and *strange*. Going further, the difference  $m_u - m_d$  is so incredibly small compared to the typical scales we are interested in that we simply take them to be the same. Then, we find:

$$S[\{\psi_f, \bar{\psi}_f\}] = \int d^4\mathbf{x} \mathcal{L} = \int d^4\mathbf{x} \sum_{f=\ell,s} \bar{\psi}_f (i\gamma^\mu \partial_\mu - m_f) \psi_f, \quad (2.3)$$

where to  $\psi_\ell$  we add an additional *isospin* index  $I$  ranging from one to two,

$$\psi_\ell^{\alpha I}(\mathbf{x}); \quad \psi_s^\alpha(\mathbf{x}). \quad (2.4)$$

This additional exact  $SU(2)$ -isospin symmetry

$$\begin{aligned} \mathcal{L}[\psi, \bar{\psi}] &\rightarrow \mathcal{L}'[\psi', \bar{\psi}'] = \mathcal{L}[\psi', \bar{\psi}'] \\ \text{for } \psi^I &\rightarrow \psi'^I = U_{IJ} \psi^J \text{ with } U \in SU(2) \end{aligned} \quad (2.5)$$

(as well as the trivial  $U(1)$ -strangeness symmetry) has important consequences for the form of our correlators. By taking operators that transform irreducibly under these symmetries, we will greatly reduce the number of correlators that must be calculated, knowing in advance that many of these are zero. This will be discussed in more detail in chapter 4.

The last, and the most important symmetry for Quantum *Chromodynamics* is  $SU(3)$ -color.

$$\begin{aligned} \mathcal{L}[\psi, \bar{\psi}] &\rightarrow \mathcal{L}'[\psi', \bar{\psi}'] = \mathcal{L}[\psi', \bar{\psi}'] \\ \text{for } \psi^A &\rightarrow \psi'^A = U_{AB} \psi^B \text{ with } U \in SU(3) \end{aligned} \quad (2.6)$$

That is, we add yet another index  $A$ , ranging from one to three; or from red, to blue, to green. Fully decorated,

$$\begin{aligned} S[\{\psi_f, \bar{\psi}_f\}] &= \int d^4\mathbf{x} \bar{\psi}_\ell^{\alpha IA} (i\gamma_{\alpha\beta}^\mu \partial_\mu - \delta_{\alpha\beta} m_\ell) \psi_\ell^{\beta IA} \\ &\quad + \bar{\psi}_s^{\alpha A} (i\gamma_{\alpha\beta}^\mu \partial_\mu - \delta_{\alpha\beta} m_s) \psi_s^{\beta A}. \end{aligned} \quad (2.7)$$

Color allows three quarks in the same position and spin-state without violating overall antisymmetry. All observed states, however, are colorless. We implement this by using invariant functionals, like  $\delta_{AB} \bar{\psi}^A \psi^B$  or  $\epsilon_{ABC} \psi^A \psi^B \psi^C$ . The symmetry is currently global, and will become local after we introduce the bosonic, or gauge, sector.

Finally, we briefly mention that these fields must *anticommute*, rather than commute, which means they cannot be real number- or complex number-valued. How to handle these complex Grassmann numbers on a computer will be discussed in more detail in chapter 5. In finite volume we take the quark fields to be periodic in space, but we require *anti*-periodicity in time in order to make contact with the trace in the partition function. That is, these Grassmann numbers must satisfy  $\psi(\mathbf{x}, t) = -\psi(\mathbf{x}, t + T)$ .

### 2.1.2 Gauge Invariance

Electrons and positrons are to photons as colored quarks and antiquarks are to gluons. Just like with  $U(1)$  electric charge, we take the previous Lagrangian and demand its global  $SU(3)$  be promoted to a local  $SU(3)$ ,

$$\begin{aligned} \mathcal{L}[\psi, \bar{\psi}] &\rightarrow \mathcal{L}'[\psi', \bar{\psi}'] \neq \mathcal{L}[\psi', \bar{\psi}'] \quad (\text{currently}) \\ \text{for } \psi^A(\mathbf{x}) &\rightarrow \psi'^A(\mathbf{x}) = U_{AB}(\mathbf{x})\psi^B(\mathbf{x}) \text{ with } U(\mathbf{x}) \in SU(3), \end{aligned} \quad (2.8)$$

which is violated by the kinetic term:

$$\sum_{\mu} \lim_{\epsilon \rightarrow 0} \bar{\psi}(\mathbf{x}) i\gamma^{\mu} \left( \frac{\psi(\mathbf{x} + a\epsilon \mathbf{e}_{\mu}) - \psi(\mathbf{x})}{a\epsilon} \right). \quad (2.9)$$

The symmetry-violating extended structure  $\bar{\psi}(\mathbf{x})\psi(\mathbf{y})$  is fixed by adding a gauge transporter  $G$  satisfying

$$G(\mathbf{x}, \mathbf{y}) \rightarrow G'(\mathbf{x}, \mathbf{y}) = U(\mathbf{x})G(\mathbf{x}, \mathbf{y})U^{\dagger}(\mathbf{y}), \quad (2.10)$$

to form

$$\begin{aligned} \sum_{\mu} \lim_{\epsilon \rightarrow 0} \bar{\psi}(\mathbf{x}) i\gamma^{\mu} \left( \frac{G(\mathbf{x}, \mathbf{x} + a\epsilon \mathbf{e}_{\mu})\psi(\mathbf{x} + a\epsilon \mathbf{e}_{\mu}) - \psi(\mathbf{x})}{a\epsilon} \right) \\ \equiv \bar{\psi}^A(\mathbf{x}) i\gamma^{\mu} D_{\mu}^{AB} \psi^B(\mathbf{x}). \end{aligned} \quad (2.11)$$

Because this is infinitesimally close to the identity we can expand using a basis of  $\mathfrak{su}(3)$  as

$$\sum_{\mu} \lim_{\epsilon \rightarrow 0} \bar{\psi}(\mathbf{x}) i\gamma^{\mu} \left( \frac{iga\epsilon \mathbf{e}_{\mu} \cdot \mathbf{A}^a(\mathbf{x}) \frac{\lambda^a}{2} \psi(\mathbf{x}) + \psi(\mathbf{x} + a\epsilon \mathbf{e}_{\mu}) - \psi(\mathbf{x})}{a\epsilon} \right) \quad (2.12)$$

to find the familiar gauge fields. Typically the Lagrangian is crafted out of these gauge fields  $A_\mu^a$ , but one could also make invariant terms out of the gauge transporter  $G$ .

### 2.1.3 The Bosonic Sector

The Lagrangian describing the gluon dynamics in the absence of quarks can be written in terms of the field tensor,

$$F_{\mu\nu}^a = \partial_\mu A_\nu^a - \partial_\nu A_\mu^a + g f^{abc} A_\mu^b A_\nu^c \quad (2.13)$$

(with the structure constants  $f^{abc}$  of  $\mathfrak{su}(3)$ ) as

$$\mathcal{L}_{\text{bos.}} = -\frac{1}{4} F_{\mu\nu}^a F^{\mu\nu a} + \theta \epsilon^{\mu\nu\rho\sigma} F_{\mu\nu}^a F_{\rho\sigma}^a, \quad (2.14)$$

though experimental evidence suggests  $\theta$  is negligible, *i.e.* that QCD respects parity, so we do not include it.<sup>1</sup>

We can reconstruct the bosonic sector in terms of gauge transporters by exploiting how they act on quark fields,

$$\lim_{\epsilon \rightarrow 0} G(\mathbf{x}, \mathbf{x} + a\epsilon \mathbf{e}_\mu) \psi(\mathbf{x} + a\epsilon \mathbf{e}_\mu) = \lim_{\epsilon \rightarrow 0} e^{a\epsilon \mathbf{e}_\mu D^\mu} \psi(\mathbf{x}). \quad (2.15)$$

So, in terms of the matrix-valued field tensor  $F_{AB}^{\mu\nu} = F_a^{\mu\nu} \lambda_{AB}^a = [D^\mu, D^\nu]_{AB}$  we can see that

$$F^{\mu\nu} = [D^\mu, D^\nu] = \lim_{a \rightarrow 0} \frac{1}{ga^2} \left( e^{a^2 [D^\mu, D^\nu]} - 1 \right). \quad (2.16)$$

---

<sup>1</sup>Despite its renormalizability; up to this point we have included all possible renormalizable terms. A similar term in the fermionic sector,  $m(e^{i\theta' \gamma^5})_{\alpha\beta}$  can be removed *via* a similarity transformation of the gamma matrices and is thus physically irrelevant. Although it is a total divergence, it is believed the theta-term in the gauge sector can not be removed.

The leading term of the exponential,  $F$ , is traceless, so we can take the trace of the series to find the kinetic term,

$$\begin{aligned}
\frac{1}{4}\text{Tr}F^{\mu\nu}F_{\mu\nu} &= \lim_{a\rightarrow 0} \frac{1}{g^2a^4}\text{Tr}\left(e^{[aD^\mu, aD^\nu]} - 1\right) \quad (\text{no sum over lorentz indices}) \\
&= \lim_{a\rightarrow 0} \frac{1}{g^2a^4}\text{Tr}\left(e^{aD^\mu}e^{aD^\nu}e^{-aD^\mu}e^{-aD^\nu} - 1\right) \\
\frac{1}{4}\text{Tr}F^{\mu\nu}F_{\mu\nu} &= \sum_{\substack{(\mu,\nu)-\\ \text{planes}}} \lim_{a\rightarrow 0} \frac{1}{g^2a^4}\text{Tr}\left(G_{\mu\nu} - 1\right),
\end{aligned} \tag{2.17}$$

where by  $G_{\mu\nu}$  we indicate a small  $a \times a$ -sized box, or *plaquette*, of gauge-links.

### 2.1.4 Wick-Rotating the QCD Lagrangian

Our full QCD Lagrangian density is then:

$$\mathcal{L} = \sum_{f=\ell,s} \bar{\psi}_f \left( i\gamma \cdot \left[ \partial + ig\mathbf{A} \cdot \frac{\lambda}{2} \right] - m_f \right) \psi_f - \frac{1}{4}\text{Tr}F^2 \tag{2.18}$$

for  $\psi_\ell^{\alpha IA}, \psi_s^{\alpha A}$ , and  $A_\mu^a$ .

Written in terms of gauge transporters, which will be more important for the discretization, we find:

$$\begin{aligned}
\mathcal{L} = \sum_{f=\ell,s}^\mu \bar{\psi}_f(\mathbf{x}) \left( i\gamma^\mu \left[ \frac{G(\mathbf{x}, \mathbf{x} + \mathbf{a}_\mu) - 1}{a} \right] \psi_f(\mathbf{x} + \mathbf{a}_\mu) - m_f \psi_f(\mathbf{x}) \right) \\
+ \sum_{\substack{(\mu,\nu)-\\ \text{planes}}} \frac{1}{2g^2a^4}\text{Tr}(G_{\mu\nu} - 1)
\end{aligned} \tag{2.19}$$

in the limit that each  $\mathbf{a}_\mu = a\mathbf{e}_\mu \rightarrow 0$ .

With the continuum Lagrangian density in hand, we now Wick-rotate, setting  $t = -i\tau$ :

$$\begin{aligned}
x_{(E)}^4 \equiv ix_{(M)}^0 &\Rightarrow \partial_4^{(E)} = -i\partial_0^{(M)} \Rightarrow A_4^{a(E)} = -iA_0^{a(M)} \quad \text{and} \quad \gamma_{(E)}^4 \equiv \gamma_{(M)}^0 \\
x_{(E)}^i \equiv x_{(M)}^i &\Rightarrow \partial_i^{(E)} = \partial_i^{(M)} \Rightarrow A_i^{a(E)} = A_i^{a(M)} \quad \text{and} \quad \gamma_{(E)}^i \equiv -i\gamma_{(M)}^i.
\end{aligned}$$

This changes the Minkowski  $\gamma^\mu D_\mu$  to a Euclidean  $i\gamma^\mu D_\mu = i\gamma_\mu D_\mu$ , leaves the kinetic gauge term alone, and introduces a small subtlety into the  $\bar{\psi}$  fields.

The requirement of  $\text{SO}^+(1,3)$  invariance becomes  $\text{SO}(4)$  invariance, which pre-

vents  $\bar{\psi}\psi = \psi^\dagger\gamma^0\psi$  in the Minkowski case from becoming  $\psi^\dagger\gamma^4\psi$  in the Euclidean case as the latter is not  $\text{SO}(4)$  invariant. Although they now have identical transformation properties,  $\bar{\psi} = \psi^\dagger$  is also not possible; it spoils the identification of Euclidean Green's functions with Wick-rotated Minkowski Green's functions.

From the point of view of the path integral,  $\bar{\psi}$  and  $\psi$  are separate integration variables, so they don't maintain any particular relationship. One difference between the Euclidean case and the Minkowski cases is that the action is no longer Hermitian.<sup>2</sup>

After the changes, we get:

$$iS_{(M)} \rightarrow -S_{(E)} = - \int d^4\mathbf{x} \sum_{f=\ell,s} \bar{\psi}_f \left( \boldsymbol{\gamma} \cdot \left[ \boldsymbol{\partial} + g\mathbf{A} \cdot \frac{\boldsymbol{\lambda}}{2} \right] + m_f \right) \psi_f + \frac{1}{4} \text{Tr} F^2, \quad (2.20)$$

where every field is understood as residing in Euclidean space.

## 2.2 Naïve Discretization

The action of equation 2.20 represents an uncountably infinite number of continuous degrees of freedom. This integration is divergent and requires a regularization, with physical values extracted as the regulator is removed. The lattice regulates the theory by making the number of degrees freedom finite.

Wilson [12] wrote down a lattice-regularized Lagrangian density for fermions that preserves gauge symmetry and reduces to the form 2.20 in the continuum limit, and Reisz [13] showed that such a regularization scheme maintains renormalizability at all orders in perturbation theory.

Looking at our action 2.19 written in terms of small gauge-transporters, a plausible discretization is practically immediate. We only rewrite the covariant derivative term, in a more symmetrical form, so the action  $S$  is:

$$S = a^4 \sum_{\mathbf{n}} \left[ \sum_{f=\ell,s} \sum_{\mu} \frac{1}{a^3} \bar{\psi}_f(\mathbf{n}) \gamma_{\mu} \left( \frac{G_{\mu}(\mathbf{n}) \psi_f(\mathbf{n} + \hat{\mu}) - G_{-\mu}(\mathbf{n}) \psi_f(\mathbf{n} - \hat{\mu})}{2a} \right) + \frac{1}{a^3} m_f \bar{\psi}_f(\mathbf{n}) \psi_f(\mathbf{n}) + \sum_{\substack{\mu\nu: \\ \mu < \nu}} \frac{1}{2g^2 a^4} \text{Re Tr}(1 - G_{\mu\nu}(\mathbf{n})) \right] \quad (2.21)$$

---

<sup>2</sup>However,  $\gamma^5$ -Hermiticity of  $M$  in  $S = \bar{\psi}M\psi + S_g$  guarantees at least that  $\det M$  is real.

for *gauge-links*  $G_\mu$  that span from one lattice site to the next, and *plaquettes*  $G_{\mu\nu}$  that run over a small  $1 \times 1$  loop in the  $(\mu\nu)$ -plane,

$$\begin{aligned} G_\mu(\mathbf{n}) &= G_{\mu;n} = G(\mathbf{n}, \mathbf{n} + \hat{\nu}) \\ G_{\mu\nu}(\mathbf{n}) &= G_{\mu,\nu} = G_\mu(\mathbf{n})G_\nu(\mathbf{n} + \hat{\mu})G_{-\mu}(\mathbf{n} + \hat{\mu} + \hat{\nu})G_{-\nu}(\mathbf{n} + \hat{\nu}). \end{aligned} \tag{2.22}$$

(Sometimes we also use a  $1 \times 2$ -loop.) In this form the fields, gauge-links and integer-tuples  $\mathbf{n}$  are manifestly dimensionless, though the  $m_f$ 's still have dimensions.

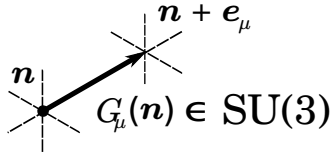


Figure 2.1: A gauge link covers a lattice link in a particular direction.

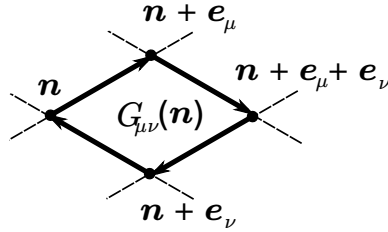


Figure 2.2: Four gauge links multiply together to make a plaquette.

The term *naïve* discretization is used because there are an infinite number of lattice theories that all have the same continuum limit; any two lattice actions  $S_1$  and  $S_2$  represent the same continuum theory provided  $\Delta S$  vanishes as  $a \rightarrow 0$ . Therefore we can add additional terms, *e.g.* to improve the convergence from  $\mathcal{O}(a)$  to  $\mathcal{O}(a^2)$  or to help alleviate any undesirable features, provided the continuum limit is unaffected.

# Chapter 3

## Action Improvement

In this chapter we discuss the various improvements and modifications made to the lattice-discretized QCD Lagrangian, including how we solve the fermion doubling problem. We especially note the addition of new terms to the action and modification of gauge variables in the fermionic sector. We also discuss the tuning of the various parameters appearing in the action, specifically the quark masses, anisotropy, and coupling.

### 3.1 Fermion Doubling

Because the discretized action must only agree in the continuum limit, we can add additional terms provided they become irrelevant in this limit. There is a particular undesirable feature appearing in the fermion action – there are  $2^4 - 1$  other fermions in the theory! This is known as fermion doubling, and occurs because the fermion propagator has extra poles at the ends of the Brillouin zone, for all momenta with any component  $p_\mu = \frac{\pi}{a}$ . This is clear given the form of the propagator for massless modes:

$$D_F^{-1}(\mathbf{p}) = a \frac{-i \sum_\mu \gamma_\mu \sin(ap_\mu)}{\sum_\mu \sin^2(ap_\mu)}, \quad (3.1)$$

found from the free massless fermion action

$$\begin{aligned}
S_F &= \sum_{mn} a \bar{\psi}(\mathbf{n}) \left[ \sum_{\mu} \gamma^{\mu} \frac{\delta_{\mathbf{n}+\hat{\mu},\mathbf{m}} - \delta_{\mathbf{n}-\hat{\mu},\mathbf{m}}}{2a} \right] \psi(\mathbf{m}) \\
&= \sum_{mn} a \bar{\psi}(\mathbf{n}) D(\mathbf{n}, \mathbf{m}) \psi(\mathbf{m}) \\
D(\mathbf{p}, \mathbf{q}) &= \frac{1}{N^4} \sum_{nm} e^{-ia\mathbf{p}\cdot\mathbf{n}} D(\mathbf{n}, \mathbf{m}) e^{ia\mathbf{q}\cdot\mathbf{m}} \\
&= \delta_{\mathbf{p},\mathbf{q}} D(\mathbf{p}).
\end{aligned} \tag{3.2}$$

Such a term has poles not just at  $\mathbf{p} = (0, 0, 0, 0)$ , but also for any combination of  $\frac{\pi}{a}$ 's.

### 3.1.1 Wilson Fermions

This defect can be treated by adding the *Wilson term* [14],

$$\begin{aligned}
D(\mathbf{p}) &\rightarrow D(\mathbf{p}) + \frac{1}{a} \sum_{\mu} (1 - \cos(ap_{\mu})) \\
D(\mathbf{n}, \mathbf{m}) &\rightarrow D(\mathbf{n}, \mathbf{m}) - \sum_{\mu} \frac{\delta_{\mathbf{n}+\hat{\mu},\mathbf{m}} - 2\delta_{\mathbf{n},\mathbf{m}} + \delta_{\mathbf{n}-\hat{\mu},\mathbf{m}}}{2a}
\end{aligned} \tag{3.3}$$

which is a discretized form of  $a\partial^2$ , acting on a fermion field. This becomes negligible in the continuum limit, and adds a mass on the order of  $\frac{1}{a}$  to each doubled mode. Therefore, it causes these modes to not affect the low energy theory for small lattice sizes.

Unfortunately, adding a mass in this way explicitly breaks chiral symmetry; there is no-go theorem that prevents any lattice regularization from preserving translational invariance, locality, chiral symmetry and Hermiticity without additional fermion modes [15] [16]. Our action necessarily violates Hermiticity and chiral symmetry because of the fermion masses; importantly, massless fermions would *still* run afoul of the theorem – the Wilson term gives a mass, thus breaking chiral symmetry explicitly and satisfying the theorem.

## 3.2 Symanzik Improvement

Other terms may be added which improve the convergence in  $a$ , provided they disappear in the continuum limit [17]. This is Symanzik improvement, and is performed in both the fermionic and gauge sectors. For example, we add the *clover term* [18],

$$\frac{c_{sw}}{a} \sum_{\mu < \nu} \frac{1}{2} \bar{\psi}(\mathbf{n}) \sigma_{\mu\nu} C_{\mu\nu}(\mathbf{n}) \psi(\mathbf{n}) \quad (3.4)$$

where the  $C$ 's in the clover term are sums of plaquette petals,

$$C_{\mu\nu} = \frac{1}{4} \text{Im} P_{\mu\nu} \quad (3.5)$$

for  $P_{\mu\nu} = G_{\mu,\nu} + G_{\nu,-\mu} + G_{-\mu,-\nu} + G_{-\nu,\mu}$ .

In addition to improve the  $\mathcal{O}(a)$  convergence, this term also seems to partially alleviate the chirality-breaking effects of Wilson fermions [19].

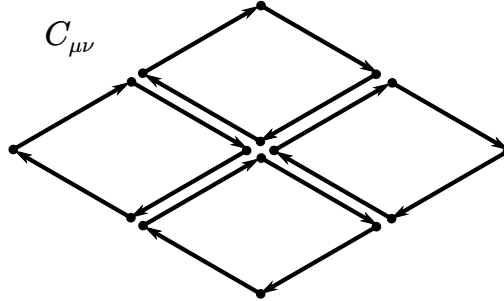


Figure 3.1: Four plaquettes sum together in the clover term.

In the gauge sector,  $\mathcal{O}(a)$  corrections can be alleviated by adding  $2 \times 1$  plaquettes in the action [20]. For these we use the term  $R_{\mu\nu}$ .

## 3.3 Tadpole Improvement and Stout Smearing

In addition to explicit  $\mathcal{O}(a)$  convergence, there is a modification we make to cancel some contributions from tadpole diagrams in the gauge sector [21]. These are generated by the expansion of  $e^{\int \text{ds} \cdot A}$  and are reduced by rescaling each link in a given

direction, by

$$u = \frac{1}{3} \langle \text{ReTr} (G_{\mu\nu}) \rangle^{\frac{1}{4}}$$

$$\text{as } G_{\mu\nu} \rightarrow \frac{1}{u^4} G_{\mu\nu}.$$
(3.6)

In practice we tune these  $u$ 's iteratively, until we find a fixed point where the variable that appears in the action  $u_{\text{input}}$  is the same as  $u_{\text{output}}$  calculated as in 3.6 [22].

Though we will visit the issue further in chapter 4 on operator construction, we must pause here and discuss smearing, also. High energy modes are generally less sensitive to spatially-smeared objects, in the sense that their correlation is reduced and the smeared operator excites more low energy modes, which we want, and fewer high energy modes, which serve only to contaminate the spectrum.

This has applications to operators in both sectors, but in the action only the modification of the gauge links  $G_\mu$  is important. We replace each gauge link in a given direction with a superposition of all  $\square$ -shaped links, with various weights  $\rho_\mu$ . The process is performed iteratively, to generate *stout-smeared* [23] gauge links  $\tilde{G}_\mu$ :

$$\mathcal{S}_\mu[G_\mu] = \sum_{\pm\nu \neq \mu} \rho_{\mu\nu} \left( G_{\nu;x} G_{\mu;x+\hat{\nu}} G_{\nu;x+\hat{\mu}}^\dagger + G_{\nu;x-\hat{\nu}}^\dagger G_{\mu;x-\hat{\nu}} G_{\nu;x-\hat{\nu}+\hat{\mu}} \right)$$

$$\mathcal{Q}_\mu[G_\mu] = -\text{Im} \left( \mathcal{S}[G_\mu] G_\mu^\dagger - \frac{1}{3} \text{Tr} \mathcal{S}[G_\mu] G_\mu^\dagger \right)$$

$$G_\mu^{(n+1)} = \exp(\mathcal{Q}_\mu[G_\mu^{(n)}]) G_\mu^{(n)},$$
(3.7)

where the spatial weight is set to  $\rho_{ij} = \rho = 0.14$  and temporal directions are not smeared ( $\rho_{\mu 4} = \rho_{4\mu} = 0$ ), with  $n = 2$  iterations. The differentiability of this smearing method is a convenient consequence of the analytic group-multiplicative form. The symbol  $\tilde{G}$  is used to indicate links that have been smeared in this way. The smeared links replace the unsmeared links only in the fermion action.

### 3.4 Anisotropic Improved Action

Finally, we note that our lattice is made anisotropic between space and time. That is, we take each cell's spatial length  $a_s$  to be greater than its temporal length  $a_t$ ; we are calculating temporal correlators, so the additional time resolution is critical, es-

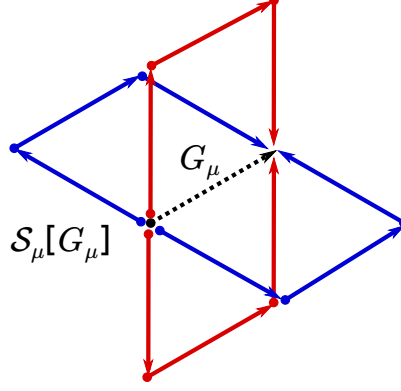


Figure 3.2: Illustration of stout-smeared gauge link.

pecially for extracting excited state energies. The anisotropy  $\xi$  enters the Lagrangian separately in the fermionic and gauge actions as  $\xi_F$  and  $\xi_G$ . These are only bare parameters, and in practice both must be tuned separately to ensure that the renormalized anisotropies of each sector remain identical. The  $2 \times 1$  plaquettes  $R$  in the gauge action are arranged such that the double-length directions are purely spatial, and we calculate separate  $u_s$  and  $u_t$  tadpole factors (from loops in purely spatial planes  $x_i \times x_j$  and temporal planes  $x_0 \times x_i$ , respectively).

With everything included, our action is [24]:

$$\begin{aligned}
S[\bar{\psi}, \psi, G] = \sum_{nmf} \bar{\psi}_f(\mathbf{n}) & \left[ \sum_{\mu} \left( \rho_{\mu}^{(1)} \gamma_{\mu} \frac{\tilde{G}_{\mu}(\mathbf{n}) \delta_{n+\hat{\mu},m} - \tilde{G}_{-\mu}(\mathbf{n}) \delta_{n-\hat{\mu},m}}{2} \right. \right. \\
& \left. \left. - \rho_{\mu}^{(1)} \frac{\tilde{G}_{\mu}(\mathbf{n}) \delta_{n+\hat{\mu},m} - 2\delta_{n,m} + \tilde{G}_{-\mu}(\mathbf{n}) \delta_{n-\hat{\mu},m}}{2} \right) \right. \\
& \left. + a_t m_f \delta_{n,m} - \sum_{\mu < \nu} \frac{1}{2} \rho_{\mu}^{(2)} \sigma_{\mu\nu} \tilde{C}_{\mu\nu}(\mathbf{n}) \delta_{n,m} \right] \psi_f(\mathbf{m}) \\
& + \sum_{\mathbf{n}} \frac{5\beta}{9\xi_G} \sum_{\mu < \nu} \rho_{\mu\nu}^{(3)} \text{Tr}[1 - G_{\mu\nu}(\mathbf{n})] + \frac{\beta}{36\xi_G} \sum_{\mu < \nu} \rho_{\mu\nu}^{(4)} \text{Tr}[1 - R_{\mu\nu}(\mathbf{n})]
\end{aligned} \tag{3.8}$$

for

$$\begin{aligned}
\rho_\mu^{(1)} &= \begin{cases} \frac{1}{\tilde{u}_s} \frac{\xi_F}{\xi_G} \frac{1}{\xi} \\ \frac{1}{\tilde{u}_t} \end{cases} & \rho_\mu^{(2)} &= \begin{cases} \frac{1}{(\tilde{u}_s)^3} \frac{\xi_G}{\xi_F} & \text{spatial} \\ \frac{1}{2\tilde{u}_s\tilde{u}_t^2} \frac{1}{\xi_G} \left( \frac{1}{\xi} + \frac{\xi_G}{\xi_F} \right) & \text{temporal} \end{cases} \\
\rho_{\mu\nu}^{(3)} &= \begin{cases} \frac{1}{(u_s)^4} \\ \frac{4}{5(u_s u_t)^2} \xi_G^2 \end{cases} & \rho_{\mu\nu}^{(4)} &= \begin{cases} \frac{1}{(u_s)^6} & \text{spatial plane} \\ \frac{4}{(u_s^2 u_t)^2} \xi_G^2 & \text{space-time plane} \end{cases}
\end{aligned} \tag{3.9}$$

In order, these are the minimally-coupled fermionic kinetic term, Wilson term, fermionic mass term, clover term, and gauge kinetic terms. We have indicated separate tadpole factors, calculated with smeared and unsmeared links  $\tilde{u}$  and  $u$ , in each weight term  $\rho$ , as well as the fermion, gauge and renormalized anisotropies  $\xi_F$ ,  $\xi_G$  and  $\xi$ . Everything is given as a dimensionless variable, with the exception of  $m$ , which is instead always written in dimensionless form as  $a_t m$ .

## 3.5 Parameter Tuning

### 3.5.1 Heavy Pion

Corrections between the finite-volume and infinite-volume spectra are expected to decrease as we increase the length, compared to the coherence length or mass of the lightest particle. Specifically, for a massive particle like the pion (*i.e.* a mass gap) these corrections are suppressed by  $e^{-m_\pi L}$ . So, increasing  $m_\pi L$  is critical. This has effects not just for the accuracy, but also the precision of our results. We will eventually find it necessary to estimate matrix inverses, and the low pion mass increases the likelihood of ill-conditioned matrices.

Other than the pion, we also use the kaon and the omega baryon to set some input parameters. Chiral perturbation theory finds that the following quantities are proportional to the quark masses, to first order:

$$\begin{aligned}
\ell_\Omega &= \frac{9m_\pi^2}{4m_\Omega^2} \\
s_\Omega &= \frac{9(2m_K^2 - m_\pi^2)}{4m_\Omega^2}.
\end{aligned} \tag{3.10}$$

The values  $a_t m_s = -.0743$  and  $a_t m_\ell = -.0840$  are selected, found by monitoring simple operators for each particle type until the desired  $(\ell_\Omega, s_\Omega)$  is achieved. We choose  $s_\Omega$  to have its physical value, while we keep  $\ell_\Omega$  as small as possible without making the entire calculation infeasible. Further details for this tuning procedure, and those that follow, may be found in [24].

### 3.5.2 Anisotropy

As previously mentioned, there are separate anisotropy parameters  $\xi_G$  and  $\xi_F$  in the action. There is an additional anisotropy parameter  $\xi$ , which we refer to as the desired anisotropy. The last of these represents the desired ratio  $\frac{a_s}{a_t}$ , and the other two are tuned to reproduce this value in their respective sector.

In the gauge sector, the anisotropy  $\xi_G$  is set by tracking the ratio of Wilson loop ratios:

$$\frac{\left(\frac{W_{ss}(a, b)}{W_{ss}(a+1, b)}\right)}{\left(\frac{W_{st}(a, \xi b)}{W_{st}(a+1, \xi b)}\right)} = 1 \quad (3.11)$$

for

$$W_{\mu\nu}(a, b) = \left\langle \text{Tr} \left\{ U(\mathbf{n}, \mathbf{n} + a\hat{\mu}) U(\mathbf{n} + a\hat{\mu}, \mathbf{n} + a\hat{\mu} + b\hat{\nu}) \right. \right. \\ \left. \left. \times U(\mathbf{n} + a\hat{\mu} + b\hat{\nu}, \mathbf{n} + b\hat{\nu}) U(\mathbf{n} + b\hat{\nu}, \mathbf{n}) \right\} \right\rangle. \quad (3.12)$$

For a desired anisotropy  $\xi = 3.5$  this is achieved with  $\xi_G = 4.3$ . In the fermion sector, the anisotropy  $\xi_F$  is set by tracking the dispersion relation

$$a_t^2 E^2(\mathbf{d}) = a_t^2 m_\pi^2 + \frac{(2\pi)^2}{\xi^2 N_s^2} \mathbf{d}^2 \quad (3.13)$$

for a pion operator with momentum  $\frac{2\pi}{L}\mathbf{d}$ . In order to find  $\xi = 3.5$ , we set  $\xi_F = 1.3$ . (Actually, we replace  $\xi_F$  by  $\nu = \frac{\xi_G}{\xi_F}$  and set  $\nu = 3.4$ .)

### 3.5.3 Gauge-coupling

The parameter  $\beta = \frac{6}{g^2}$  represents the coupling, and is set to 1.5. This value was chosen to obtain a spatial lattice spacing of about 0.14 fm, determined with a variety

of particle masses. This spacing is known to produce near-continuum physics while maintaining a sufficiently large volume. With this value, a physical  $m_\Omega$  particle gives a lattice spacing of  $a_t = .034$  fm. In order to take the continuum limit and change  $a$  we would need to change this  $\beta$  value. One should see that as we change  $\beta$  to the continuum limit value, we should find all of our dimensionless energies  $a_t E$  shrink in value, so that we may divide them by ever decreasing  $a_t$  to bring them to the physical values. That is, we must have tuned the theory near a *critical point*, where the correlation lengths *diverge*.

This is not as much of an issue for spectroscopy, because  $a_t$  explicitly disappears in mass ratios. In fact, these ratios differ from their continuum limit values by terms of  $\mathcal{O}(a^2)$ . Because of this, we require our  $\beta$  to be tuned such that: we are insensitive to the difference between lattice and continuum dispersion relations, and our correlators do not fall to zero too quickly due to large  $a_t E$ .

# Chapter 4

## Operator Construction

In this chapter we discuss operator construction, with regard to irreducibility, multiparticle states, displacements and smearing. Much of this chapter focuses on the many internal and external symmetry transformations that we apply to the fields. The important quantum numbers to consider are isospin, parity, G-parity, strangeness as well as the lattice's substitute for full rotational symmetry, the symmetries of a cube.

### 4.1 Single Hadrons

#### 4.1.1 Elemental Components

As discussed previously, we are extracting energies from the fall-off of temporal correlators. We must use operators  $\hat{A}, \hat{B}$  that have overlap with the energy-state of interest. For a trivial example, consider  $\phi^4$  theory: if one is interested in the first excited state ( $\phi$ -particle at rest) energy, we could temporally-correlate the operator  $\hat{\phi}(\mathbf{p} = 0)$  with itself, but one cannot expect to extract this state *via*  $\hat{\phi}(\mathbf{p} \neq 0)$ , as this latter operator could not couple to any state of total momentum zero. The crucial distinction is *symmetry* – the latter operator responds to translations in a different way than the former, and indeed in a different way than the actual first excited state. By ensuring that our single-hadron operators possess particular symmetry properties, we guarantee that they will create states that overlap significantly with single-hadron states of interest.

The first symmetry we consider is gauge invariance, and every operator we construct must be exactly gauge invariant. We also ask for particular rotational symme-

tries, and discrete symmetries like time-reversal, parity and G-parity.

We have already discussed at length how to make gauge-invariant gluonic operators out of gauge-links, because such terms appear in the action. That is, operators such as

$$\hat{A}_{\mu\nu}(\mathbf{p}, t) = \sum_{\mathbf{x}} e^{i\mathbf{p}\cdot\mathbf{x}} \text{Tr} \hat{G}_{\mu\nu}(\mathbf{x}, t) \quad (4.1)$$

are gauge-invariant, and create states of particular total momentum  $\mathbf{p}$  [25]. (The trace is over color indices, which are not displayed.)

Gauge-invariant operators made out of fermions have also already appeared in the action. For example, the term

$$\hat{A}_{\alpha\beta}(\mathbf{p}, t) = \sum_{\mathbf{x}} e^{i\mathbf{p}\cdot\mathbf{x}} \hat{\psi}_{\alpha}(\mathbf{x}, t) \hat{\psi}_{\beta}(\mathbf{x}, t) \quad (4.2)$$

already appears in the action, as the mass term, and shares some quantum numbers of a meson with momentum  $\mathbf{p}$ . (The color indices are summed over, and not displayed.) The above operator is used to create meson states, and we can construct another type of gauge-invariant functional<sup>1</sup> out of *three* quark fields, as

$$A_{\alpha\beta\gamma}(\mathbf{p}, t) = \sum_{\mathbf{x}} e^{i\mathbf{p}\cdot\mathbf{x}} \epsilon_{abc} \psi_{\alpha a}(\mathbf{x}) \psi_{\beta b}(\mathbf{x}) \psi_{\gamma c}(\mathbf{x}), \quad (4.3)$$

which represents a typical baryon operator. Both the mesonic and baryonic operators we have considered so far are referred to as *single-site*, meaning that each constituent quark field is taken at the same spatial site. To capture orbital and radial structure we consider spatially extended objects.

### 4.1.2 Covariant Displacements

If we are interested in simple examples of spatially-displaced objects that still transform gauge-invariantly, we need look no further than our action. That is, we had already solved the problem of  $\bar{\psi}(\mathbf{x})\psi(\mathbf{x} + \hat{\mu})$  in the kinetic term by including a gauge-link, as

$$A_{\alpha\beta\mu}(\mathbf{p}, t) = \sum_{\mathbf{x}} e^{i\mathbf{p}\cdot\mathbf{x}} \bar{\psi}_{\alpha}(\mathbf{x}) G(\mathbf{x}, \mathbf{x} + \hat{\mu}) \psi_{\beta}(\mathbf{x} + \hat{\mu}), \quad (4.4)$$

---

<sup>1</sup>After this point, we will stop tediously distinguishing between functionals and operators.

where color indices are hidden and summed over. Likewise, we can make spatially extended baryon operators with

$$A_{\alpha\beta\gamma\mu\nu\rho}(\mathbf{p}, t) = \sum_{\mathbf{x}} e^{i\mathbf{p}\cdot\mathbf{x}} \epsilon_{abc} G_{ad}(\mathbf{x}, \mathbf{x} + \hat{\boldsymbol{\mu}}) \psi_{ad}(\mathbf{x} + \hat{\boldsymbol{\mu}}) \times G_{be}(\mathbf{x}, \mathbf{x} + \hat{\boldsymbol{\nu}}) \psi_{be}(\mathbf{x} + \hat{\boldsymbol{\nu}}) G_{cf}(\mathbf{x}, \mathbf{x} + \hat{\boldsymbol{\rho}}) \psi_{cf}(\mathbf{x} + \hat{\boldsymbol{\rho}}). \quad (4.5)$$

In this work, we displace the quark fields only in spatial directions, using the notation

$$(D_{\hat{\mathbf{j}}}\psi)_{\alpha a}(\mathbf{x}) \equiv G_{ab}(\mathbf{x}, \mathbf{x} + \hat{\mathbf{j}}) \psi_{ab}(\mathbf{x} + \hat{\mathbf{j}}) \quad (4.6)$$

to denote a quark field displaced such that it transforms as if it were at  $\mathbf{x}$ , but actually lies on the adjacent site in the  $\hat{\mathbf{j}}$  direction. Longer displacements mean higher powers of  $D$ . Following the same procedure as in [26]. For mesons, we perform the displacements shown in Figure 4.1, and for baryons we perform the displacements shown in Figure 4.2.

### 4.1.3 Hermiticity

To extract excited state energies, matrices of correlators are needed. Hence, we plan to evaluate large numbers of meson- and baryon-operators. Ensuring that our correlation matrices are Hermitian is crucial for the analysis techniques we plan to use to extract the excited-state energies. Our correlators should be Wick-rotated Minkowski objects, so we will define operators such that the Minkowski correlator is Hermitian, and Wick-rotate to find our desired Euclidean objects.

In Minkowski space, the Hermitian conjugate of  $\psi$  is  $\psi^\dagger = \bar{\psi}\gamma^0$ , which becomes  $\bar{\psi}\gamma^4$  after the rotation to Euclidean space. So, we replace every  $\psi$  with  $\bar{\psi}\gamma^4$  to make a new list of operators for use in manifestly Hermitian correlator matrices. For example, if we have a baryonic operator like

$$\epsilon\psi_\alpha\psi_\beta\psi_\gamma \quad (4.7)$$

we should find a real number after correlating with

$$\epsilon\chi_\alpha\chi_\beta\chi_\gamma = \epsilon\bar{\psi}_\delta\bar{\psi}_\epsilon\bar{\psi}_\zeta\gamma_\delta^4\gamma_\epsilon^4\gamma_\zeta^4. \quad (4.8)$$



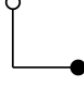
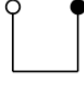

Illustration	Name	Explicit form ( $ i  \neq  j  \neq  k  \neq 0$ )
	single-site	$\delta_{ab} \tilde{\chi}_{a\alpha}^A \tilde{\psi}_{b\beta}^B$
	singly-displaced	$\delta_{ab} \tilde{\chi}_{a\alpha}^A \left( \tilde{D}_j^{(p)} \tilde{\psi} \right)_{b\beta}^B$
	doubly-displaced-L	$\delta_{ab} \left( \tilde{\chi} \tilde{D}_j^{(p)\dagger} \right)_{a\alpha}^A \left( \tilde{D}_k^{(p)} \tilde{\psi} \right)_{b\beta}^B$
	triply-displaced-U	$\delta_{ab} \left( \tilde{\chi} \tilde{D}_j^{(p)\dagger} \right)_{a\alpha}^A \left( \tilde{D}_k^{(p)} \tilde{D}_j^{(p)} \tilde{\psi} \right)_{b\beta}^B$
	triply-displaced-O	$\delta_{ab} \left( \tilde{\chi} \tilde{D}_i^{(p)\dagger} \right)_{a\alpha}^A \left( \tilde{D}_j^{(p)} \tilde{D}_k^{(p)} \tilde{\psi} \right)_{b\beta}^B$

Figure 4.1: Five types of quark-antiquark displaced operators. Each empty/filled circle represents smeared quark and antiquark fields, with the line segments indicating covariant displacements.


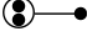


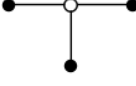

Illustration	Name	Explicit form ( $ i  \neq  j  \neq  k $ )
	single-site	$\varepsilon_{abc} \tilde{\psi}_{a\alpha}^A \tilde{\psi}_{b\beta}^B \tilde{\psi}_{c\gamma}^C$
	singly-displaced	$\varepsilon_{abc} \tilde{\psi}_{a\alpha}^A \tilde{\psi}_{b\beta}^B \left( \tilde{D}_j^{(p)} \tilde{\psi} \right)_{c\gamma}^C$
	doubly-displaced-I	$\varepsilon_{abc} \tilde{\psi}_{a\alpha}^A \left( \tilde{D}_{-j}^{(p)} \tilde{\psi} \right)_{b\beta}^B \left( \tilde{D}_j^{(p)} \tilde{\psi} \right)_{c\gamma}^C$
	doubly-displaced-L	$\varepsilon_{abc} \tilde{\psi}_{a\alpha}^A \left( \tilde{D}_j^{(p)} \tilde{\psi} \right)_{b\beta}^B \left( \tilde{D}_k^{(p)} \tilde{\psi} \right)_{c\gamma}^C$
	triply-displaced-T	$\varepsilon_{abc} \left( \tilde{D}_{-j}^{(p)} \tilde{\psi} \right)_{a\alpha}^A \left( \tilde{D}_j^{(p)} \tilde{\psi} \right)_{b\beta}^B \left( \tilde{D}_k^{(p)} \tilde{\psi} \right)_{c\gamma}^C$
	triply-displaced-O	$\varepsilon_{abc} \left( \tilde{D}_i^{(p)} \tilde{\psi} \right)_{a\alpha}^A \left( \tilde{D}_j^{(p)} \tilde{\psi} \right)_{b\beta}^B \left( \tilde{D}_k^{(p)} \tilde{\psi} \right)_{c\gamma}^C$

Figure 4.2: Five types of three quark displaced operators. Each filled circle represents smeared antiquark fields, with the line segments indicating covariant displacements. Here, the open circles represent epsilon symbols.

This replacement of  $\bar{\psi} \rightarrow \chi = \bar{\psi}\gamma_4$  causes issues with Lorentz invariance for bilinears:

$$\begin{aligned}\bar{\psi}\psi &\rightarrow \bar{\psi}SS^{-1}\psi = \bar{\psi}\psi \\ \chi\psi &\rightarrow \chi\gamma_4S\gamma_4S^{-1}\psi,\end{aligned}\tag{4.9}$$

but this is not a problem. Lorentz invariance, or even  $SO(4)$ , is not a symmetry of the hypercubic lattice so we can't make operators that transform irreducibly under this symmetry. The action is still minimized for these symmetries in the continuum and thermodynamic limits, so our fields take values such that the non-interacting correlator is

$$\langle\psi_\alpha(\mathbf{x})\bar{\psi}_\beta(\mathbf{y})\rangle = \int \frac{d^4\mathbf{k}}{(2\pi)^4} \frac{(-i\gamma_\mu k_\mu + m)_{\alpha\beta}}{k^2 + m^2} e^{i\gamma\cdot(\mathbf{x}-\mathbf{y})},\tag{4.10}$$

which Wick-rotates to the desired Minkowski result. Effectively multiplying this by  $\gamma_4$  to achieve a  $\chi$  field in the correlator, matching our operators, doesn't affect the spectrum which appears as zeroes of  $k^2 + m^2$ . So, we swap all  $\bar{\psi}$ 's with  $\chi$ 's to get a Hermitian correlator without worrying about spoiled  $SO(4)$  invariance of mesonic operators. It bears repeating that our action ensures the energies come from a theory which is Lorentz invariant in the physical limit, without requiring that our operators are Lorentz invariant in the physical limit. (That is, compare Equation 4.10 with 4.9.)

#### 4.1.4 Stout Smearing

The last ingredient in our basic building blocks is smearing. Smearing has already been introduced, as stout smearing applied to gauge links in the fermion action. We can extend the same smearing technique to gauge links that make up our desired operators, which we have already done in the definition of the smeared tadpole factors  $\tilde{u}$ . It was inadmissible to smear fermions in the action (doing so spoils some crucial properties) but smearing the fermion operators is acceptable. This modification to our operators reduces the noise and excited state contamination.

We review stout-smearing,

$$\begin{aligned}
\mathcal{S}_\mu[G_\mu] &= \sum_{\pm\nu \neq \mu} \rho_{\mu\nu} \left( G_{\nu;x} G_{\mu;x+\hat{\nu}} G_{\nu;x+\hat{\mu}}^\dagger + G_{\nu;x-\hat{\nu}}^\dagger G_{\mu;x-\hat{\nu}} G_{\nu;x-\hat{\mu}} \right) \\
\mathcal{Q}_\mu[G_\mu] &= -\text{Im} \left( \mathcal{S}[G_\mu] G_\mu^\dagger - \frac{1}{3} \text{Tr} \mathcal{S}[G_\mu] G_\mu^\dagger \right) \\
G_\mu^{(n+1)} &= \exp(\mathcal{Q}_\mu[G_\mu^{(n)}]) G_\mu^{(n)},
\end{aligned} \tag{4.11}$$

where an unsmeared link  $G_\mu$  is turned into a set of staples  $\mathcal{S}_\mu$  which then generates an  $SU(3)$  group element  $\exp \mathcal{Q}$ , finally multiplying  $G_\mu$  to get  $G_\mu^{(1)}$ . This process is performed iteratively, up to 10 times for the gauge links making up operators, and 2 times for the gauge links appearing in the action. The weights  $\rho$  in each direction orthogonal to the original link are chosen differently as well, with  $\rho = .10$  in the operators and  $\rho = .14$  in the action. Any temporal component like  $\rho_{\mu 4}$  is set to zero in both cases.

The group structure of the gauge smearing procedure is crucial [23]. It ensures that these matrices do not need to be projected to  $SU(3)$  since they never leave the group; the lack of projection ensures differentiability, a key element in the Markov chain updating scheme used to generate gauge configurations  $G$ . This will be revisited in chapter 5.

### 4.1.5 Quark Smearing

The key to quark-field smearing is the Laplacian  $\nabla^2$ , which we have already seen as the spatial part of the Wilson term  $\partial^2$  [27]. We want to excite fewer high-energy modes, so by associating these higher energy modes with higher lying eigenvectors of the gauge-covariant Laplacian,

$$\Delta(\mathbf{x}, \mathbf{y}) = \sum_i \frac{G_i(\mathbf{x}) \delta_{\mathbf{x}+\hat{i}, \mathbf{y}} - 2\delta_{\mathbf{x}, \mathbf{y}} + G_{-i}(\mathbf{x}) \delta_{\mathbf{x}-\hat{i}, \mathbf{y}}}{2}, \tag{4.12}$$

we can project them out explicitly, with

$$\begin{aligned}
\psi_a(\mathbf{x}) \rightarrow \tilde{\psi}_a(\mathbf{x}) &= \sum_{\mathbf{y}} \mathcal{S}_{ab}(\mathbf{x}, \mathbf{y}) \psi_b(\mathbf{y}) \\
&= \sum_{\mathbf{y}} \Theta_{ab}(\sigma^2 + \Delta(\mathbf{x}, \mathbf{y})) \psi_b(\mathbf{y}),
\end{aligned} \tag{4.13}$$

using the Heaviside step-function of the Laplacian. In terms of the eigenvectors  $v_a^k(\mathbf{x})$  (associated with eigenvalue  $\lambda_k$ ) of the covariant Laplacian, the smearing kernel looks like

$$\mathcal{S}_{ab}(\mathbf{x}, \mathbf{y}) = \delta_{x_4, y_4} \sum_k w_k v_a^k(\mathbf{x}) v_b^{k*}(\mathbf{y}) \quad (4.14)$$

where the weight  $w_k$  is 1 whenever the associated eigenvalue  $\lambda_k < \sigma^2$  and zero otherwise. In theory the number of such eigenvectors could change depending on the gauge configuration, but truncating the sum at a sufficiently large value, identical across gauge configurations, has negligible effect on the correlation functions.

So, for a given gauge configuration  $G$ , we calculate the lowest  $N_\nu$  eigenvectors of  $\Delta[G]$  on each timeslice. These are then applied to the quark fields as a smearing kernel  $S$ :

$$\psi(\mathbf{x}) \rightarrow \tilde{\psi}(\mathbf{x}) = \sum_{\mathbf{y}} \delta_{x_4, y_4} \sum_{k=1}^{N_\nu} v_a^k(\mathbf{x}) v_b^{k*}(\mathbf{y}) \psi(\mathbf{y}) \quad (4.15)$$

Because of the gauge-covariant Laplacian, the smeared operators have all the same important symmetries as the unsmeared operators.

This also ends up playing a crucial role in the actual evaluation of the Grassmann variables *via* Berezin integration which lead to sums and products of inverse matrix elements of a large matrix  $M[\tilde{G}]$ . In chapter 5, we explore this issue in more detail. For now, we say tersely that matrix inverses are expensive and we save time by restricting ourselves to the LapH subspace only.

### 4.1.6 Basic Building Blocks

Combining the stout-smeared gauge links into our covariant displacements and covariant Laplacian allows us to write everything in terms of properly smeared, extended variables [28]. For baryons and mesons:

$$\begin{aligned} B_{\alpha\beta\gamma}^{(ijk)}(\mathbf{p}, t) &= \sum_{\mathbf{x}} e^{i\mathbf{p}\cdot\mathbf{x}} \epsilon_{abc} \left( \tilde{D}_i^{(p)} \tilde{\psi}_\alpha \right)_a(\mathbf{x}) \left( \tilde{D}_j^{(p)} \tilde{\psi}_\beta \right)_b(\mathbf{x}) \left( \tilde{D}_k^{(p)} \tilde{\psi}_\gamma \right)_c(\mathbf{x}) \\ M_{\alpha\beta}^{(ijk)}(\mathbf{p}, t) &= \sum_{\mathbf{x}} e^{i\mathbf{p}\cdot\left(\mathbf{x} + \frac{\mathbf{d}_\alpha + \mathbf{d}_\beta}{2}\right)} \delta_{ab} \left( \tilde{\chi}_\alpha \tilde{D}_i^{(p)\dagger} \right)_a(\mathbf{x}) \left( \tilde{D}_j^{(p)} \tilde{D}_k^{(p)} \tilde{\psi}_\beta \right)_b(\mathbf{x}) \end{aligned} \quad (4.16)$$

where the displacement length  $p$  is displayed explicitly. That is, we use

$$D_i^{(p)}(\mathbf{x}, \mathbf{x} + p\hat{\mathbf{i}}) = G_i(\mathbf{x}) G_i(\mathbf{x} + \hat{\mathbf{i}}) \cdots G_i(\mathbf{x} + (p-1)\hat{\mathbf{i}}) \quad (4.17)$$

and displace  $p = 2$  and  $3$  for baryons and mesons respectively. These are the most general possible operators; by taking particular combinations of  $i, j$  and  $k$ , and sometimes not displacing at all, we create the possibilities listed in Figures 4.1 and 4.2. The factor of  $\mathbf{d}_\alpha, \mathbf{d}_\beta$  of the total quark-antiquark displacements is to ensure a particular transformation under  $G$ -parity, a symmetry we will fully address later this chapter.

There are corresponding creation fields

$$\begin{aligned}\bar{B}_{\alpha\beta\gamma}^{(ijk)}(\mathbf{p}, t) &= \sum_{\mathbf{x}} e^{-i\mathbf{p}\cdot\mathbf{x}} \epsilon_{abc} \left( \tilde{\chi}_\alpha \tilde{D}_i^{(p)\dagger} \right)_a(\mathbf{x}) \left( \tilde{\chi}_\beta \tilde{D}_j^{(p)\dagger} \right)_b(\mathbf{x}) \left( \tilde{\chi}_\gamma \tilde{D}_k^{(p)\dagger} \right)_c(\mathbf{x}) \\ \bar{M}_{\alpha\beta}^{(ijk)}(\mathbf{p}, t) &= \sum_{\mathbf{x}} e^{-i\mathbf{p}\cdot\left(\mathbf{x} + \frac{\mathbf{d}_\alpha + \mathbf{d}_\beta}{2}\right)} \delta_{ab} \left( \tilde{\chi}_\alpha \tilde{D}_i^{(p)\dagger} \tilde{D}_j^{(p)\dagger} \right)_a(\mathbf{x}) \left( \tilde{D}_k^{(p)} \tilde{\psi}_\beta \right)_b(\mathbf{x}).\end{aligned}\tag{4.18}$$

Now that we have these basic structures, the rest of the chapter will be devoted to making them transform properly under the various discrete and rotational symmetries of interest. But first, we visit the topic of quark flavor.

## 4.2 Symmetries

### 4.2.1 Flavor Structure

Restoring flavor indices to all the quark and antiquark fields allows us to explore physical mesons and baryons. For a specific example, we can focus on flavor only and ignore rotations to make a pion operator; to make an isotriplet meson we first consider a light quark and antiquark, so  $f = \ell$  for both particles in  $M_{\alpha\beta}$ , to get  $M_{\alpha\beta IJ}$  with isospin indices  $I, J = 1, 2$  or up and down, or  $u$  and  $d$ . Then combine these with a  $\sigma_{IJ}^{I_3}$  for  $I_3 = -1, 0, 1$  to get an isotriplet  $I = 1$  nonstrange  $S = 0$  particle with isospin projection  $I_3$

$$\pi_{\alpha\beta}^{I_3} = \sigma_{IJ}^{I_3} \delta_{ab} \tilde{\chi}_{\alpha a I}(\mathbf{x}) \tilde{\psi}_{\beta b J}^\ell(\mathbf{x}),\tag{4.19}$$

for a single site operator, before projection into a definite momentum state.

Putting together a list of the mesonic flavor structures:

$$\begin{aligned}
\text{pion} \quad \pi_{\alpha\beta}^{I_3} &= \sigma_{IJ}^{I_3} \delta_{ab} \tilde{\chi}_{\alpha a I}^{\ell} \tilde{\psi}_{\beta b J}^{\ell} & I_3 = -1, 0, 1 \\
\text{kaon} \quad K_{\alpha\beta}^{I_3} &= \delta_{ab} \tilde{\chi}_{\alpha a}^s \tilde{\psi}_{\beta b I_3}^{\ell} & I_3 = -\frac{1}{2}, \frac{1}{2} \\
\text{eta} \quad \eta_{\alpha\beta} &= \delta_{IJ} \delta_{ab} \tilde{\chi}_{\alpha a I}^{\ell} \tilde{\psi}_{\beta b J}^{\ell} & I_3 = 0 \\
\text{phi} \quad \phi_{\alpha\beta} &= \delta_{ab} \tilde{\chi}_{\alpha a}^s \tilde{\psi}_{\beta b}^s & I_3 = 0.
\end{aligned} \tag{4.20}$$

A few brief points on this list, before we move onto the baryons. First, the antikaon is not listed, we will soon see these are defined by a transformation of our kaon operators. Second, the usual  $\eta, \eta'$  and  $\phi, \omega$  mesons are particular combinations of  $\bar{u}u + \bar{d}d$  and  $\bar{s}s$ , linear combinations of the above operators labeled as  $\eta, \phi$  which really mean purely light isoscalar and purely strange isoscalar. Lastly, the second point demonstrates these names refer to *only* the flavor structure – pions and kaons are pseudoscalars, but the above objects do not have these transformation properties. To get physical particles we will continue to nail down further symmetries which constrain the states these operators excite. A physical pion, for example, will be a version of the above operator that is also a negative parity and  $G$ -parity eigenstate, and which is invariant under rotations.

Putting together a list of the baryonic flavor structures:

$$\begin{aligned}
\text{nucleon} \quad N_{\alpha\beta\gamma}^{I_3} &= D_{IJK}^{I_3} \epsilon_{abc} \tilde{\psi}_{\alpha a I}^{\ell} \tilde{\psi}_{\beta b J}^{\ell} \tilde{\psi}_{\gamma c K}^{\ell} & I_3 = -\frac{1}{2}, \frac{1}{2} \\
\text{delta} \quad \Delta_{\alpha\beta\gamma}^{I_3} &= Q_{IJK}^{I_3} \epsilon_{abc} \tilde{\psi}_{\alpha a I}^{\ell} \tilde{\psi}_{\beta b J}^{\ell} \tilde{\psi}_{\gamma c K}^{\ell} & I_3 = -\frac{3}{2}, -\frac{1}{2}, \frac{1}{2}, \frac{3}{2} \\
\text{lambda} \quad \Lambda_{\alpha\beta\gamma} &= \delta_{IJ} \epsilon_{abc} \tilde{\psi}_{\alpha a I}^{\ell} \tilde{\psi}_{\beta b J}^{\ell} \tilde{\psi}_{\gamma c}^s & I_3 = 0 \\
\text{sigma} \quad \Sigma_{\alpha\beta\gamma}^{I_3} &= \sigma_{IJ}^{I_3} \epsilon_{abc} \tilde{\psi}_{\alpha a I}^{\ell} \tilde{\psi}_{\beta b J}^{\ell} \tilde{\psi}_{\gamma c}^s & I_3 = -1, 0, 1 \\
\text{xi} \quad \Xi_{\alpha\beta\gamma}^{I_3} &= \epsilon_{abc} \tilde{\psi}_{\alpha a I_3}^{\ell} \tilde{\psi}_{\beta b}^s \tilde{\psi}_{\gamma c}^s & I_3 = -\frac{1}{2}, \frac{1}{2} \\
\text{omega} \quad \Omega_{\alpha\beta\gamma} &= \epsilon_{abc} \tilde{\psi}_{\alpha a}^s \tilde{\psi}_{\beta b}^s \tilde{\psi}_{\gamma c}^s & I_3 = 0
\end{aligned} \tag{4.21}$$

where the coefficients  $D$  result from the projection to the doublet part of  $2 \otimes 2 \otimes 2 = 4 \oplus 2 \oplus 2$ . There are two possibilities here, but they are redundant under permutation of indices. That is, we take (ignoring overall normalizations)

$$\begin{aligned}
D_{IJK}^{\frac{1}{2}} &= \delta_{Iu} \delta_{Ju} \delta_{Kd} - \delta_{Id} \delta_{Ju} \delta_{Ku} \\
D_{IJK}^{-\frac{1}{2}} &= \delta_{Iu} \delta_{Jd} \delta_{Kd} - \delta_{Id} \delta_{Jd} \delta_{Ku}.
\end{aligned} \tag{4.22}$$

There is only one quartet, so  $Q$  is fully determined. For reference these are

$$\begin{aligned}
Q_{IJK}^{\frac{3}{2}} &= \delta_{Iu}\delta_{Ju}\delta_{Ku} \\
Q_{IJK}^{\frac{1}{2}} &= \frac{1}{\sqrt{3}} (\delta_{Id}\delta_{Ju}\delta_{Ku} + \delta_{Iu}\delta_{Jd}\delta_{Ku} + \delta_{Iu}\delta_{Ju}\delta_{Kd}) \\
Q_{IJK}^{-\frac{1}{2}} &= \frac{1}{\sqrt{3}} (\delta_{Id}\delta_{Jd}\delta_{Ku} + \delta_{Id}\delta_{Ju}\delta_{Kd} + \delta_{Iu}\delta_{Jd}\delta_{Kd}) \\
Q_{IJK}^{-\frac{3}{2}} &= \delta_{Id}\delta_{Jd}\delta_{Kd}.
\end{aligned} \tag{4.23}$$

For all of the above operators we have given each possible  $I_3$ . Because of isospin symmetry, the energies do not actually depend on  $I_3$ , so the energies in the  $I = 1, I_3 = -1$  sector should be identical to the  $I = 1, I_3 = 1$ , assuming other quantum numbers are identical. However, we will end up requiring different  $I_3$  anyway, because we will want to combine these operators into multi-hadron objects that have definite total  $I = I^{(1)} + I^{(2)}$  and  $I_3$ . Two-hadron operators will be addressed in more detail later.

### 4.2.2 G-Parity

$G$ -parity is a transformation that combines charge conjugation with isospin rotation. Charge conjugation itself is not a symmetry of many states we consider: *e.g.*, although  $\pi^0$  is electrically neutral and transforms into itself, the other two pions switch under charge conjugation. We can “switch back” by essentially interchanging  $u$  and  $d$ , *via* isospin rotation:

$$U_{IR}\psi_I^\ell U_{IR}^\dagger = e^{i\pi\frac{\sigma^2}{2}}\psi_I^\ell = i\sigma_{IJ}^2\psi_J^\ell \tag{4.24}$$

which sends  $u \rightarrow d \rightarrow -u$  and  $\bar{u} \rightarrow \bar{d} \rightarrow -\bar{u}$ . Of course  $s$  is left invariant. By combining this with charge conjugation

$$\begin{aligned}
U_C\psi_\alpha U_C^\dagger &= \bar{\psi}_\beta C_{\beta\alpha}^\dagger = \bar{\psi}_\beta(\gamma_4\gamma_2)_{\beta\alpha}^\dagger \\
U_C\bar{\psi}_\alpha U_C^\dagger &= -C_{\alpha\beta}\psi_\beta = -(\gamma_4\gamma_2)_{\alpha\beta}\psi_\beta \\
U_C G_i U_C^\dagger &= G_i^*
\end{aligned} \tag{4.25}$$

and replacing barred fields in favor of  $\chi = \bar{\psi}\gamma_4$  we find these properties for  $G$ -parity  $U_G = U_{IR}U_C$ :

$$\begin{aligned}
U_G (D_j \psi_{\alpha I}^\ell)_a U_G^\dagger &= i\sigma_{IJ}^2 \left( \chi_{\beta J}^\ell D_j^\dagger \right)_a \gamma_{\beta\alpha}^2 \\
U_G (D_j \psi_\alpha^s)_a U_G^\dagger &= - \left( \chi_\beta^s D_j^\dagger \right)_a \gamma_{\beta\alpha}^2 \\
U_G \left( \chi_{\alpha J}^\ell D_j^\dagger \right)_a U_G^\dagger &= i\sigma_{IJ}^2 \gamma_{\alpha\beta}^2 (D_j \psi_{\beta I}^\ell)_a \\
U_G \left( \chi_\alpha^s D_j^\dagger \right)_a U_G^\dagger &= -\gamma_{\alpha\beta}^2 (D_j \psi_\beta^s)_a.
\end{aligned} \tag{4.26}$$

Technically, these results depend on the choice of representation for the  $\gamma$ -matrices. However it turns out the above is true for multiple common choices, the Dirac-Pauli, Weyl-Chiral, and DeGrand-Rossi conventions. So, for each meson operator (except the kaon) we can define two sectors of opposite  $G$ -parity,

$$M \rightarrow M^\pm = M \pm U_G M U_G^\dagger. \tag{4.27}$$

In the case of the kaon, we simply define the  $\bar{k}$  as its  $G$ -parity conjugate,

$$\bar{K} = U_G K U_G^\dagger. \tag{4.28}$$

### 4.2.3 Time-Reversal

It turns out that the time-reversed baryon operator has opposite parity, and not necessarily the same energy. The mesons, however, are candidates for time-reversal invariance because the forward- and backward-propagating modes have the same parity. In fact, Hermiticity of the correlator can be connected to time-reversal invariance for Euclidean objects. In the case of baryons, time reversal is tied up with parity and asking for the former gives us a procedure for constructing the latter. For mesons the two are independent, but we can increase statistics by requiring it. To really take advantage of the increase, we must be sensitive to forward- and backward-propagating modes, which is only plausible for the lightest meson channels. Therefore, the increase in statistics is not so relevant for the baryons nor most mesons, outside of those in the  $A_{1u}, A_{1u}^\pm$  channels. (Though we still construct the baryons accordingly, because of the relationship to parity.)

We would like the correlator to satisfy

$$C_{ij}^g(t) = -C_{ji}^{u\dagger}(T-t) \quad (4.29)$$

( $g, u$  refer to parity plus and minus, respectively) for baryons, and

$$C_{ij}(t) = C_{ij}(T-t) \quad (4.30)$$

for mesons. The latter case is simple; we can take operators of either class  $M_{\pm} = M \pm U_T M U_T^{\dagger}$ . There is no reason to use one of these over another, but it seemed that the odd operators were less noisy on small lattices. The symmetry operation  $U_T$ , *restricted* time-reversal, is unitary and defined by

$$\begin{aligned} U_T (D_j \psi_{\alpha})_a(\mathbf{x}, x_4) U_T^{\dagger} &= (\gamma_4 \gamma_5)_{\alpha\beta} (D_j \psi_{\beta})_a(\mathbf{x}, T - x_4) \\ U_T \left( \chi_{\alpha} D_j^{\dagger} \right)_a(\mathbf{x}, x_4) U_T^{\dagger} &= \left( \chi_{\beta} D_j^{\dagger} \right)_a(\mathbf{x}, T - x_4) (\gamma_4 \gamma_5)_{\beta\alpha}. \end{aligned} \quad (4.31)$$

Again, the baryon time-reversal behavior will follow automatically from our method of constructing opposite-parity operators. This will be discussed further in the next section, but, for reference, baryons satisfy equation 4.31 if, for an even operator like

$$B^{\Lambda_g \lambda} = d_{\alpha\beta\gamma}^{\Lambda\lambda} B_{\alpha\beta\gamma}, \quad (4.32)$$

the odd operator is constructed according to

$$B^{\Lambda_u \lambda} = C_{\lambda\lambda'}^{(\Lambda)} d_{\alpha\beta\gamma}^{*\Lambda\lambda'} (\gamma_{\alpha\alpha'}^2 \gamma_{\beta\beta'}^2 \gamma_{\gamma\gamma'}^2 B_{\alpha'\beta'\gamma'}) \quad (4.33)$$

for baryons of opposite parity. The coefficients  $C$  are found to be:

$$\begin{aligned} C_{12} = -C_{21} &= 1 && \text{for } G_1, G_2 \\ C_{14} = -C_{41} = C_{32} = -C_{23} &= 1 && \text{for } H \end{aligned} \quad (4.34)$$

with all other entries zero. (The irreducible representations  $G_1, G_2$  and  $H$  are discussed in the following section.)

#### 4.2.4 Cubic Symmetry

The last symmetry we consider is rotational, with spatial inversion. In typical formulations of field theory, we ask for objects that transform irreducibly under  $SO(3)$ , the little group of a reference momentum vector  $(0, 0, 0, 1)$  for massive particles. However, in our system we have only the discrete symmetries of a cube, the octahedral group  $O$ . Therefore, we use the irreducible representations of this group at rest, and for a moving frame we use irreps of the relevant little group. We have been leaving all spinor indices free on objects like  $M_{\alpha\beta}$  because the plan is to eventually project these into the irreducible representations of cubic, rather than continuous, rotations.

The octahedral group  $O$  is made up of the rotations that leave a cube invariant,

$$\begin{array}{ll}
E & \text{Identity} \\
R_{\alpha}^{\frac{2n}{3}\pi} & \text{Rotations around corners by } \frac{2\pi}{3}, \frac{4\pi}{3} \\
R_x^{\frac{2n+1}{2}\pi} & \text{Rotations around face normals by } \frac{\pi}{2}, \frac{3\pi}{2} \\
R_x^{\pi} & \text{Rotations around face normals by } \pi \\
R_a^{\pi} & \text{Rotations around edge by } \pi.
\end{array} \tag{4.35}$$

The lines are separated by conjugacy class, and each axis is displayed in Figure 4.3. Incorporating parity leads to the point octahedral group  $O_h$ , which is accomplished with an additional group element  $I$ , for spatial inversion, that doubles the number of conjugacy classes. So far these are single-valued representations which only account for integer spin, but they can be made projective by adding a further element to  $O$  or  $O_h$  called  $\bar{E}$ . Now,  $E$  represents a rotation by  $4\pi$ , and  $\bar{E}$  is  $2\pi$ . The additional element (really, additional set of elements) creates three new conjugacy classes in the case of  $O$ , and six more for  $O_h$ .

So, the irreducible representations of  $O_h^D$  (the double point octahedral group) are labeled by  $\Lambda$ , and there are sixteen of them because there are sixteen conjugacy classes; for each parity, there are five integer-spin classes and three half-integer classes. Following the Mulliken convention, these are labeled as

$$A_{1g/u}, A_{2g/u}, E_{g/u}, T_{1g/u}, T_{2g/u} \tag{4.36}$$

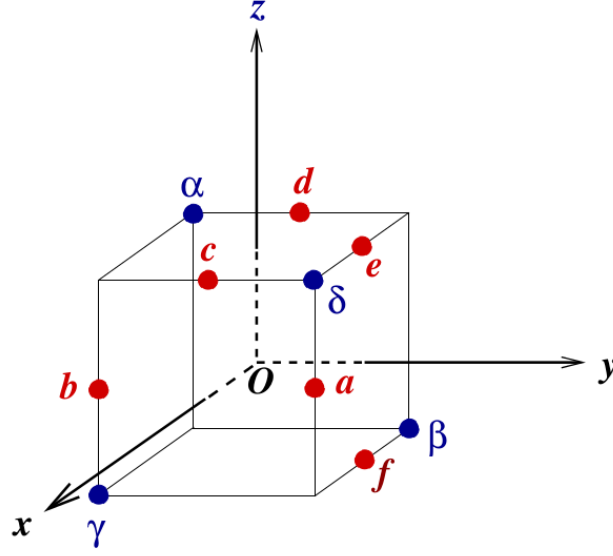


Figure 4.3: The rotation axes for each element of  $O$ . Early Latin letters (a-e) indicate edges, late Latin (x, y, z) indicate face normals, and Greek indicate corners.

for the usual representations and

$$G_{1g/u}, G_{2g/u}, H_{g/u} \quad (4.37)$$

for the double-covers. (Again, subscript  $g$  and  $u$  indicate parity  $+$  and  $-$ , respectively.)

Because we have given up spin-symmetry, in principal it is very hard to relate states on the lattice with physical particles. For low spin, however, it is not so difficult, in practice. One can take an irreducible representation of  $SO(3)$  (which becomes reducible if we consider only a few specific rotations), and find the symmetry sectors of  $O_h^D$  to which it subduces. Table 4.1 gives the number of occurrences  $n$  of each  $O_h^D$  irrep for a given  $J$ .

We explicitly build these representations, group-element by group-element, and use the matrices to project our operators into specific symmetry sectors. This effectively builds the coefficient  $d_{\alpha\beta\gamma}$ , mentioned earlier, which ends up depending on displacement type. We detail the procedure in section 4.2.6.

$J$	$A_1$	$A_2$	$E$	$T_1$	$T_2$	$G_1$	$G_2$	$H$
0	1	0	0	0	0	0	0	0
$\frac{1}{2}$	0	0	0	0	0	1	0	0
1	0	0	0	1	0	0	0	0
$\frac{3}{2}$	0	0	0	0	0	0	0	1
2	0	0	1	0	1	0	0	0
$\frac{5}{2}$	0	0	0	0	0	0	1	1

Table 4.1: Number of occurrences of irreducible representations of the double-octahedral group in the subduction of  $SO(3)$ . This table continues with many of the irreps showing up multiple times for any particular  $J$ .

### 4.2.5 Moving Frames

At rest, we used representations of  $O_h^D$ , but in moving frames we need representations of the subgroup of  $O_h^D$  that leaves a certain momentum vector invariant. That is, we can use operators with total momentum  $(n, 0, 0)$ ,  $(n, n, 0)$  and  $(n, n, n)$ , as well as the various permutations and inversions ( $\pm$ ). For each irrep of  $O_h^D$ , the little groups  $C_{4v}$ ,  $C_{2v}$  and  $C_{3v}$  have a set of irreducible representations, as outlined in Table 4.2

Again these are built explicitly, and used to project onto the relevant sector. It is important to remember that parity is no longer a good symmetry of these operators, because they are moving with a specific nonzero total momentum.

### 4.2.6 Projection onto Symmetry Sectors

In order to find the coefficients  $d_{\alpha\beta\gamma}$  or  $d_{\alpha\beta}$  for baryon and meson operators for each displacement type, irrep, and irrep row we follow the following procedure, detailed in [26]:

- (1) Assemble a list of operators that transform into each other under rotations. For single-site operators this is trivial, consisting only of all possible spin indices. For displaced operators, the directions must be taken into account as well.
- (2) Reduce this list to the independent operators (that is, some of the above operators will be related under permutation of identical particles)
- (3) Project each into a specific row of each irrep
- (4) Apply lowering operator to get all other rows
- (5) Recover the coefficients  $d$  by reading them off the resulting linear combinations

$\Lambda(O_h)$	$\Lambda(O_h) \downarrow C_{4v}$	$\Lambda(O_h)$	$\Lambda(O_h) \downarrow C_{3v}$	$\Lambda(O_h)$	$\Lambda(O_h) \downarrow C_{2v}$
$A_{1g}$	$A_1$	$A_{1g}$	$A_1$	$A_{1g}$	$A_1$
$A_{1u}$	$A_2$	$A_{1u}$	$A_2$	$A_{1u}$	$A_2$
$A_{2g}$	$B_1$	$A_{2g}$	$A_2$	$A_{2g}$	$B_2$
$A_{2u}$	$B_2$	$A_{2u}$	$A_1$	$A_{2u}$	$B_1$
$E_g$	$A_1 \oplus B_1$	$E_g$	$E$	$E_g$	$A_1 \oplus B_2$
$E_u$	$A_2 \oplus B_2$	$E_u$	$E$	$E_u$	$A_2 \oplus B_1$
$T_{1g}$	$A_2 \oplus E$	$T_{1g}$	$A_2 \oplus E$	$T_{1g}$	$A_2 \oplus B_1 \oplus B_2$
$T_{1u}$	$A_1 \oplus E$	$T_{1u}$	$A_1 \oplus E$	$T_{1u}$	$A_1 \oplus B_1 \oplus B_2$
$T_{2g}$	$B_2 \oplus E$	$T_{2g}$	$A_1 \oplus E$	$T_{2g}$	$A_1 \oplus A_2 \oplus B_1$
$T_{2u}$	$B_1 \oplus E$	$T_{2u}$	$A_2 \oplus E$	$T_{2u}$	$A_1 \oplus A_2 \oplus B_2$
$G_{1g/u}$	$G_1$	$G_{1g/u}$	$G$	$G_{1g/u}$	$G$
$G_{2g/u}$	$G_2$	$G_{2g/u}$	$G$	$G_{2g/u}$	$G$
$H_{g/u}$	$G_1 \oplus G_2$	$H_{g/u}$	$F_1 \oplus F_2 \oplus G$	$H_{g/u}$	$2G$

Table 4.2: Subduction of irreps of  $O_h^D$  to the little group of on-axis, cubic-diagonal, and planar-diagonal momenta.

The projection formula is

$$O_i^{\Lambda\lambda=1}(\mathbf{p}, t) = \frac{d_\Lambda}{|G|} \sum_{R \in G} \Gamma_{11}^{(\Lambda)}(R) U_R O_i(\mathbf{p}, t) U_R^\dagger, \quad (4.38)$$

which projects onto the  $\lambda = 1$  row, and then is lowered to other rows via

$$O_i^{\Lambda\mu}(\mathbf{p}, t) = \frac{d_\Lambda}{|G|} \sum_{R \in G} \Gamma_{\mu 1}^{(\Lambda)}(R) U_R O_i^{\Lambda 1}(\mathbf{p}, t) U_R^\dagger. \quad (4.39)$$

Here, the symbol  $d_\Lambda$  counts the dimension (number of rows) of the irrep, and  $|G|$  is the order of the relevant group. In each case the relevant group is  $O_h^D$  or one of its subgroups for moving frames. Like with isospin projection, operators of different irrep-row will have zero correlation, and result in identical energies, so the only reason to use multiple rows is in constructing multi-hadron operators.

### 4.3 Multi-Hadron Operators

We quickly detail the procedure for multiple hadrons. The key point is that we combine operators of specific total momentum  $\mathbf{p}$ , like

$$O(\mathbf{P}, t) = A(\mathbf{p}_1, t) B(\mathbf{p}_2, t) \quad (4.40)$$

rather than taking a so-called “local” operator

$$O(\mathbf{P}, t) = \sum_{\mathbf{x}} e^{i\mathbf{P} \cdot \mathbf{x}} A(\mathbf{x}) B(\mathbf{x}). \quad (4.41)$$

It turns out that nonlocal multiparticle operators have generally less excited state contamination than local multiparticle operators. We make only meson-meson and baryon-meson two-hadron operators, which greatly simplifies the number of possibilities. (Baryon-baryon operators are too heavy for us to consider here.)

Symmetries like parity and  $G$ -parity combine multiplicatively when appropriate. Strangeness combines additively, and operators must be made to transform under *total* isospin  $I$  via standard Clebsh-Gordan coefficients. The only slight complication comes from rotational symmetries, which we solve by reapplying the above procedure to project a general two-hadron operator into the desired irrep.

The last aspect to consider is  $G$ -parity. When the individual hadrons are irreducible under  $G$ -parity the two-hadron state is automatically irreducible, but it can be the case that the two individual hadrons do *not* create  $G$ -parity eigenstates. When neither constituent operator is irreducible, it is sometimes true that the total multihadron operator can be made to transform irreducibly. For example, we project operators like  $K\bar{K}$  into positive and negative  $G$ -parity sectors, even though this is not a good quantum number for the individual  $K$  and  $\bar{K}$ .

# Chapter 5

## Monte Carlo Sampling

In this chapter, we discuss Monte Carlo sampling as a means of performing the path integral. The Dirac matrix is introduced for its use in the probability weight, and fermions are discussed in detail, as well as quark lines, and their efficient evaluation via noise dilution in the LapH-subspace. We outline the process of configuration generation, with the Rational Hybrid Monte Carlo method, and our Metropolis-Hastings updating scheme.

### 5.1 Fermions and Correlators

A prototypical correlator between operators  $A$  and  $B$ , each made out of quark fields and gauge links, takes the form

$$\langle A(t)B^\dagger \rangle = \frac{1}{Z} \int D\bar{\psi} D\psi DGA[\bar{\psi}(t), \psi(t), G(t)] B^*[\bar{\psi}(0), \psi(0), G(0)] e^{-S} \quad (5.1)$$

with  $S$  defined in Equation 3.8. Looking at the form of

$$S = S_f + S_g = \int d^4x \bar{\psi} M[G] \psi + S_g \quad (5.2)$$

we see that  $S_f$  is quadratic in the fermion fields, which are completely absent in  $S_g$ . Because of this, we can integrate out the quarks exactly which dodges the issue of numerically representing Grassmann numbers. It is well-known<sup>1</sup> that integrating over Grassmann numbers in a Gaussian  $e^{-(\bar{\psi}, M\psi)}$  results in a matrix determinant,  $\det M$ ;

---

<sup>1</sup>See any field theory text, *e.g.* [29].

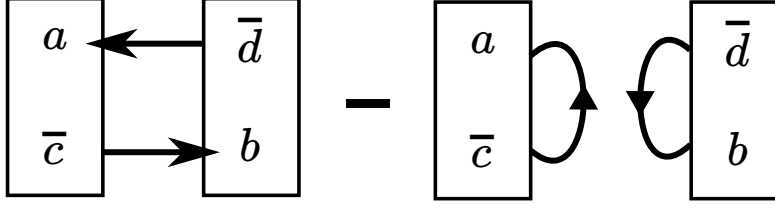


Figure 5.1: Diagram of possible meson correlator. Each line represents a particular element of the Dirac matrix inverse.

when additional Grassmann numbers appear in the integrand, we find the same factor of  $\det M$ , supplemented with additional factors of  $M^{-1}$  matrix-elements. Specifically,

$$\int D\bar{\psi} D\psi \psi_a \bar{\psi}_b e^{-(\bar{\psi}, M\psi)} = M_{ab}^{-1} \det M, \quad (5.3)$$

where we have combined *every* index on  $\psi$  into one that iterates over everything. For example, if the compound index  $a$  contains the flavor  $s$  and  $b$  contains  $\ell$ , the relevant element of  $M^{-1}$  is guaranteed to be zero. This is the simplest nontrivial case; a more typical example is a meson correlator

$$\langle \psi_a \psi_b \bar{\psi}_c \bar{\psi}_d \rangle = (M_{ad}^{-1} M_{bc}^{-1} - M_{ac}^{-1} M_{bd}^{-1}) \det M. \quad (5.4)$$

Each meson operator contributes one  $\psi$  and one  $\bar{\psi}$  to this correlator. For the labelling choice in Figure 5.1 we can see that the matrix elements  $M^{-1}$  contain both forward/backward lines and same-time lines. Often, only some of the quark lines contribute to a given operator. For example, in the case of single mesons, only isoscalars have same-time quark lines.

All of the above is rather generic. In practice we use  $\chi$  fields rather than  $\bar{\psi}$ , for example, which means there should be a  $\gamma_4$  floating around. Additionally, our actual fields are smeared and displaced. All these operations take the form of linear operators like  $g_{ab}$  that are applied to the above objects. Therefore, they can be applied to our elements of  $M^{-1}$  rather trivially. So, any correlator can be decomposed into linear combinations of products of quark lines. For forward quark lines

$$Q_{jk}(t, t_0) = D_j \mathcal{S} \Omega^{-1}(t, t_0) \mathcal{S} D_k^\dagger \quad (5.5)$$

must be calculated, where we prefer the use of  $\Omega = \gamma_4 M$  rather than the Dirac matrix itself. Remember that each of these  $Q_{jk}(t, t_0)$ 's is a matrix in color-spin-position space. (We ignore flavor and isospin indices because we can only have quark lines between operators of the same flavor or isospin.) For backward quark lines

$$\bar{Q}_{jk}(t, t_0) = (\gamma_5 \gamma_4 Q_{jk}(t, t_0) \gamma_4 \gamma_5)^* \quad (5.6)$$

and for same time quark lines, we use the forward line with identical time indices as  $Q_{jk}(t_0, t_0)$ .

Each correlator decomposes into quark lines which each contain inverses of the Dirac matrix, in the form  $\Omega^{-1}$ . It turns out that LapH-smearing our quarks has important consequences for the inversion procedure.

### 5.1.1 Matrix Inversion

Any matrix inverse  $M^{-1}$  can be estimated by iteratively approximating  $\mathbf{x}_i$ , the solution to  $M\mathbf{x}_i = \mathbf{e}_i$ , for each basis vector  $\mathbf{e}_i$ . This is made stochastic (Monte Carlo within Monte Carlo) by replacing the basis vector  $\mathbf{e}_i$  with a *noise vector*  $\boldsymbol{\eta}$ , of random elements. With only a few requirements, iteratively solving for  $\mathbf{x}$  in  $M\mathbf{x} = \boldsymbol{\eta}$  for each  $\boldsymbol{\eta}$  yields

$$\langle x_i \eta_j^* \rangle = \langle M_{ik}^{-1} \eta_k \eta_j^* \rangle = M_{ik}^{-1} \langle \eta_k \eta_j^* \rangle = M_{ij}^{-1} \quad (5.7)$$

for an estimate  $M^{-1}$ . We note that the expectation value  $\langle \cdot \rangle$  here is taken over a set of noise vectors  $\{\boldsymbol{\eta}\}$  rather than configurations  $\{G\}$  as before. These randomly generated noise vectors must satisfy

$$\begin{aligned} \langle \eta_i \rangle &= 0 \\ \langle \eta_i \eta_j^* \rangle &= \delta_{ij}. \end{aligned} \quad (5.8)$$

There are many ways to accomplish this, and our noise vector elements  $\eta_i$  are chosen randomly from the set  $\{1, i, -1, -i\}$ , referred to as  $Z_4$  noise. It is easy to show that the variance in our estimate for  $M^{-1}$  goes like  $\frac{1}{N_n}$ , for  $N_n$  noise vectors  $\boldsymbol{\eta}$ .

### 5.1.2 Noise Dilution

We can dramatically decrease the variance in this estimate by projecting our noise vectors into several distinct subspaces. That is, one makes any complete set of projectors  $\{P^{(r)}\}$  to solve  $M\mathbf{x}^{(r)} = P^{(r)}\boldsymbol{\eta}$  and form

$$\langle x_i^{(r)} P_{jk}^{(r)} \eta_k^* \rangle = M_{ij}^{-1} \quad (5.9)$$

to get the inverse. By diluting the noise vectors in this way we reduce the variance in our estimate of  $M^{-1}$ . For example, fully diluting these  $\boldsymbol{\eta}$  should completely eliminate the variance; this corresponds to introducing a set of projectors  $P_{ij}^{(r)} = \delta_{ir}\delta_{jr}$ , which serve to turn a noise vector  $\boldsymbol{\eta}$  into the basis vector  $\mathbf{e}_r$ , thereby achieving exact inversion. A smaller set of projectors will save computational time at the expense of increasing the variance.

We consider three sets of projectors, referred to as *full*, *interlace-8* and *interlace-16*. The former we have already discussed, and the latter two correspond to chopping up the identity into 8 or 16 subspaces. We do not have to necessarily dilute in every index, and in fact we will dilute separately in time, spin, and LapH eigenvector indices. The last of these is effectively a mix of spatial and color indices, found after diagonalizing the covariant Laplacian. We see a dramatic cost reduction by only diluting in the LapH subspace *via* the stochastic LapH method [5].

### 5.1.3 Factorization

The diluted noise vectors  $\boldsymbol{\eta}^{(r)}$  allow us to find  $M^{-1}$  by first approximately solving  $\Omega\boldsymbol{\phi}^{(r)} = \boldsymbol{\eta}^{(r)}$  for  $\boldsymbol{\phi}^{(r)}$ . So, we can replace our elements of  $M^{-1}$  in Equation 5.9 with combinations of these source and sink noise vectors. The original operators were smeared and displaced so we must apply this smearing and displacement to these very noise vectors, as

$$Q_{a\alpha j; b\beta k}(\mathbf{x}, \mathbf{y}, U) = \frac{1}{N_n} \sum_{n=1}^{N_n} \sum_r \varphi_{a\alpha j}^{(r)n}(\mathbf{x}, U) \varrho_{b\beta k}^{(r)n}(\mathbf{y}, U)^*. \quad (5.10)$$

The fields  $\varrho$  in the above are made by applying a couple of linear operators to our noise vectors  $\boldsymbol{\eta}$ . Specifically, a large list of noise vectors  $\boldsymbol{\eta}^n$  lying in the LapH subspace

are acted upon by

$$\boldsymbol{\eta}^n \rightarrow P^{(r)} \boldsymbol{\eta}^n \rightarrow D_k V_s P^{(r)} \boldsymbol{\eta}^n = \varrho_k^{(r)n} \quad (5.11)$$

to first dilute, move to spatial and color indices (from LapH-eigenvector indices) and lastly covariantly displace. Simultaneously, we are receiving from each  $\boldsymbol{\eta}$  a corresponding  $\boldsymbol{\phi}$  and likewise smearing and displacing these:

$$\boldsymbol{\eta}^{(r)n} \rightarrow \Omega \boldsymbol{\phi}^{(r)n} = V_s \boldsymbol{\eta}^{(r)n} \quad (5.12)$$

is solved to find  $\boldsymbol{\phi}^{(r)n}$ , which defines  $\varphi$  as

$$\boldsymbol{\phi}^{(r)n} \rightarrow D_j \mathcal{S} \boldsymbol{\phi}^{(r)n} = \varphi_j^{(r)n}. \quad (5.13)$$

One notes that the factors of  $V_s$  and  $\mathcal{S}$  appear asymmetrically – this is because the vectors  $\boldsymbol{\eta}$  lie entirely within the LapH subspace, whereas the vectors  $\boldsymbol{\phi}$  lie automatically in the whole space.

Each quark line is calculated by combining the source- and sink-vectors, and the correlator is made by combining all the necessary quark lines. A key point is that any correlator will end up *factorizing*, allowing us to calculate all the source- and sink-vectors, or line-ends, for each operator and then keeping them on disk. Thus, the fermionic operators can be viewed in the same way as gluonic operators, with a mere complex number (or set of complex numbers) for each configuration. The only difference is the computational expense required in forming these  $\varphi$  and  $\varrho$  fields. By forming these line-ends for a large number of operators, they can be quickly combined into quark lines which can in turn be combined into correlators. For example, a typical baryon correlator becomes

$$\begin{aligned} C(t - t_0) = & B(\varphi_1, \varphi_2, \varphi_3; t) (B(\varrho_1, \varrho_2, \varrho_3; t_0) - B(\varrho_1, \varrho_3, \varrho_2; t_0) \\ & - B(\varrho_2, \varrho_1, \varrho_3; t_0) - B(\varrho_3, \varrho_2, \varrho_1; t_0) + B(\varrho_2, \varrho_3, \varrho_1; t_0) + B(\varrho_3, \varrho_1, \varrho_2; t_0))^* \end{aligned} \quad (5.14)$$

where we have used an extremely condensed notation. This can be viewed pictorially, as shown in Figure 5.2.

The factorization is particularly advantageous for large sets of operators and correlation matrices. Each individual operator becomes associated with a set of complex numbers, the line-ends, which are combined with the line-ends of a different operator

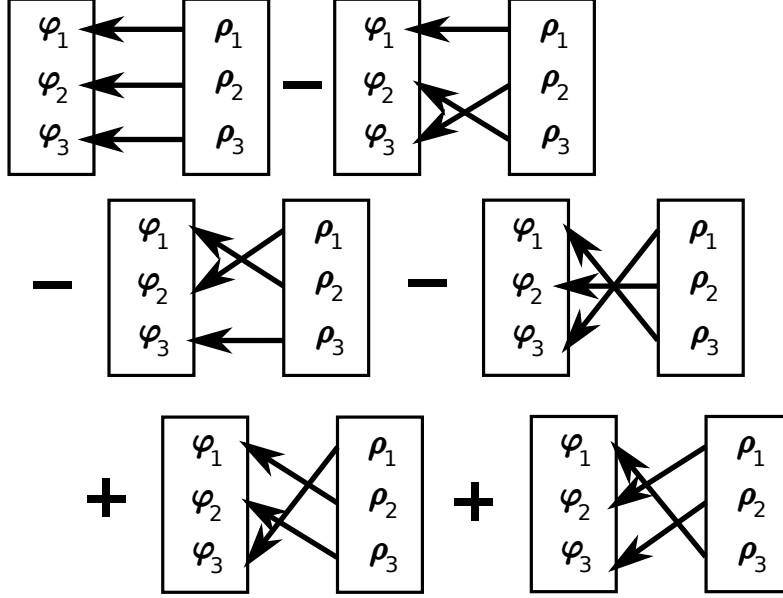


Figure 5.2: Diagram of possible baryon correlator. Before, each line represented an element of the Dirac matrix inverse. Now, we see that these inverses are estimated by multiplying together functions of source and sink vectors.

to form the correlator itself.

## 5.2 Importance Sampling

Given the previous discussion of Grassmann integration, we see that the remaining integral takes the form

$$\langle A \rangle = \frac{1}{Z} \int DGF_A [M^{-1}[G]] \det M[G] e^{-S_g[G]}. \quad (5.15)$$

Our gauge fields give  $N^4 \times 4 \times 8$  variables to integrate in, using 4 directions and 8 parameters for a  $3 \times 3$  unitary matrix of determinant 1. The general procedure in such a situation is to use Monte Carlo sampling, detailed very well in [30], where we take a statistical sampling of points in the integration region and perform a weighted average. However, not all of these points contribute significantly to the result. Specifically, field configurations that are associated with particularly large actions are practically irrelevant. One can improve the estimate by using *importance sampling*, where the

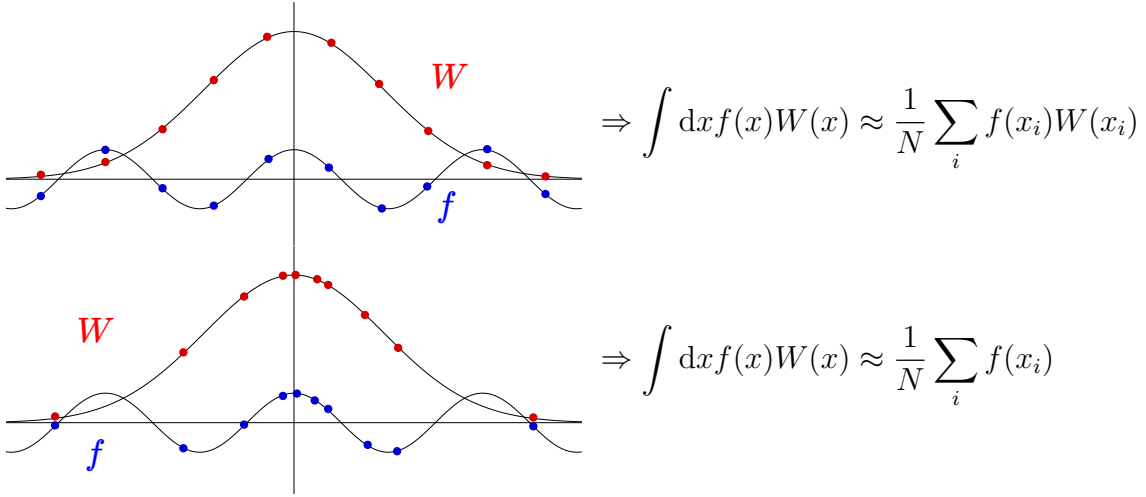


Figure 5.3: Comparing uniformly distributed sampling (above) to importance sampling (below). The average of  $f$  weighted by  $W$  in the former case becomes merely the average of  $f$ , at points distributed according to  $W$ , in the latter case.

sampling points themselves are distributed according to  $\det M[G]e^{-S_g}$ , and we perform a simple average over  $F_A$ , which represent the particular combination of quark lines that correspond to a given pair of operators.

Therefore, we are sampling according to

$$W = \det M[G]e^{-S_g[G]} \quad (5.16)$$

rather than merely  $e^{-S}$ . That a determinant must be evaluated rather than just the exponential changes the computational load, but not the conceptual one. We merely trade a list of  $G, \bar{\psi}$  and  $\psi$  sampled according to  $e^{-S}$  for a list of  $G$  sampled according to  $\det M e^{-S_g}$ . Soon, we will discuss approximations and modifications to this determinant, but first we must detail the configuration generation process itself.

## 5.3 Configuration Generation

### 5.3.1 Markov Chains

In order to generate configurations of gauge-links distributed according to  $W$  we exploit stochastic Markov chains. That is, if we can find a stochastic updating process with a fixed point equal to  $W$ , then with the right updating procedure we can

randomly explore the vicinity of this fixed point, continually generating new configurations distributed according to  $W$  [30]. So, any initial field-configuration can be iteratively massaged to a thermal configuration, which can then be further iterated upon to continue generating more configurations. Because of the iterative procedure, these configurations are highly correlated together – one must choose configurations separated by enough *Markov time* such that these autocorrelations are negligible.

The entire process is:

- (1) Propose a random set of complex numbers
- (2) Propose a new set, by randomly modifying the previous configuration.
- (3) Accept or reject the new set, according to probability  $P$ .
- (4) Repeat (2)-(3) many times
- (5) After repeating enough times, the chains “thermalize” and we can begin taking configurations as our sampling points for the integrand, provided they are far enough apart in Markov time to have small autocorrelations.

To ensure the existence of a fixed point (the thermalization) the updating scheme must fully cover the region, allowing any configuration to potentially be generated; it must be aperiodic, so that configurations don’t consistently return to the same point; and it must be reversible, so that given two configurations we have an identical probability of proposing the first from the second as *vice versa*. (The *proposal* probability must be the same, not the acceptance probability.)

The metropolis method [31] meets these requirements through random updates accepted with probability

$$P_{\text{accept}} = \min \left( 1, \frac{W_b}{W_a} \right), \quad (5.17)$$

which always takes changes that increase the weight, and sometimes accepts changes that lower the weight. Accepting changes that increases this weight allows us to find and remain near the fixed point, while the occasional changes that lower the weight allow us to explore the area surrounding the maximum. Generally if the acceptance rate is too high, the changes being made are too small and the integral is being explored too slowly. If the acceptance rate is too low, then time is being wasted proposing configurations that are not used.

Making *local* updates, or changing only a few variables at a time, falls into the category of small changes that take longer to cover the integration region; the advantage is that a small change is easy to make. These algorithms have been explored

in the quenched approximation, where the fermion determinant is neglected [32] [33]. Changing the entire field by small amounts explores the integration region faster, but even small changes made to the entire field often result in large changes to  $W$ , which can often be rejected.  $W$  contains a matrix determinant, which must be entirely recalculated even for local updates (contrastingly, the action need not be *entirely* recalculated) so there is absolutely no advantage to this first method. Thus, we need a procedure for calculating global updates that only alter the weight  $W$  by a small amount.

### 5.3.2 Hybrid Monte Carlo

Global modifications that alter the final weight  $W$  only slightly are hard to make. One method is to invent a fictitious Hamiltonian, with fictitious conjugate momenta  $\Pi$ , with which to evolve fields  $G$ , as in [34] [35]. So, we invent a Hamiltonian  $H$  that evolves our fields  $G$  and  $\Pi$  in fictitious time according to

$$\begin{aligned} H &= S_g[G] + \int d^4x \frac{1}{2} \Pi_\mu^\dagger \Pi_\mu \\ G(f + \delta f) &= G(f) + \delta f \{H, G\} \\ \Pi(f + \delta f) &= \Pi(f) + \delta f \{H, \Pi\}. \end{aligned} \tag{5.18}$$

(Ignore the fermions, for now. We will introduce them shortly.) Exact evolution means that  $H$  doesn't change, so any changes to  $S$  must be balanced by the small changes to  $\Pi^2$ . In practice our fictitious time-evolution is inexact, but this is entirely irrelevant as all that matters is that the changes to  $S$  are generally small enough to be accepted at a decent rate.

Now, incorporating fermions into the above is slightly tricky. We must rewrite this determinant as a term in the action in order to introduce the above Hamiltonian flow procedure. This is precisely where it came from originally – a term like  $\bar{\psi} M \psi$  between fermion fields leads to a  $\det M$ , while the identical term between bosons  $\phi M \phi$  leads to a  $\det M^{-1}$ . We can't use Grassmann variables to compute  $\bar{\psi} M \psi$  but we *can* use bosonic variables to compute  $\phi M^{-1} \phi$ .

Using identical up- and down-quarks means that there are two identical factors of  $\det M_\ell$  in the integrand. This guarantees positivity for Monte Carlo sampling, and we move this term into the action with  $\phi^\dagger (M M^\dagger)^{-1} \phi$ . Unfortunately, this is not as

easy for the single strange quark. There, the factor becomes  $\phi^\dagger(MM^\dagger)^{-\frac{1}{2}}\phi$  if  $\det M_s$  is positive; because of the comparatively larger mass of the strange compared to the light quarks this is generally true. Therefore, in the light-sector we apply one  $M$  to each pseudofermion, but for the strange-sector we must use  $(M^\dagger M)^{\frac{1}{4}}$ . The actual factor of  $(M^\dagger M)^{\frac{1}{4}}$  applied to each  $\phi$  is estimated via the rational approximation

$$(M^\dagger M)^{\frac{1}{4}} \approx \alpha_0 1 + \sum_i \frac{a_i}{M^\dagger M + b_i} \quad (5.19)$$

for particular set of coefficients  $\alpha, a, b$  [36].

To summarize, starting with a set of original fields  $(G_0, \Pi_0, \phi_0)$  we update in the following way:

- (1) Calculate a new  $\Pi, \chi$
- (2) Evaluate

$$\begin{aligned} \phi_\ell &= M_\ell[G]\chi_\ell \\ \phi_\ell^\dagger &= \chi_\ell^\dagger M_\ell[G]^\dagger \\ \phi_s &= (M_s[G]^\dagger M_s[G])^{\frac{1}{4}} \chi_s \\ \phi_s^\dagger &= \chi_s^\dagger (M_s[G] M_s[G]^\dagger)^{\frac{1}{4}} \end{aligned} \quad (5.20)$$

- (3) Discretely evolve

$$\begin{aligned} \dot{G} &= -\frac{\partial H}{\partial \Pi} \\ \dot{\Pi} &= \frac{\partial H}{\partial G} \end{aligned} \quad (5.21)$$

with a fictitious  $H$

$$H = S_g[G] + \sum_x \frac{1}{2} \Pi^2 + \chi_\ell^\dagger \chi_\ell + \chi_s^\dagger \chi_s \quad (5.22)$$

- (4) Accept the evolved  $G, \Pi$  and new  $\phi$  with probability

$$P = \min(1, e^{-(H-H_0)}) \quad (5.23)$$

- (5) Repeat

The rational approximation comes into play while evaluating both  $\phi_s$  and  $\frac{\partial H}{\partial G}$ . Additionally, the derivative term  $\frac{\partial H}{\partial G}$  can be computed because  $G$  are stout-smeared

analytically. This ensures that the map can be differentiated and discretized for fictitious time-evolution.

The product of all this is merely a set of configurations  $\{G\}$ , distributed according to  $W$ . Now, it is easy to see that operators or functionals of  $G$  are straightforward to calculate, by using the value on each configuration. However, we have clearly not generated any Grassmann or fermionic fields for similar use. In fact, we have seen instead that the fermionic fields have completely disappeared, leaving behind only a factor  $\det M$  used in the weight  $W$  of  $\{G\}$ .

# Chapter 6

## Correlator Analysis

In this chapter, we discuss correlator analysis and excited-state extraction *via* the single-pivot method. We briefly discuss pruning guidelines, as well as our calculation of overlap factors and the various fit forms used.

### 6.1 Excited States

We have been viewing energies as the decay rates of temporal correlators, as in

$$\begin{aligned}\langle 0|\hat{A}(t)\hat{B}^\dagger(0)|0\rangle = C_{AB}(t) &= \sum_n \langle 0|\hat{A}|n\rangle \langle n|\hat{B}^\dagger|0\rangle e^{-E_n t} \\ &= \sum_n Z_A^n Z_B^{n*} e^{-E_n t},\end{aligned}\tag{6.1}$$

so the gap between the ground state and the first excited state is given by:

$$\begin{aligned}E_1 &= \lim_{t \rightarrow \infty} -\frac{d}{dt} \ln \left( \langle 0|\hat{A}(t)\hat{B}^\dagger(0)|0\rangle - \langle 0|\hat{A}|0\rangle \langle 0|\hat{B}^\dagger|0\rangle \right) \\ &= \lim_{t \rightarrow \infty} -\frac{d}{dt} \ln \left( C_{AB}(t) - Z_A^0 Z_B^{0*} \right).\end{aligned}\tag{6.2}$$

(For every operator we consider these vacuum overlap factors  $Z_i^0$  are exactly zero, because our operators transform non-trivially under some symmetries.) We have also stated that a matrix of correlators will allow extraction of higher-lying excited states. It is not too different from a variational method: an incomplete set of unperturbed eigenstates  $\{\varphi_i\}$  is used to find approximate interacting eigenstates  $\psi = c_i \varphi_i$  basically by minimizing  $\langle \psi|H|\psi\rangle$ . Typically, higher-lying modes are found by minimizing the

expectation value *and* demanding orthogonality with the previous eigenstate. Remembering that the energy is like a decay rate for our correlators, this amounts to finding the linear combination of operators that decay most slowly. Diagonalizing the correlator automatically generates these linear combinations.

Specifically, the *principal correlator* method involves diagonalizing on each time slice to find eigenvalues  $\lambda_0 \geq \lambda_1 \geq \dots \geq \lambda_{N-1}$ :

$$\lim_{t \rightarrow \infty} \lambda_n(t) = e^{-E_n t} (1 + \mathcal{O}(e^{-\Delta_n t})) \quad (6.3)$$

where  $\Delta_n = \min_{k \neq n} |E_k - E_n|$  is the minimum difference between adjacent energies. This shows that as the correlator time separation  $t$  increases, each eigenvalue becomes a single decaying exponential, with decay rate  $E_n$ . We can visualize this decay rate by using the *effective mass*

$$m_{\text{eff}}(t) = -\frac{d}{dt} \ln C(t) \quad (6.4)$$

which is discretized to

$$m_{\text{eff}}(t) = -\frac{1}{\Delta t} (\ln C(t + \Delta t) - \ln C(t)). \quad (6.5)$$

For small times  $t$ , one can see that the correlator does *not* take the form of a single exponential, which only sets in for large times  $t$ . Therefore, whereas the correlator will always fall to zero exponentially, we expect to see effective masses that eventually plateau to a constant value,  $a_t E$  in dimensionless units. Once sub-leading contributions are negligible, we generally fit correlators with a single exponential and then display the fit value superimposed on an effective mass. It bears repeating that we do not fit the effective mass itself.

## 6.2 Single Rotation

The above discussion focused on the so-called principal-correlator method, where every time slice was diagonalized. In fact, this is not strictly necessary, and similar results can be found by only diagonalizing at *one* time,  $t_d$ , and rotating all other timeslices by the same matrix. This works provided that the off-diagonal elements stay statistically consistent with zero.

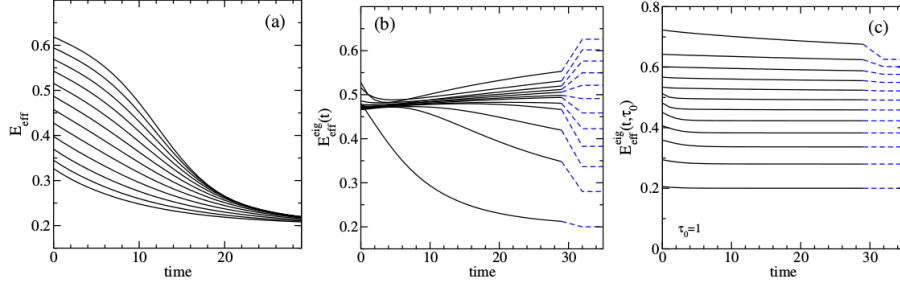


Figure 6.1: Toy correlator example. On the left, before diagonalization, all effective masses tend to lowest level. Center, after diagonalization, effective masses tend slowly to excited states. Right, after diagonalization and pre-/post-multiplying by  $C^{-1/2}(t_0)$ , effective masses tend quickly to excited states.

So, given a Hermitian correlation matrix  $C_{ij}(t)$  we rescale,

$$C_{ij}(t) \rightarrow \frac{C_{ij}(t)}{\sqrt{C_{ii}(t)C_{jj}(t)}} = R_{ij}(t) \quad (6.6)$$

which just rescales the various rows and columns to make the process more computationally convenient. The first significant step is to choose a “metric time”  $t_0$  and demand the correlator is equal to unity at this time,

$$R(t) \rightarrow R^{-1/2}(t_0)R(t)R^{-1/2}(t_0) = G(t). \quad (6.7)$$

This serves to change the error factor from  $\Delta_n = \min_{k \neq n} |E_k - E_n|$  to  $\Delta_n = |E_N - E_n|$ , where  $E_N$  is the first *omitted* energy. (That is, the lowest energy that we do not attempt to extract.) This dramatically accelerates the rate these eigenvalues reach their asymptotic values, as demonstrated in Figure 6.1 using a toy model.

This figure shows, first, that before diagonalizing the correlator matrix every entry approaches a common decay rate  $E$ . After diagonalizing, the decay rate of these diagonal entries approach a variety of values, albeit slowly. And, pre/post multiplying by  $C^{-1/2}(t_0)$  hastens the approach to each energy.

After these preliminary steps are done, we choose a time  $t_d$  at which to diagonalize  $G(t)$ :

$$\tilde{C}(t) = U^\dagger G(t)U \quad (6.8)$$

where  $U$  diagonalizes  $G(t_d)$ .

## 6.3 Pruning

Generally, we make a large number of operators for each channel. In practice, some of these produce rather noisy or poorly estimated correlators. It becomes important to remove some of these bad operators, where the definition of bad is rather subjective. For example, by looking directly at the correlators of an operator with itself (the diagonal entries of the undiagonalized correlator) we can sometimes distinguish a good operator from a bad operator, with examples shown in Figures 6.2 and 6.3.

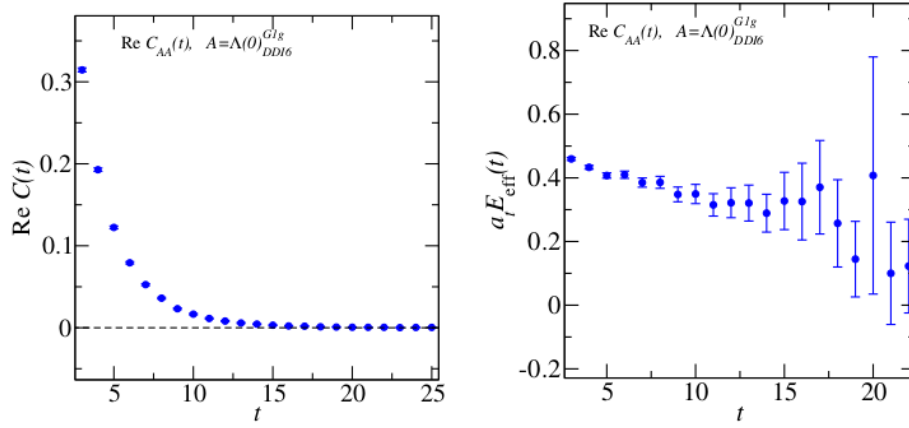


Figure 6.2: Clean signal on correlator and effective mass indicates a good operator. A visible plateau on the effective mass is also desirable, but not required.

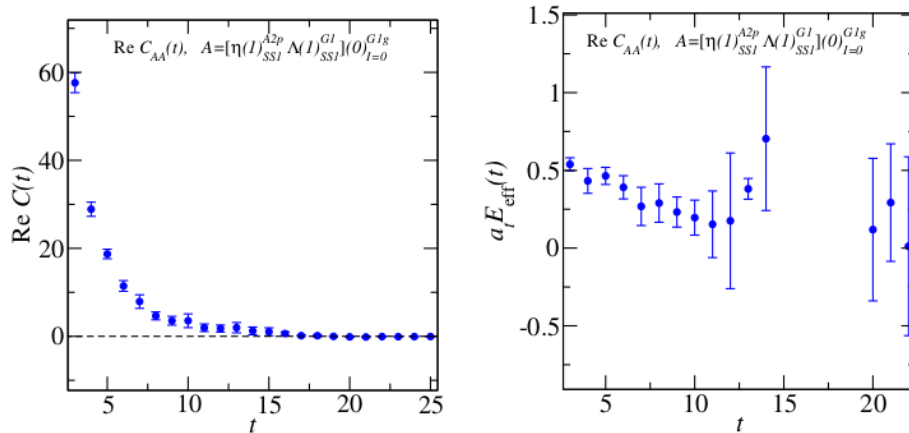


Figure 6.3: Noisy signal on correlator and effective mass indicates a bad operator. Large vertical spreads generally hide poor plateau behavior.

This is often insufficient. One must also take care to remove any linearly dependent operators, even if they are well-behaved. If the correlation matrix contains such operators, they lead to zero modes of the diagonalized correlator, which are obviously non-physical. Any eigenvalues that are negative or statistically consistent with zero can be removed completely, with their associated eigenvector not making it into the matrix  $U$ . That is, we move from an  $N \times N$  correlator to an  $M \times M$  correlator after dropping  $N - M$  eigenvectors. Throughout our results, we used a threshold,

$$\lambda_{\min} \equiv \vartheta \lambda_{\max}, \quad (6.9)$$

dropping any eigenvalues below  $\lambda_{\min}$ . We found that  $\vartheta = 0.01$  was sufficient.

## 6.4 Overlaps

In addition to the energy value  $E$ , our results also include the (less important) overlap factors

$$Z_i^n = \langle n | \hat{O}_i | \Omega \rangle \quad (6.10)$$

which are recovered from the amplitudes of our exponentials,  $Ae^{-Et}$ . After fitting every level  $n$  we find that the correlator takes on an approximate form of

$$C_{nn}(t) = A_n e^{-E_n t}, \quad (6.11)$$

and we can use the set  $\{A_n\}$  to find

$$Z_i^n = G^{1/2}(t_0)_{ij} U_{jn} A_n^{1/2} \quad (\text{no sum over } n), \quad (6.12)$$

the overlap between the  $i^{th}$  operator and the  $n^{th}$  energy level. Really, these are only defined to within a phase, so the physical quantity is  $|Z|^2$ . Furthermore, we recall that the overall norm of the correlator was arbitrary, so the numerical value of each  $Z$  is irrelevant. Instead we care only about the relative magnitudes of  $Z_i^n$  and  $Z_i^m$ , two overlap factors for the same operator on different energy levels. For an  $N \times N$  correlator, we must fit every level to recover any overlap factor.

We have already seen that it is necessary to sometimes prune our operators, reducing the size of the correlator from  $N \times N$  to  $M \times M$ . If this is the case, the

extracted overlap factors (post-pruning/post-projection) can be remade into overlap factors for our *original* operators with

$$Z_i^{(O)n} = P_{ij} Z_j^{(P)n}, \quad (6.13)$$

which relates  $j = 1, \dots, M$  pruned operators to  $i = 1, \dots, N$  original operators. The  $N \times M$  matrix  $P$  just projects out the lowest eigenvectors which cause  $\lambda_{\min} < \vartheta \lambda_{\max}$  in Equation 6.9.

## 6.5 Temporal Wrap-Around

Recall that our correlators are designed to produce vacuum expectation values only in the zero-temperature, or infinite time, limits. Furthermore, they are constructed to satisfy time-reversal symmetry and periodicity. A simple fit form like  $Ae^{-Et}$  is incapable of seeing backward-propagating modes, which are most relevant for lighter particles or lower energies  $E$ . In the meson channels, fit forms like

$$Ae^{-Et} + Ae^{-E(T-t)} \quad (6.14)$$

can be used. Clearly the backward-propagating piece disappears as  $T \rightarrow \infty$  for finite  $t$ , and is also less relevant for larger  $E$ . For this reason, baryonic channels do not generally include any backwards piece in the fit form. This is a relief as, for baryons, the backward-propagating state is the parity-partner (unlike the mesons, where it is the same particle) so a fit accounting for backward-propagating modes must deal with *two* symmetry channels at once, rather than one.

## 6.6 Fitting

### 6.6.1 Fit Forms

The form  $Ae^{-Et}$  has another defect: it is known to be incorrect for any  $t \neq \infty$ . Of course, it is approximately correct for large  $t$ , when the excited-state contamination (subleading exponentials) is negligible. We can mock up these subleading terms by

using a two-exponential fit,

$$C(t) \sim Ae^{-Et} (1 + be^{-\Delta t}) \quad (6.15)$$

or even a geometric series

$$C(t) \sim Ae^{-Et} (1 + be^{-\Delta t} + b^2e^{-2\Delta t} + \dots) = \frac{Ae^{-Et}}{1 - be^{-\Delta t}} \quad (6.16)$$

where in both cases  $\Delta > 0$  represents the difference between our fit energy  $E$  and an unwanted excited state. These extraneous parameters are not used for anything other than finding an appropriate fit, as defined by the correlator or effective mass. The energies and overlap factors are calculated as before, using exclusively  $E$  and  $A$ .

One typically sees that these multi-exponential fit forms are more sensitive to noise, especially the initially precise correlator data. The main advantage of these fits is the independence of the starting point, relative to single exponentials which must be chosen only after subleading contributions are negligible. In the baryonic sector, we have less-diluted quarks (see chapter 5 for noise dilution) and higher statistical error. Often only the lowest one or two energy states are clean enough to use multi-exponential fits, whereas mesonic sectors are typically more amenable to this technique.

### 6.6.2 Statistical Error

All of the error analysis is done in the same way, with resampling. That is, take the set of configurations  $\{G\}$  and make many new sets  $\{G\}_i$ ; we inquire about some property of  $\{G\}$  by considering instead the collection  $\{\{G\}_i\}$ . In this work we focus on bootstrap- and jackknife-resampling.

In jackknife-resampling, one takes a set of  $N_c$  configurations  $\{G\}$  and declares  $N_c$  new *sets* of configurations, each set having one configuration removed from the original set. So, the set of configurations  $\{U\}_{i=1}^{N_c}$  consists of every configuration in  $\{G\}$  *except* the first. Because we are only removing one configuration, values on the entire ensemble ought to be close to values on each resampling.

The bootstrap-resampling procedure is a lot like jackknifing, except that we choose new configurations randomly. Specifically, if we have  $N_c$  configurations we make  $N_b$  bootstrap-resamplings by choosing  $N_c$  samples from our original configurations, ran-

domly and with replacement, for each desired resampling. The phrase *with replacement* is key, and allows many configurations to be used multiple times, or not at all. Here, we are dramatically changing our sets of configurations so one expects that values should jump around quite a bit from ensemble to resampling, or resampling to resampling.

A fit value like  $A$  or  $E$  can be found easily on the entire ensemble, but to find the errors in these fit values we use the resamplings. All analysis is done by fitting on *each resampling*; the mean of these values is representative of the actual, or ensemble, average and the spread of these fit values gives the error for the whole ensemble. For jackknife-resampling, which we use for the spectrum results, the relevant formula is

$$\sigma^2(f) = \frac{N_c - 1}{N_c} \sum_i^{N_c} (\langle f \rangle_i - \langle f \rangle)^2, \quad (6.17)$$

where  $\langle \cdot \rangle$  denotes the average on the full ensemble, and  $\langle \cdot \rangle_i$  denotes that same average with the  $i^{\text{th}}$  configuration *removed*. In the case of bootstrap-resampling, which we use for the pion-scattering results, the relevant formula is

$$\sigma^2(f) = \frac{1}{N_b} \sum_i^{N_b} (\langle f \rangle_i - \langle f \rangle_B)^2 \quad (6.18)$$

where  $\langle \cdot \rangle_B$  denotes the average of all the bootstrap-resamplings, and  $\langle \cdot \rangle_i$  denotes only the average on the  $i^{\text{th}}$  resampling.

### 6.6.3 Correlated Fits

Remembering that our configurations were generated through a Markov chain, we know that there is some residual correlations between our configurations. These are referred to as autocorrelations, and are intentionally made negligible. However, we must still perform correlated fits because each datapoint – each time-slice – came from the same Monte Carlo ensemble. That is, we cannot minimize a traditional, uncorrelated  $\chi^2$ ,

$$\chi^2 = \sum_t \frac{(C(t) - f(\boldsymbol{\alpha}, t))^2}{\sigma_t^2} \quad (6.19)$$

for some model function  $f$ , but rather a correlated  $\chi^2$

$$\chi^2 = \sum_{t,t'} (C(t) - f(\boldsymbol{\alpha}, t)) \text{Cov}^{-1}(t, t') (C(t') - f(\boldsymbol{\alpha}, t')), \quad (6.20)$$

where the covariance  $\text{Cov}(t, t')$  for our correlator fits is estimated using

$$\text{Cov}(t, t') = \frac{1}{N_t - 1} \langle C(t) - \langle C(t) \rangle \rangle \langle C(t') - \langle C(t') \rangle \rangle, \quad (6.21)$$

for  $N_t$  time-slices used in the fit.

# Chapter 7

## Phase Shifts and the Luscher Method

In this chapter we discuss a generalization of Luscher’s method to extract scattering information, as well as the  $K$ -matrix method to include multiple-channel scattering and partial waves. We detail the introduction of the box matrix  $B$ , which mixes angular momenta in the cubic volume. We also mention our fit strategy for the Luscher quantization condition.

### 7.1 Luscher Quantization Condition

It has been known for some time that scattering phase shifts can be extracted from the volume-dependence of finite-volume quantum systems [9] [10]. This is an important work-around to a no-go theorem of Maiani and Testa [37] that explains what information Wick-rotation does and doesn’t spoil. Time-independent information, like stationary-state energies, is preserved by the change but processes like scattering are blocked, as the absence of phase structure in the imaginary-time formalism eliminates phase shifts. Ultimately, the no-go theorem refers to infinite-volume Euclidean and Minkowski correlators; the finite-volume spectra do determine some properties of the infinite-volume Minkowski correlators. It is interesting to note that Luscher’s solution actually predates the no-go theorem. Originally the method relied on lattice results from multiple volumes and only applied to simple scattering of identical scalars, but it has been generalized to allow moving frames and more complex scattering situations [38] [39] [40].

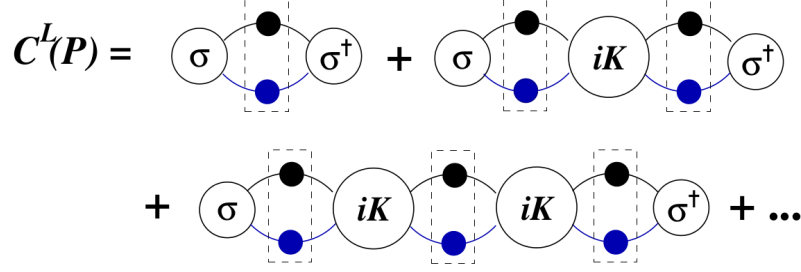


Figure 7.1: The series of ladder diagrams that builds up  $C^L$ , in 7.1. The Bethe-Salpeter kernels  $iK$  are connected by two fully dressed propagators, indicated by  $B^L$ . The dashed rectangle indicates finite volume momentum sum/integrals. The different colors of the single-particle propagators indicate different types of particles, but choosing the same color allows for identical particles. The two-body interpolating operator that couples to all open two-body channels is  $\sigma$ . Initial states are on the right, final states on the left.

The full field-theoretic derivation, which accounts for multiple-channel scattering, was provided as recently as 2005 [41] [42]. The end result of this process is a simple condition that relates the infinite volume  $S$ -matrix and a peculiar function  $F$  calculated purely from our lattice energies  $E$ . We outline the derivation of this quantization condition.

The idea is to follow the locations of poles in a general two-particle correlator, which we write as

$$\begin{aligned}
C^L(\mathbf{P}) &= \int d^4\mathbf{x} e^{i(Et - \mathbf{P} \cdot \mathbf{x})} \langle 0 | \sigma(\mathbf{x}) \sigma^\dagger(0) | 0 \rangle \\
&= \frac{1}{L^3} \sum_{\mathbf{q}} \int_{-\infty}^{\infty} \frac{dq^0}{2\pi} \sigma_a(\mathbf{q}) B_a^L(\mathbf{q}) \sigma_a^\dagger(\mathbf{q}) \\
&\quad + \frac{1}{L^6} \sum_{\mathbf{q}, \mathbf{q}'} \int_{-\infty}^{\infty} \frac{dq^0}{2\pi} \frac{dq'^0}{2\pi} \sigma_a(\mathbf{q}) B_a^L(\mathbf{q}) iK_{ab}(\mathbf{q}, \mathbf{q}') B_b^L(\mathbf{q}') \sigma_b^\dagger(\mathbf{q}') + \dots,
\end{aligned} \tag{7.1}$$

and express diagrammatically in Figure 7.1. The subscripts refer to the decay channel,  $K$  is the Bethe-Salpeter kernel which is expressed in Figure 7.2, and  $B^L$  is the fully dressed two-particle finite-volume propagator. The key concept here is that we separate  $B^L$  into its infinite-volume counterpart plus a small correction, as shown in Figure 7.3. We can avoid expressing  $iK$  in its finite-volume form, using instead the

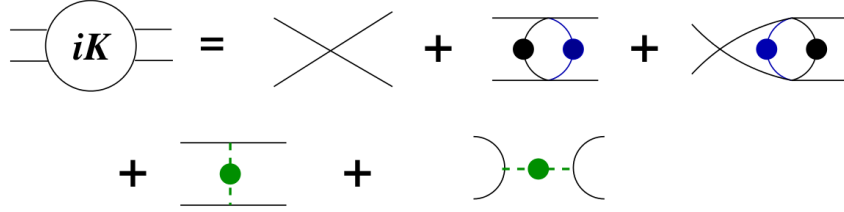


Figure 7.2: Allowed diagrams in  $iK$ . This consists of all scattering diagrams that cannot be considered part of the two fully dressed propagators. Possible meson exchanges are indicated with black, blue, and green dots.

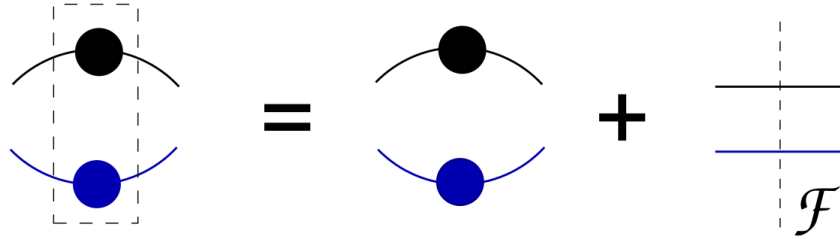


Figure 7.3: The finite-volume momentum sum/integral for two single-particle dressed propagators is indicated with the dashed box on the left. We relate this to the equivalent expression in infinite volume, plus a correction term  $\mathcal{F}$ . This expression defines  $\mathcal{F}$ .

infinite-volume version, because in the kinematic region we consider the corrections are exponentially suppressed. However, a particular pole in  $B^L$  does become relevant because it is near our kinematic region, and causes non-exponentially small corrections.

The correlator  $C^L$  has poles at each stationary-state energy. As  $L$  increases, we expect some of these poles to move off the real axis (unstable resonances), some to merge into a continuous branch cut (two free particles; scattering states) and others to stay roughly in the same place (stable particles). For real energies, the equivalent object in infinite volume,  $C^\infty$ , only has these latter two types of poles. Therefore, the difference  $C_{\text{sub}} = C^L - C^\infty$  should have the same “resonance poles” as  $C^L$ , since they can not be removed by  $C^\infty$ . We will show that these are the *only* poles  $C_{\text{sub}}$  contains.

After performing some algebra on the diagrams in  $C^L$  and  $C^\infty$ , we can show  $C_{\text{sub}}$  reduces to a compact form illustrated in Figure 7.4. Algebraically, this is equivalent to

$$C_{\text{sub}} = A\mathcal{F}(1 - i\mathcal{M}\mathcal{F})^{-1}A' = A(\mathcal{F}^{-1} - i\mathcal{M})^{-1}A'. \quad (7.2)$$

The factors  $A$  and  $A'$  may produce branch cuts, but cannot contain the real poles in our kinematic region.  $\mathcal{F}$  contains the same two-particle “scattering” poles as  $C^L$ , but appears in both the numerator and denominator so ultimately  $C_{\text{sub}}$  is regular in these regions. Therefore, every pole in  $C_{\text{sub}}$  comes from the finite-volume states that become resonances in infinite volume; these poles occur when  $(\mathcal{F}^{-1} - i\mathcal{M})$  is not invertible, or

$$\det(1 - i\mathcal{F}\mathcal{M}) = 0. \quad (7.3)$$

This is the *quantization condition*. We can rescale the rows and columns of  $\mathcal{F}$  and  $\mathcal{M}$  by a kinematic factor  $\frac{16\pi^2 E_{\text{cm}}}{\mathbf{q}_{\text{cm}}}$  to find a slightly modified form more convenient for our purposes,

$$\det[1 + F(S - 1)] = 0, \quad (7.4)$$

$$\begin{aligned}
\textcircled{A} &= \textcircled{\sigma} + \textcircled{\sigma} \textcircled{iK} + \textcircled{\sigma} \textcircled{iK} \textcircled{iK} + \dots \\
\textcircled{A'} &= \textcircled{\sigma^\dagger} + \textcircled{iK} \textcircled{\sigma^\dagger} + \textcircled{iK} \textcircled{iK} \textcircled{\sigma^\dagger} + \dots \\
\textcircled{iM} &= \textcircled{iK} + \textcircled{iK} \textcircled{iK} + \textcircled{iK} \textcircled{iK} \textcircled{iK} + \dots \\
C_{\text{sub}}(P) &= \textcircled{A} \textcircled{A'} + \textcircled{A} \textcircled{iM} \textcircled{A'} + \textcircled{A} \textcircled{iM} \textcircled{iM} \textcircled{A'} + \dots
\end{aligned}$$

The diagrams use the following conventions:  $\sigma$  and  $\sigma^\dagger$  are circles with a horizontal line on the left;  $iK$  and  $iM$  are circles with horizontal lines on both the left and right. Blue arcs connect the bottom of one circle to the bottom of another, while black arcs connect the top. In the  $C_{\text{sub}}(P)$  terms, vertical dashed lines labeled  $\mathcal{F}$  separate the components  $A$ ,  $A'$ , and  $iM$ .

Figure 7.4: Expressing  $C_{\text{sub}} = C^L - C^\infty$ , in terms of  $A, A', iM$  and  $\mathcal{F}$ .

which was rescaled in order to explicitly display  $S$ , the usual infinite-volume scattering matrix. The function  $F$  is calculated purely from our lattice energies  $E$ :

$$\begin{aligned}
E_{\text{cm}} &= \sqrt{E^2 - \frac{(2\pi)^2}{L^2} \mathbf{d}^2} \\
\gamma &= \frac{E}{E_{\text{cm}}} \\
\mathbf{q}_{\text{cm}}^2 &= \frac{1}{4} E_{\text{cm}}^2 - \frac{1}{2} (m_1^2 + m_2^2) + \frac{1}{4} \frac{(m_1^2 - m_2^2)^2}{E_{\text{cm}}^2} \\
u^2 &= \frac{L^2}{(2\pi)^2} \mathbf{q}_{\text{cm}}^2 \\
\mathbf{s} &= \left( 1 + \frac{m_1^2 - m_2^2}{E_{\text{cm}}^2} \right) \mathbf{d} \\
&\Rightarrow F(\mathbf{s}, \gamma, u^2)
\end{aligned} \tag{7.5}$$

Specifically, imagining some set of lattice levels which are supposed to be near a resonance, the function  $F$  is highly sensitive to the differences between these energies and free energy of the nearest two-particle state.

Equation 7.3 is always true and sometimes useful. We say sometimes useful because this is only one equation, and unless there is only one scattering-channel it does not completely determine the phase shifts. So, we must generally parametrize not just  $S$  in terms of phase shifts and inelasticities, but rather these objects in terms of particular functions  $\delta(s)$  and  $\eta(s)$ . Historically, lattice results for the  $\pi\pi$  scattering phase shift around the  $\rho$  resonance ignore partial waves other than  $L = 1$  and solve the equation for  $\delta$  [43].

Ultimately however it is not the phase shift itself in which we are interested. One is instead interested in where the phase rapidly progresses through  $\pi/2$ , as indicative of a resonance. Specifically, we are looking for the resonance-mass and decay width, which must be extracted from the phase shift *via* a parametrization, typically a Breit-Wigner, anyway. We can parametrize the  $S$  matrix in terms of these quantities directly.

## 7.2 K-matrix Method

Rather than parametrizing  $S$ , one might be more interested in  $iT = S - 1$  appearing in equation 7.4 and representing more directly the particle interactions. This  $T$  must satisfy the optical theorem, inherited from the unitarity of  $S$ , and an easy way to ensure this is to focus on

$$K^{-1} = T^{-1} + i \quad (7.6)$$

which the optical theorem guarantees is real and symmetric. This is the  $K$  matrix, and its parametrization is quite flexible. For example, we can consider multiple resonances in the same channel by including multiple poles and we can deal with multiple-channel scattering by extending the matrix.

Explicitly, for the  $K$ -matrix of a single channel with one resonance we might write

$$K = \frac{g^2}{E^2 - M^2} \quad (7.7)$$

where  $M$  is the mass of the resonance, and its decay width  $\Gamma$  is written in terms of  $g, M$  and the phase space determined by the decay products  $m_1$  and  $m_2$ . We are permitted to add polynomials to mock up a background varying slowly in the region near the pole, and sometimes it is important to add some energy-dependent prefactors, like

$$K = \left(\frac{p}{m}\right)^3 \frac{1}{E} \frac{g^2}{E^2 - M^2} \quad (7.8)$$

in the case of  $L = 1$  scattering.

Rewriting the quantization condition in terms of the  $K$  matrix gives

$$\det(1 + K [i - 2iF]) = 0 \quad (7.9)$$

and the quantity in brackets is redefined as the box matrix  $B$ .

## 7.3 The Box Matrix

This box matrix becomes the core of the analysis, because it represents the totality of the geometric effects of a finite cubic volume on an otherwise infinite volume spectrum. It is completely independent of any dynamical QCD effect, caring only about the values of the masses, momenta and lengths of the system.

In the usual language of  $JLS$  scattering states, the  $B$  matrix is written as

$$\langle J'm_J L'S'a' | B | Jm_J L S a \rangle = -i\delta_{aa'}\delta_{SS'}W_{L'm_{L'} L m_L} C_{L'm_{L'} S m_S}^{J'm_{J'}} C_{L m_L S m_S}^{*Jm_J} \quad (7.10)$$

with

$$\begin{aligned} W_{L'm_{L'} L m_L} &= i \sum_{\ell, m} \frac{\mathcal{Z}_{\ell m}(\mathbf{s}, \gamma, u^2)}{\pi^{3/2} \gamma u^{\ell+1}} \sqrt{\frac{(2L'+1)(2\ell+1)}{2L+1}} C_{L'0\ell 0}^{L0} C_{L'm_{L'} \ell m}^{*L m_L} \\ \mathcal{Z}_{\ell m}(\mathbf{s}, \gamma, u^2) &= \sum_{\mathbf{n}} \frac{Y_m^\ell(\mathbf{z})}{\mathbf{z}^\ell (\mathbf{z}^2 - u^2)} e^{-\Lambda(\mathbf{z}^2 - u^2)} + \delta_{\ell 0} \frac{\gamma \pi}{\sqrt{\Lambda}} F_0(\Lambda u^2) \\ &\quad + \frac{i^\ell \gamma}{\Lambda^{\ell+1/2}} \int_0^1 dt \left(\frac{\pi}{t}\right)^{\ell+3/2} e^{\Lambda t u^2} \sum_{\mathbf{n} \neq 0} e^{i\pi \mathbf{n} \cdot \mathbf{s}} \frac{Y_m^\ell(\mathbf{w})}{\mathbf{w}^\ell} e^{-\frac{\pi^2 \mathbf{w}^2}{t\Lambda}} \\ \mathbf{z} &= \mathbf{n} - \frac{1}{\gamma} \left( \frac{1}{2} + (\gamma - 1) \frac{\mathbf{n} \cdot \mathbf{s}}{\mathbf{s}^2} \right) \mathbf{s} \\ \mathbf{w} &= \mathbf{n} - (1 - \gamma) \frac{\mathbf{s} \cdot \mathbf{n}}{\mathbf{s}^2} \mathbf{s} \\ F_0(x) &= -1 + \frac{1}{2} \int_0^1 dt \frac{e^{tx} - 1}{t^{\frac{3}{2}}} \end{aligned} \quad (7.11)$$

with the generalized zeta functions appearing as a result of extensive manipulation of infinite sums and contour integrals. We choose the arbitrary constant  $\Lambda \approx 1$  and perform the integrals with Gauss-Legendre quadrature.

The determinant condition is difficult to use since the relevant matrix is infinitely large. However, one can show that it block-diagonalizes into irreps of the octahedral and little groups. In each block, one can assume an  $L_{\max}$  to truncate its size to a finite number of basis states. The structure of  $B$  in this basis is important, because it demonstrates that this matrix preserves internal properties like spin and flavor but mixes up orbital and total angular momentum, due to the cubic volume. This is to be compared with the  $K$  matrix, which preserves total angular momentum but will mix spins and flavors due to interactions:

$$\langle \Lambda' \lambda' n' J' L' S' a' | B | \Lambda \lambda n J L S a \rangle = \delta_{\Lambda' \Lambda} \delta_{\lambda' \lambda} \delta_{S' S} \delta_{a' a} B_{J' L' n', J L n}^{(\mathbf{P} \Lambda_B S a)}(E). \quad (7.12)$$

These coefficients are tabulated in [44]. We briefly note the distinction between the label  $\Lambda$  on the irrep of the octahedral or little group in which the resonance

appears and the label  $\Lambda_B$  on the box matrix itself. Because  $B$  only cares about the cubic geometry without regard to details of the scattering channel, it is insensitive to intrinsic parity. In the case that  $\eta_a = 1$  we find  $\Lambda = \Lambda_B$ , whereas if  $\eta_a = -1$   $\Lambda_B$  is the parity-partner of  $\Lambda$ . These are

<b>d</b>	LG	$\Lambda_B$ relationship to $\Lambda$
(0,0,0)	$O_h^D$	$g \leftrightarrow u$
(0,0, $n$ )	$C_{4v}$	$A_1 \leftrightarrow A_2$ ; $B_1 \leftrightarrow B_2$ ; $E, G_1, G_2$ stay same
(0, $n$ , $n$ )	$C_{2v}$	$A_1 \leftrightarrow A_2$ ; $B_1 \leftrightarrow B_2$ ; $G$ stays same
( $n$ , $n$ , $n$ )	$C_{3v}$	$A_1 \leftrightarrow A_2$ ; $F_1 \leftrightarrow F_2$ ; $E, G$ stay same

## 7.4 Fitting

With our parametrizations in hand, we want naively to minimize the determinant  $1 - KB$ , with both  $K$  and  $B$  calculated in our octahedral basis as

$$\det(1 - KB). \quad (7.13)$$

It turns out we find more convenient behavior by considering  $K^{-1} - B$  and instead minimizing the function  $\Omega$  :

$$\Omega(\mu, K^{-1} - B) = \frac{\det(K^{-1} - B)}{\det[\mu^2 + (K^{-1} - B)(K^{-1} - B)^\dagger]^{\frac{1}{2}}} \quad (7.14)$$

which has a zero at the same places as our original condition, but does not become large from the product of the many nonzero eigenvalues. Further details on the fit procedure are found in [44].

The ultimate output of this strategy is a value for the resonance mass and decay width which are dependent on the  $K$  matrix parametrization. We have skipped finding the phase shift itself entirely, though this can be reconstructed from our  $K$  matrix if desired.

# Chapter 8

## Results

In this chapter, we first present the spectroscopy results for several at-rest baryonic channels, followed by the  $L = 1, 3$  and  $5$  phase shifts for  $\pi\pi$  scattering. For spectroscopy, we focus on the  $\Lambda$  resonances, looking at several symmetry channels in the  $I = 0, S = -1$  sector. Specifically, we have extracted spectra from correlators in the  $G_{1g}, G_{1u}, H_g$  and  $H_u$  symmetry channels. Previous work in this sector has been done on much smaller lattices with heavier pion masses. After the spectra, we present a mesonic phase shift analysis which extracts the mass and decay width of an infinite volume  $\rho$  resonance *without* neglecting partial-wave mixing. For the first time in lattice QCD, we incorporate all partial waves up to  $L = 5$ .

### 8.1 Computational Details

There are four main stages of the calculation. First, the gauge configurations must be generated using the pseudo-Hamiltonian flow described previously. This process is extremely expensive, using 200 million core hours total, distributed among Jaguar at Oak Ridge National Laboratory (sponsored by the Department of Energy) and Kraken at University of Tennessee (sponsored by the National Science Foundation).

Secondly, we calculate all the quark propagators. This was done with software written in C++ using the USQCD QDP++ library [45]. The entire process took about 100 million core hours, mainly on the Kraken machine. In this stage, the main computational expenses come from inverting the large Dirac matrix; the quark propagators must be combined into the hadronic source- and sink-functions, which are then combined for all the relevant operators in a given channel. The bottleneck

here is mostly due to file I/O. The Stampede supercomputer at University of Texas at Austin and Comet in San Diego were used to perform these final contractions. This was also sponsored by the NSF, and took approximately 50 million core hours.

Lastly, after all the source- and sink-functions have been combined into correlator elements for a given channel, we store them on disk here at CMU. That is, we have a complex number for each source-sink pair, for each timeslice, for each configuration stored locally. These are extracted and analyzed with our XML-driven C++ code which we call SigMonD, for signal extraction of Monte Carlo data. This code performs the actual matrix-diagonalizations, rotations, and fits, for the energy spectra. The phase shift calculation itself is done by another piece of XML-driven C++ code, Chimera, authored by John Bulava.

## 8.2 $G_{1g}$ Spectrum on $32^3 \times 256$

The isosinglet strange  $G_{1g}$  channel (at rest) is parity-positive and consists of spins  $\frac{1}{2}$ ,  $\frac{7}{2}$  and  $\frac{9}{2}$ , and contains the physical  $\Lambda$  as well as a few resonances mostly of spin  $\frac{1}{2}$ . These include  $\Lambda(1600)$ ,  $\Lambda(1810)$  and  $\Lambda(2350)$  (the last of these is spin  $\frac{9}{2}$ ).

The two-particle-content consists of particular meson-baryon pairings. Remembering that our meson and baryon operators are labeled for flavor structure only, we see that the the following two-particle operators excite states in this channel:

$\Lambda\eta$	Isospin	$0 + 0$	Strangeness	$-1 + 0$	Spin	$\frac{1}{2} + 0$
$N\bar{K}$	Isospin	$\frac{1}{2} + \frac{1}{2}$	Strangeness	$0 - 1$	Spin	$\frac{1}{2} + 0$
$\Sigma\pi$	Isospin	$1 + 1$	Strangeness	$-1 + 0$	Spin	$\frac{1}{2} + 0$
$\Xi K$	Isospin	$\frac{1}{2} + \frac{1}{2}$	Strangeness	$-2 + 1$	Spin	$\frac{1}{2} + 0$

(Ordinarily, we would want both  $\eta$  and  $\phi$ , but  $\Lambda\phi$ -operators were too high in energy.) In each case, the above baryons are positive parity and the mesons are negative parity. So, all of our simple meson-baryon operators must have some nonzero back-to-back momentum for the total parity to be positive. If any meson-baryon operator in this channel has zero constituent momenta, at least one of the operators is expected to couple to a resonance, or at least not the state corresponding most precisely to its flavor name. For example, an  $\eta\Lambda$  both at rest could not correspond to the physical  $\Lambda$ , but rather a resonance like the  $\Lambda(1405)$  which has negative parity.

A list of some low-lying “expected” levels is given in Table 8.1 . Energies of physical particles corresponding to a given operator are added to find a non-interacting

meson	baryon	operators
$\bar{K}[1]$	$N[1]$	$A_2 \text{ SS2} - G_1 \text{ SS0}$
$\pi[1]$	$\Sigma[1]$	$A_2^- \text{ SS1} - G_1 \text{ SS0}$ $A_2^- \text{ SS1} - G_1 \text{ SS2}$
$\bar{K}[2]$	$N[2]$	$A_2 \text{ SS0} - G \text{ SS0}$ $A_2 \text{ SS1} - G \text{ SS0}$
$\pi[2]$	$\Sigma[2]$	$A_2^- \text{ SS0} - G \text{ SS1}$
$\eta[1]$	$\Lambda[1]$	$A_2^+ \text{ SS1} - G_1 \text{ SS1}$
$\pi[1]$	$\Sigma(1385)[1]$	$A_2^- \text{ SS1} - G_1 \text{ SS0}$ $A_2^- \text{ SS1} - G_1 \text{ SS2}$
$\bar{K}[3]$	$N[3]$	$A_2 \text{ SS0} - G \text{ SS0}$
$\eta[2]$	$\Lambda[2]$	$A_2^+ \text{ SS0} - G \text{ SS0}$
$\pi[3]$	$\Sigma[3]$	none
$K^*(892)[1]$	$N[1]$	$E \text{ SS2} - G_1 \text{ SS0}$
$K[1]$	$\Xi[1]$	$A_2 \text{ SS1} - G_1 \text{ SS0}$ $A_2 \text{ SS1} - G_1 \text{ SS2}$
$\eta[0]$	$\Lambda(1405)[0]$	none
$\bar{K}[4]$	$N[4]$	$A_2 \text{ SS1} - G_1 \text{ SS0}$
$\pi[2]$	$\Sigma(1385)[2]$	$A_2^- \text{ SS0} - G \text{ SS1}$
$\pi[0]$	$\Sigma(1750)[0]$	$A_{1u}^- \text{ SS0} - G_{1u} \text{ SS0}$
$\omega(782)[1]$	$\Lambda[1]$	$E^- \text{ SS1} - G_1 \text{ SS1}$

Table 8.1: Some expected two-hadron levels in the  $G_{1g}$  channel. We list operators that might excite, or couple strongly to, each level. In each case, square-brackets  $[n]$  indicates constituent momentum-squared, as  $\mathbf{p}^2 = n (2\pi/L)^2$ .

two-particle energy; this gives us a rough idea of which operators must be made and used. We make many more operators than appear on this list, but ultimately these are pruned down to some smaller set which has a better signal. For example, operators containing an  $\eta$  particle were often found to be noisy, and largely irrelevant, coupling only to the higher energy states. Such operators are pruned away.

In addition to the above two-particle operators, we also have the single-baryon operators. A large set of 13 operators was pruned down to just six, by removing noisy operators as well as operators found to be linearly dependent with others in the set. The final single hadron operators are:

$\Lambda$	$G_{1g}$	SS3
$\Lambda$	$G_{1g}$	TDT5
$\Lambda$	$G_{1g}$	TDT8
$\Lambda$	$G_{1g}$	DDI22
$\Lambda$	$G_{1g}$	TDT28
$\Lambda$	$G_{1g}$	TDT38

(The letters indicate displacement type, shown in Table 4.2 and the number is just an extra index.) We first “optimize” these single-hadron operators by diagonalizing the correlator only in the single-hadron subspace. We refer to the resulting eigenvectors, linear combinations of our original operators, as “optimized” because they overlap more strongly with particular stationary states. We determine overlap factors for these optimized single-hadron operators, labeled as 0 through 5, rather than the original operators directly. This is to be contrasted with the two-hadron operators, which were not pre-rotated in this way. Ultimately, this procedure cannot change the observed spectrum, instead modifying only the single-hadron overlap factors.

We calculated correlator elements for everything in the above lists, from timeslice 3 to 25, or  $t = 3a_t$  to  $t = 25a_t$ . Diagonalizing at later times would be ideal, except that noise gets progressively worse at later times. Diagonalizing at earlier times is not desirable, because it increases excited-state contamination and the correlator is less likely to stay diagonal. For this channel, a diagonalization time of 8 and a metric time of 5 were found to be sufficient for off-diagonal elements to be consistent with zero; the relatively noisy baryons, compared to mesons, prevent a later diagonalization time. Operators were pruned such that the correlator matrix itself was not ill-conditioned, having no negative or zero eigenvalues.

While we prefer multi-exponential fits, like the two-exponential or geometric series, many of the levels in this channel were found to be too noisy for these fits to be reliably used. As a result, we have preferred single-exponential fits for most levels, with a geometric series only used for the lowest level. These fits are displayed in Table 8.2. For reference, we also give the effective mass plots for each level in Figure 8.1, though these are illustrative only and the effective mass points are not used in any fit.

Level	Time Range	$a_t E$	$\chi^2/\text{dof}$	content
0	(3, 22)	.2203(64)	0.83	$\Lambda$
1	(10, 22)	.329(30)	1.89	$K[1] - \Xi[1]$
2	(8, 22)	.367(33)	1.32	$\bar{K}[1] - N[1]$
3	(6, 22)	.381(10)	1.91	$\pi[1] - \Sigma[1]$
4	(5, 22)	.382(13)	1.45	
5	(8, 22)	.383(25)	1.07	$qqq$
6	(8, 22)	.383(50)	1.11	$\eta[2] - \Lambda[2]$
7	(8, 20)	.388(66)	0.47	$\eta[1] - \Lambda[1]$
8	(7, 22)	.400(23)	0.84	
9	(5, 22)	.401(11)	2.40	$qqq$
10	(5, 22)	.4033(82)	1.84	$K[2] - N[2]$
11	(8, 22)	.413(20)	1.29	$K[3] - N[3]$
12	(6, 22)	.414(11)	1.57	
13	(7, 22)	.417(28)	0.77	$K[4] - N[4]$
14	(8, 22)	.420(19)	0.17	
15	(6, 22)	.438(15)	1.32	$K^*(892)[1] - N[1]$
16	(6, 22)	.444(14)	2.14	
17	(7, 22)	.476(45)	1.16	$qqq$
18	(6, 22)	.497(32)	1.43	$\omega(782)[1] - \Lambda[1]$
19	(5, 22)	.509(35)	2.10	
20	(6, 22)	.524(52)	1.44	$K[1] - N[1]$
21	(5, 22)	.728(79)	0.77	

Table 8.2: Results of non-periodic exponential fits to the 22 diagonal entries of a diagonalized correlator in the  $G_{1g}$  channel. Last column indicates an operator which overlaps maximally with a given level. All fits are single exponentials, with the exception of level 0, a geometric series. The subleading amplitude and energy for such a fit is neither used nor reported.

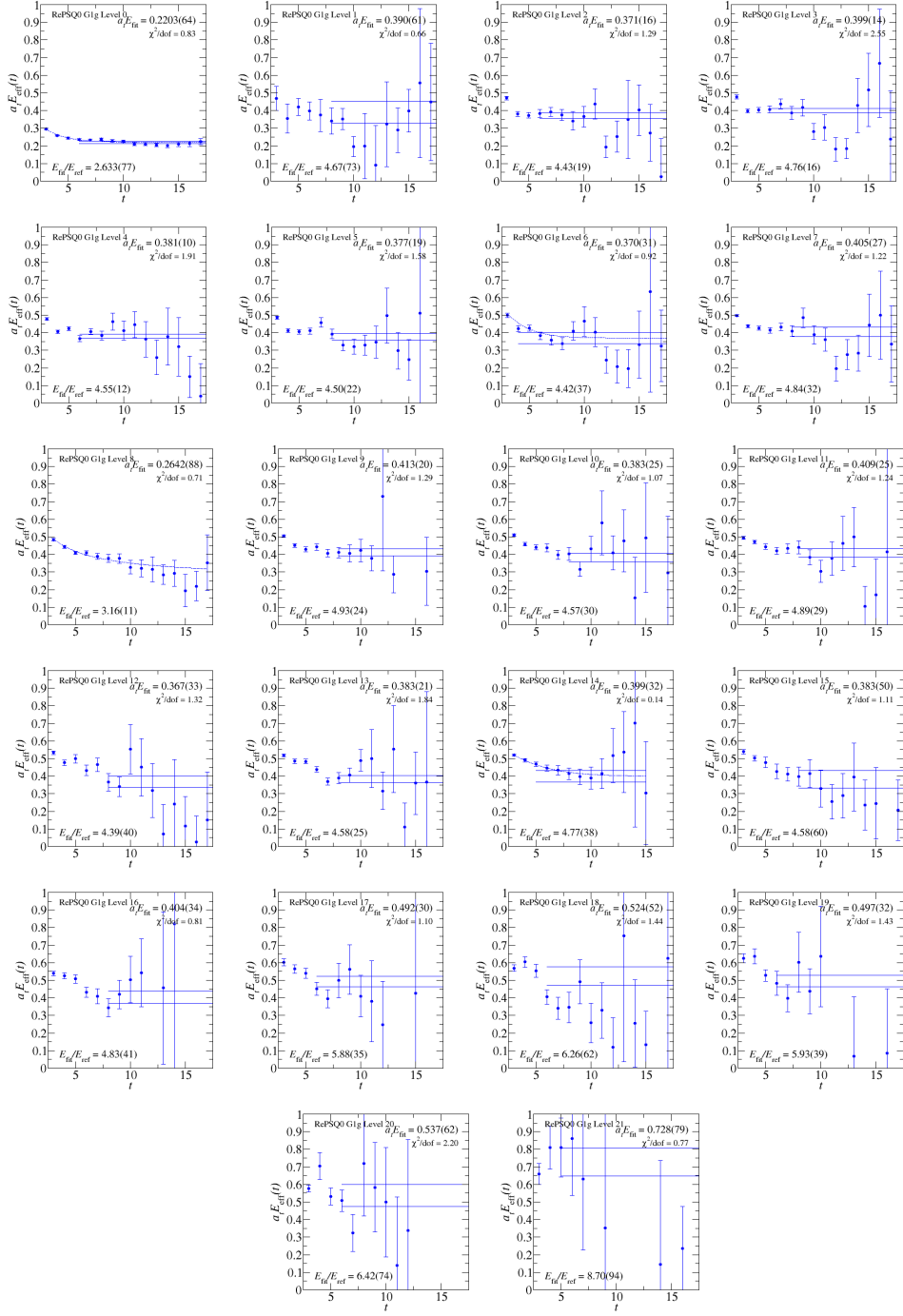


Figure 8.1: Effective energies of diagonal elements of a diagonalized correlator in the  $G_{1g}$  channel. Horizontal lines display the upper and lower bounds for the final fit value, calculated *via* jackknifing, and dotted lines, when present, display the approach from any subleading exponentials. We use a time separation of  $\Delta t = 3$  in the discretized derivative.

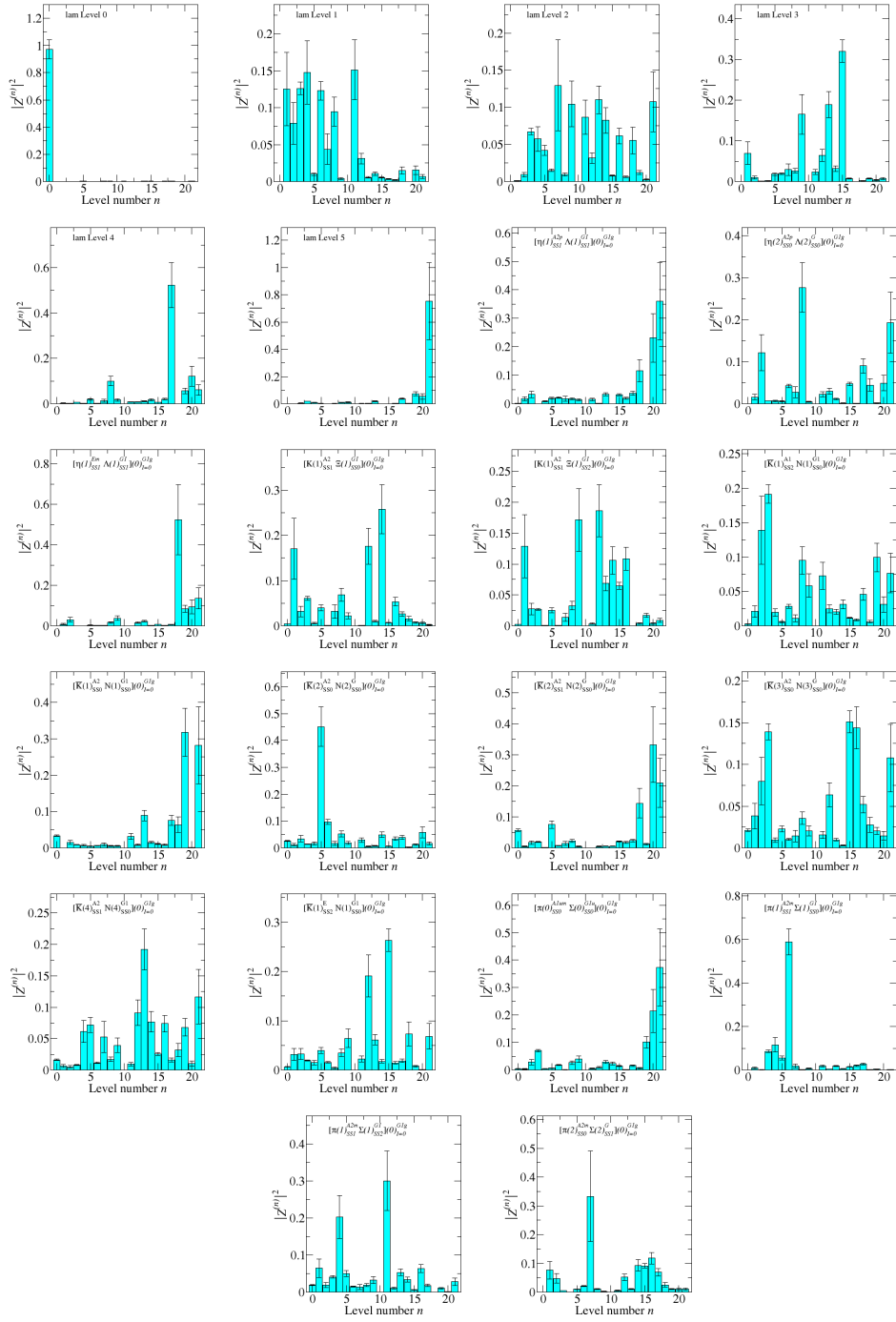


Figure 8.2: Overlap factors for each operator onto the extracted energy-levels in the  $G_{1g}$  channel. Each single-hadron operator has been optimized by pre-diagonalizing in the single-hadron subspace. The maximum bar for each operator is used to identify the corresponding level. Bars within 75% of the maximum, for single hadrons, denote significant mixing.

After fitting every level and finding the overlap factors, we can attempt an identification of the content of these states. Figure 8.2 contains the overlap factors for each operator, demonstrating to which state(s) a given operator predominately couples. In addition to maximal peaks, we are also interested in the mixing – many single-hadron operators couple relatively strongly to multiple states, which is indicative of the behavior of a resonance. That is, we expect resonances to exhibit mixing between the dominate  $qqq$  content and potential decay products.

A summary of the spectrum is shown in Figure 8.3; in this figure, we color each level according to each operator that overlaps maximally with that level. So, some levels can have multiple colors, indicating maximal overlap on more than one operator, or no colors at all (gray) to indicate that no operator overlaps maximally with that energy level. Because we are more interested in the single-hadron operators, the black hatches indicate strong but subleading ( $> 75\%$  of the maximum for that operator) overlap with single-hadron operators. The most important energies, colored in solid black, are those that overlap maximally with the single-hadron levels.

We select these  $qqq$ -dominated states to compare with experimental spectra. For an  $N \times N$  correlator matrix, the energies near level  $N$  are less reliably determined; because the highest few states are rarely reproduced well, we ignore these levels in the identification process. In the case of  $G_{1g}$ , we ignore the two highest single-hadron-dominated states.

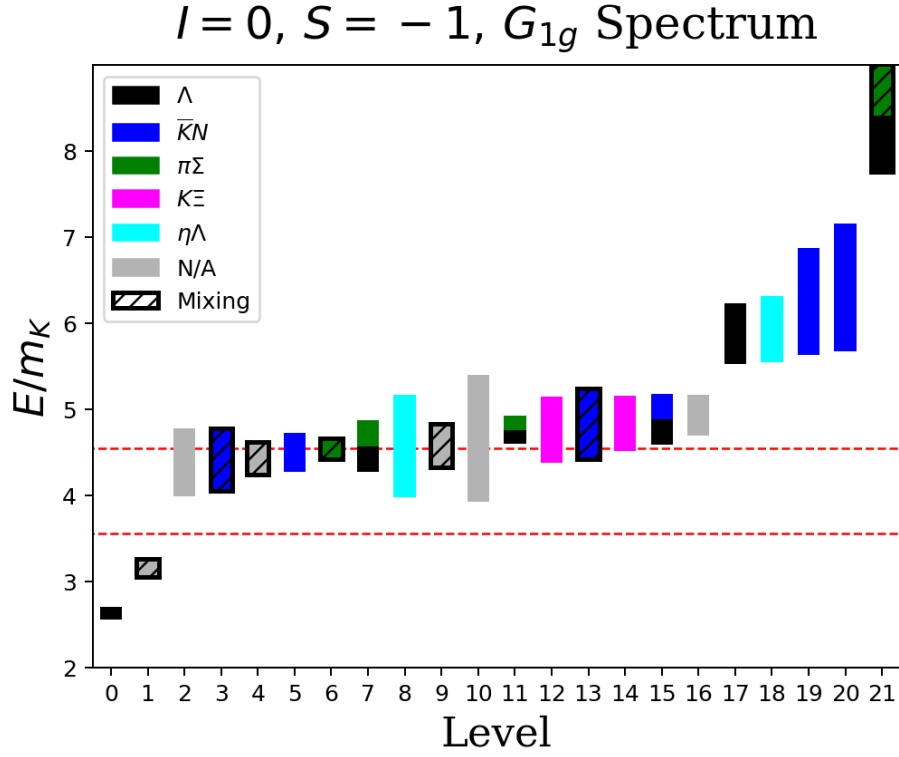


Figure 8.3: Full spectrum for isosinglet strange  $G_{1g}$ . Levels colored by maximal overlaps, with large but non-maximal overlaps on single-hadron operators indicating significant mixing. Three ( $\bar{K}[0]N[0]\pi[0]$ ) and four ( $\bar{K}[1]N[1]\pi[0]\pi[0]$ ) particle thresholds are displayed.

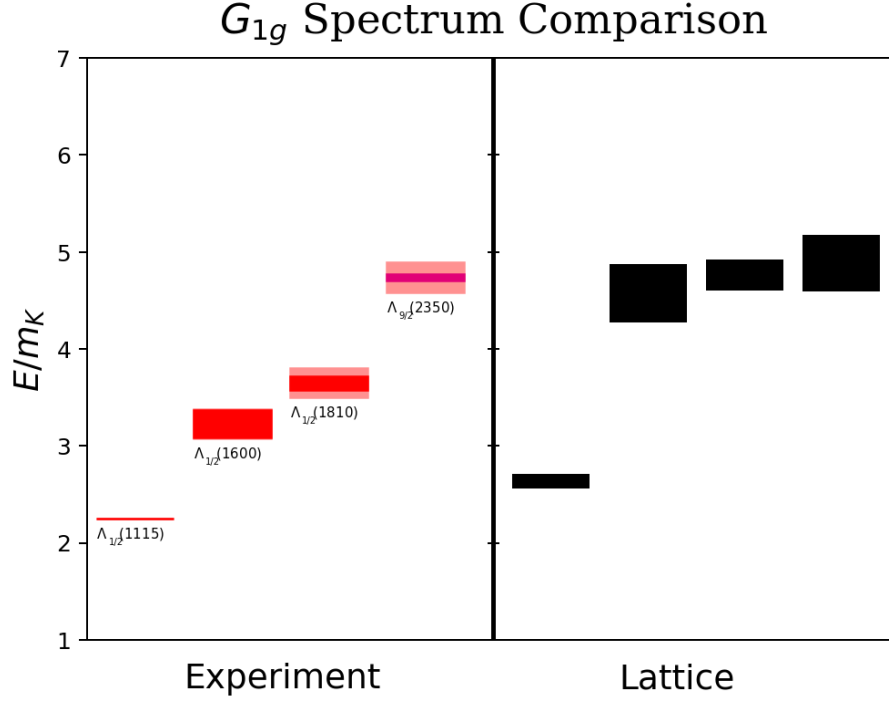


Figure 8.4: Experimentally observed resonances compared with our finite-volume single-hadron-dominated states. These energies are plotted in units of the kaon mass. On the left, dark bands indicate experimental uncertainty, with lighter bands indicated decay widths.

The  $G_{1g}$  spectrum of single-hadron-dominated states given in Figure 8.4 does not compare terribly well with the experimental spectrum, when expressed as ratios of the kaon mass. This is not surprising, given that we have an unphysically heavy pion and one strange quark in the sector. That is, one expects particles with less strange and more light content to be strongly affected by the pion mass, while particles with more strange and less light content ought to be less sensitive.

By comparing with the nucleon (which is made unphysically heavy) as a reference instead of the kaon (which is set to its physical mass) we can observe better agreement, shown in Figure 8.5.

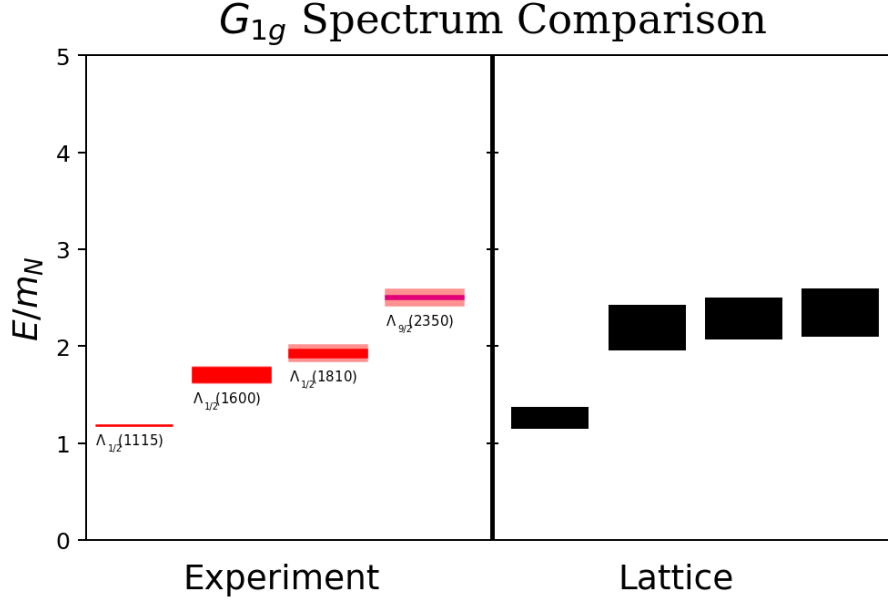


Figure 8.5: Experimentally observed resonances compared with our finite-volume single-hadron-dominated states. These energies are plotted in units of the nucleon mass. On the left, dark bands indicate experimental uncertainty, lighter bands indicate decay widths.

The overall structure compares well to past results on  $\Lambda$  baryons [46], shown in Figure 8.6. We find an isolated low-energy state corresponding to the physical  $\Lambda$ , as well as a group of three closely-spaced states at roughly twice that energy.

### 8.3 $G_{1u}$ Spectrum on $32^3 \times 256$

The isosinglet strange  $G_{1u}$  channel (at rest) is parity-minus and consists of spins  $\frac{1}{2}$  and  $\frac{7}{2}$ , and contains a few  $\Lambda$  resonances mostly of spin  $\frac{1}{2}$ . These include  $\Lambda(1405)$ ,  $\Lambda(1670)$ ,  $\Lambda(1800)$  and  $\Lambda(2100)$  (the last of these is spin  $\frac{7}{2}$ ).

The two-particle content is the same as in the  $G_{1g}$  channel, but with the opposite parity considerations. Because of this, two-particle meson-baryon states with both particles at rest show up here. A list of some low-lying “expected” levels is given in Table 8.3.

In addition to the above two-particle operators, we also have the single-baryon operators. A large set of 11 operators was pruned down to seven, by removing noisy operators as well as operators found to be linearly dependent with others in the set.

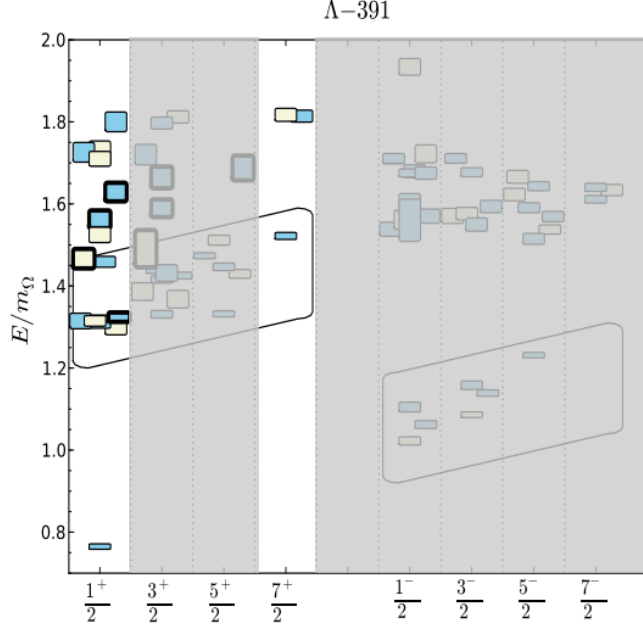


Figure 8.6: Observed baryonic states on a  $16^3$  lattice with a heavy 391 MeV pion [46]. The colors indicate  $SU(3)$ -flavor irrep, which we have not identified. Levels are labeled by  $J^P$ .

The final single hadron operators are:

$\Lambda$	$G_{1u}$	SS0
$\Lambda$	$G_{1u}$	SS1
$\Lambda$	$G_{1u}$	DDI10
$\Lambda$	$G_{1u}$	DDI16
$\Lambda$	$G_{1u}$	SD21
$\Lambda$	$G_{1u}$	TDT16
$\Lambda$	$G_{1u}$	TDT20

As in the  $G_{1g}$  channel, these operators are pre-rotated, to find “optimized” single hadron operators, labeled as 0 through 7, to be used in the calculation of overlap factors.

For this channel, a diagonalization time of 8 and a metric time of 5 were found to be sufficient for off-diagonal elements to be consistent with zero. As with  $G_{1g}$ , operators were pruned such that the correlator matrix itself was not ill-conditioned, having no negative or zero eigenvalues.

We have preferred single-exponential fits for most levels, with a geometric series

meson	baryon	operators
$\pi[0]$	$\Sigma[0]$	$A_{1u}^- \text{SS0} - G_{1g} \text{SS1}$
$\bar{K}[0]$	$N[0]$	$A_{1u} \text{SS0} - G_{1g} \text{SS0}$
$\bar{K}[1]$	$N[1]$	$A_2 \text{SS1} - G_1 \text{SS0}$
$\pi[1]$	$\Sigma[1]$	$A_2^- \text{SS1} - G_1 \text{SS2}$
$\eta[0]$	$\Lambda[0]$	$A_{1u}^+ \text{SS0} - G_{1g} \text{SS0}$
$K[2]$	$N[2]$	$A_2 \text{SS0} - G \text{SS0}$
$\pi[2]$	$\Sigma[2]$	$A_2^- \text{SS0} - G \text{SS1}$
$\eta[1]$	$\Lambda[1]$	$A_2^+ \text{SS1} - G_1 \text{SS1}$
$\bar{K}[0]$	$\Xi[0]$	$A_{1u} \text{SS0} - G_{1g} \text{SS0}$
$\pi[1]$	$\Sigma(1385)[1]$	$A_2^- \text{SS1} - G_1 \text{SS2}$
$K^*[0]$	$N[0]$	$T_{1u} \text{SS1} - G_{1g} \text{SS0}$
$\bar{K}[3]$	$N[3]$	$A_2 \text{SS0} - G_g \text{SS0}$
$\omega(782)[0]$	$\Lambda[0]$	$T_{1u}^- \text{SS0} - G_{1g} \text{SS0}$

Table 8.3: Some expected two-hadron levels in the  $G_{1u}$  channel. We list operators that might excite, or couple strongly to, each level.

only used for four low-lying levels. These fits are displayed in Table 8.4. For reference, we also give the effective mass plots for each level in Figure 8.7, though these are illustrative only and the effective mass points are not used in any fit.

Level	Time Range	$a_t E$	$\chi^2/\text{dof}$	content
0	(3, 22)	.298(12)	1.03	$\Lambda$
1	(3, 22)	.312(24)	1.24	$\bar{K}[0] - N[0]$
2	(10, 22)	.312(41)	0.97	
3	(3, 22)	.324(16)	0.80	$qqq$
4	(3, 22)	.329(13)	0.83	$qqq$
5	(8, 22)	.340(25)	0.65	
6	(8, 22)	.358(17)	1.02	$\bar{K}[0] - \Xi[0]$
7	(8, 22)	.364(15)	0.95	$\pi[1] - \Sigma[1]$
8	(8, 22)	.368(24)	0.74	$\bar{K}[1] - N[1]$
9	(8, 22)	.393(32)	1.66	
10	(8, 22)	.398(25)	0.72	$\pi[2] - \Sigma[2]$
11	(5, 22)	.3995(88)	1.66	$\bar{K}[2] - N[2]$
12	(8, 22)	.415(40)	1.73	$K^*[0] - N[0]$
13	(8, 22)	.453(66)	0.77	$qqq$
14	(6, 22)	.459(22)	1.19	$\omega(782)[0] - \Lambda[0]$
15	(6, 22)	.472(55)	0.56	$qqq$
16	(5, 12)	.529(51)	1.19	$\eta[0] - \Lambda[0]$
17	(3, 12)	.614(23)	2.36	$\eta[1] - \Lambda[1]$
18	(3, 12)	.735(44)	1.21	$qqq$

Table 8.4: Results of non-periodic exponential fits to the 19 diagonal entries of a diagonalized correlator in the  $G_{1u}$  channel. Last column indicates an operator which overlaps maximally with a given level. All fits are single exponentials, with the exception of levels 0, 1, 3 and 4, geometric series. The subleading amplitude and energy for such a fit is neither used nor reported.

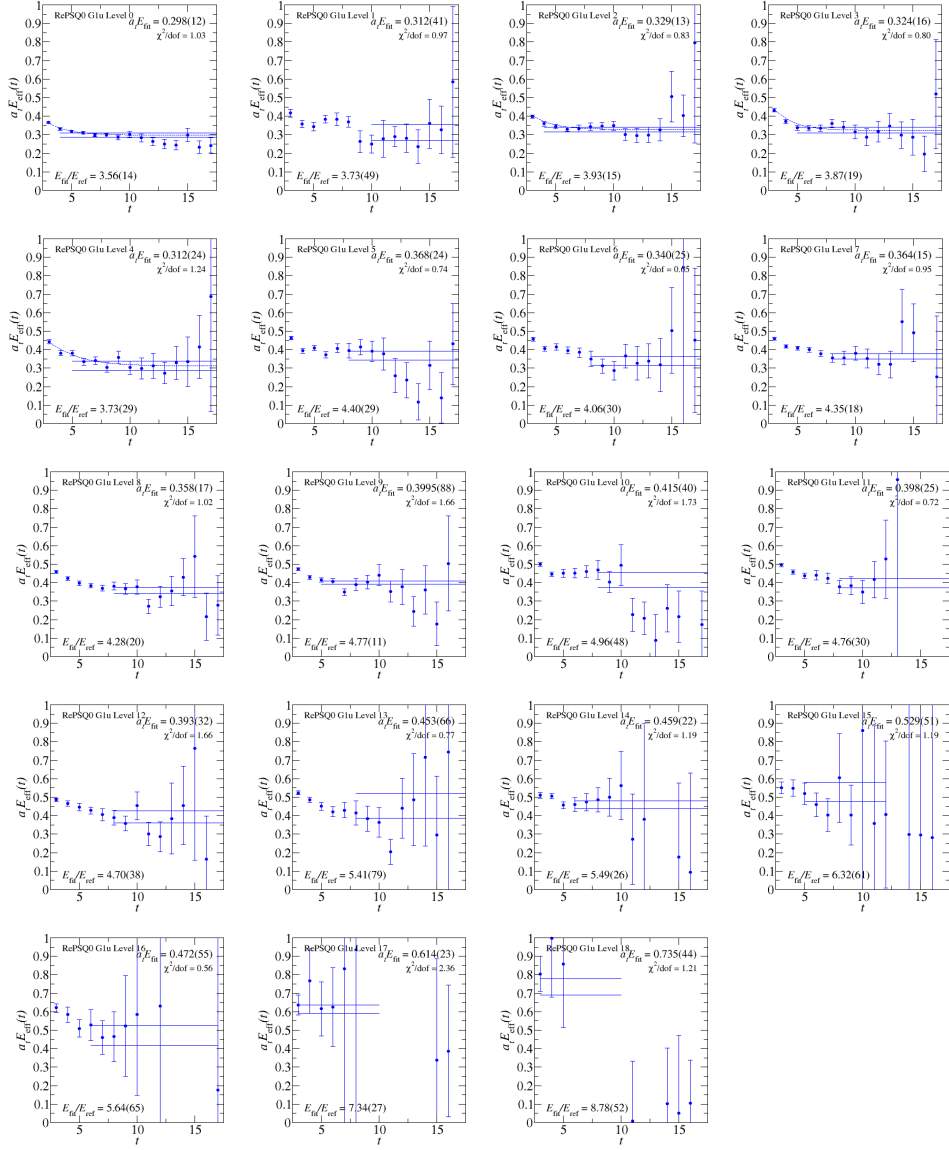


Figure 8.7: Effective energies of diagonal elements of a diagonalized correlator in the  $G_{1u}$  channel. Horizontal lines display the upper and lower bounds for the final fit value, and dotted lines, when present, display the approach from any subleading exponentials. We use a time separation of  $\Delta t = 3$  in the discretized derivative.

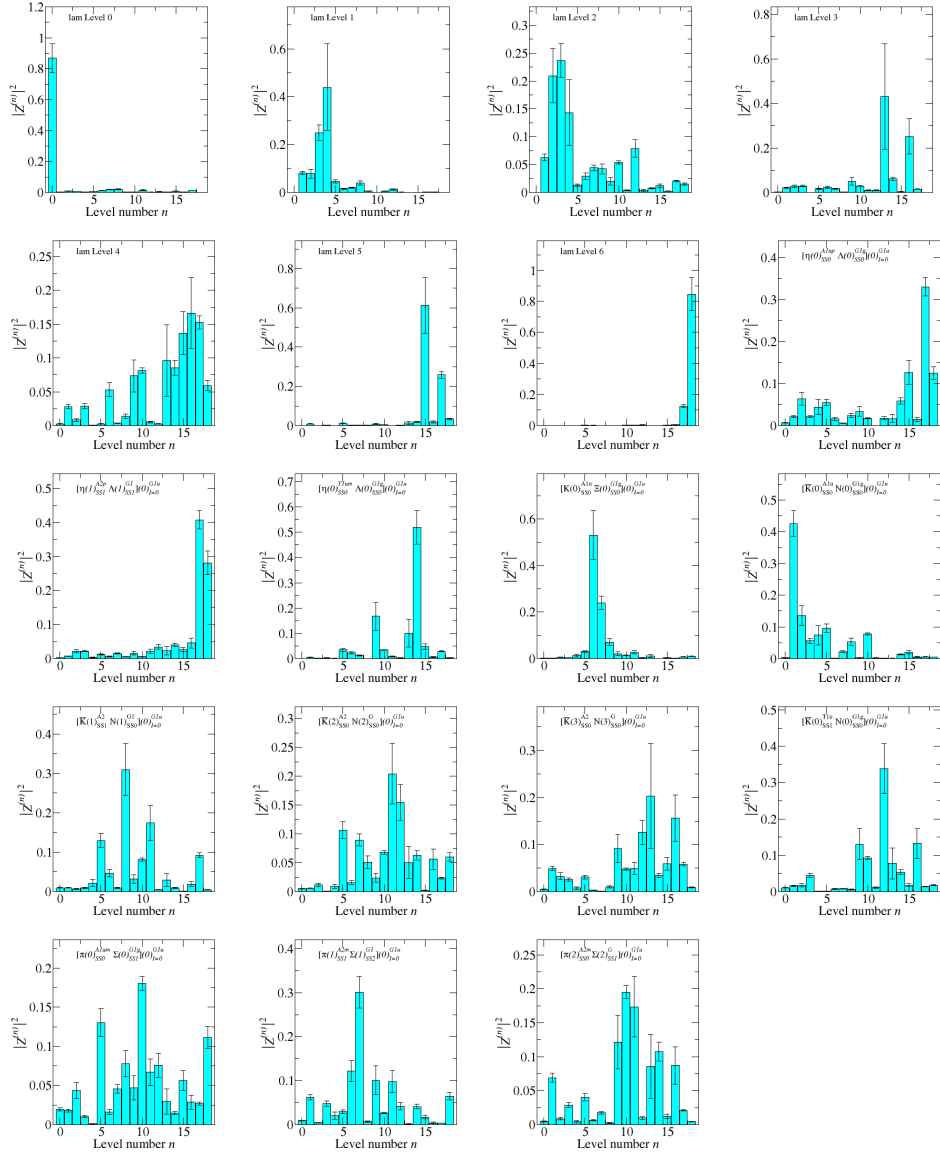


Figure 8.8: Overlap factors for each operator onto the extracted energy levels in the  $G_{1u}$  channel. Each single-hadron operator has been optimized by pre-diagonalizing in the single-hadron subspace. The maximum bar for each operator is used to identify the corresponding level. Bars within 75% of the maximum, for single hadrons, denote significant mixing.

As in  $G_{1g}$ , after fitting every level and finding the overlap factors, we can attempt an identification of the content of these states. Figure 8.8 contains the overlap factors for each operator, demonstrating to which state(s) a given operator predominately couples.

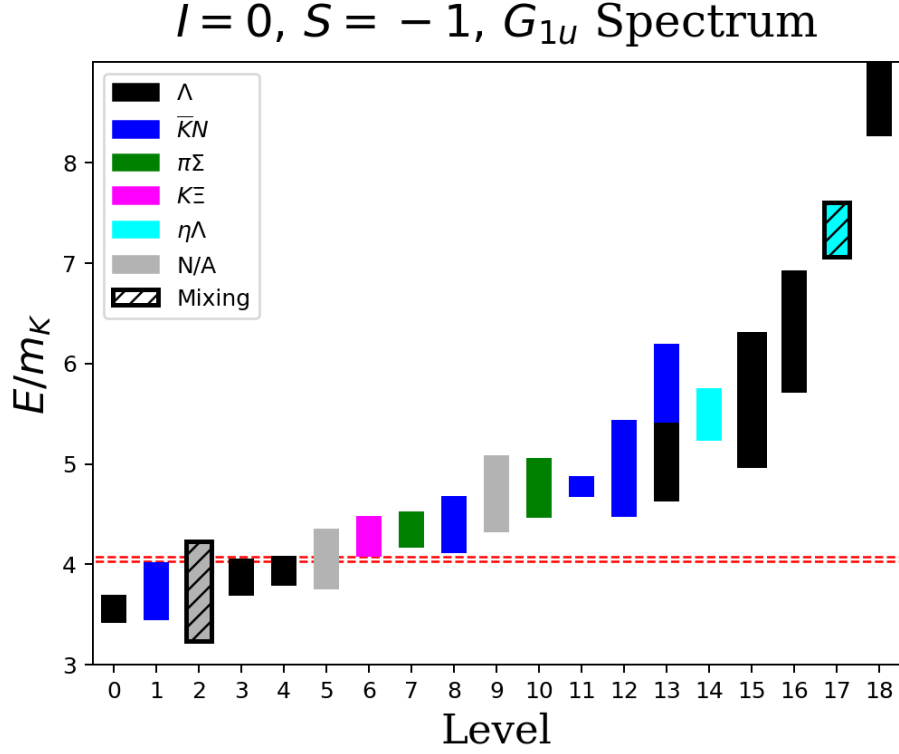


Figure 8.9: Full spectrum for isosinglet strange  $G_{1u}$ . Levels colored by maximal overlaps, with large but non-maximal overlaps on single-hadron operators indicating significant mixing. Three ( $\bar{K}[1]N[1]\pi[0]$ ) and four ( $\bar{K}[0]N[0]\pi[0]\pi[0]$ ) particle thresholds are displayed.

A summary of the spectrum is shown in Figure 8.9, colored in the same way as the  $G_{1g}$  spectrum. We again select  $qqq$ -dominated states to compare with experimental spectra. Because the highest few states are rarely reproduced well, we ignore these levels in the identification process. In the case of  $G_{1u}$ , we ignore the two highest single-hadron-dominated states.

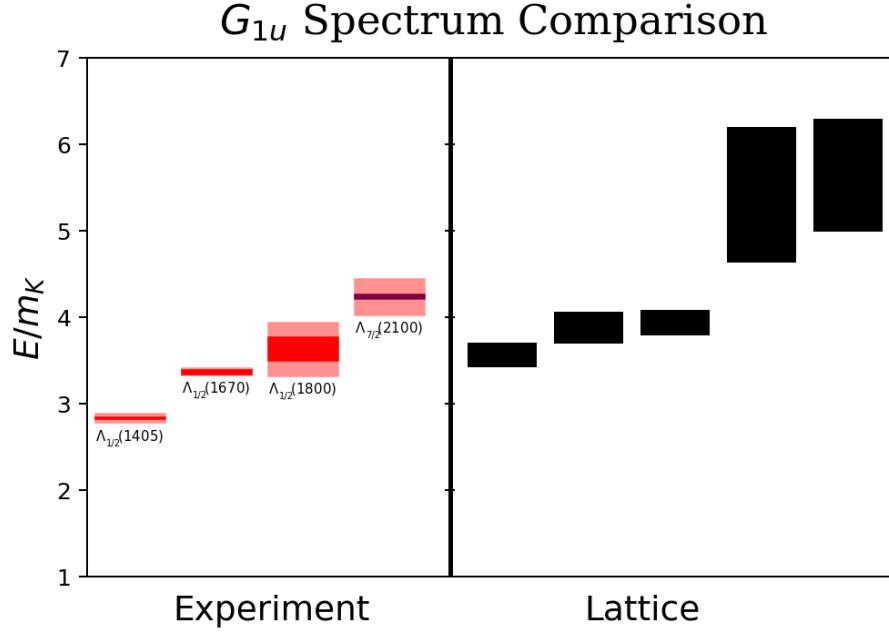


Figure 8.10: Experimentally observed resonances compared with our finite-volume single-hadron-dominated states. On the left, dark bands indicate experimental uncertainty, lighter bands indicate decay widths.

The  $G_{1u}$  spectrum of single-hadron-dominated states given in Figure 8.10 does not compare terribly well with the experimental spectrum. By comparing with the nucleon (which is made unphysically heavy) as a reference instead of the kaon (which is set to its physical mass) we can observe better agreement, shown in Figure 8.11.

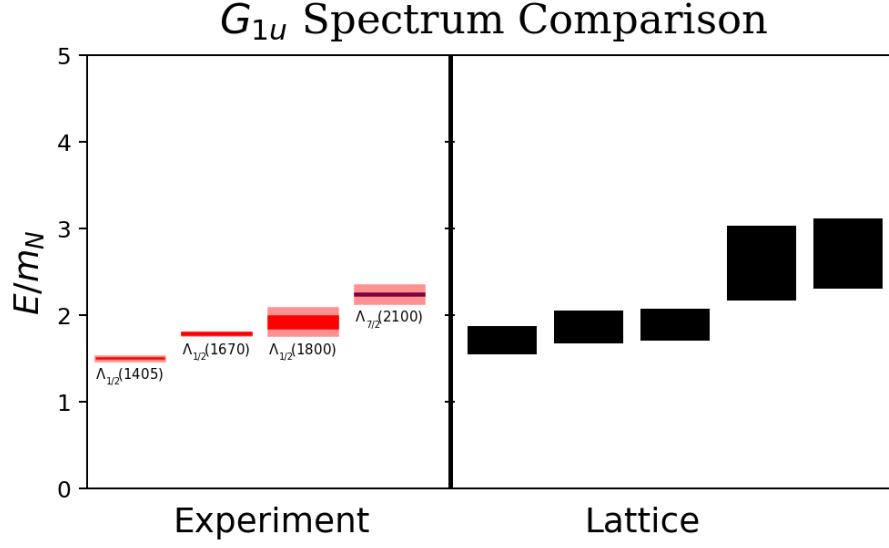


Figure 8.11: Experimentally observed resonances compared with our finite-volume single-hadron-dominated states. On the left, dark bands indicate experimental uncertainty, with lighter bands indicated decay widths.

The overall structure compares well to past results on  $\Lambda$  baryons [46], shown in Figure 8.12. We find that our lowest state corresponds roughly to the  $\Lambda(1405)$ , and lies in a closely-spaced group of three states. Additional resonances seem to lie above these, where we have neglected to include further two-particle operators. The qualitative reproduction of the  $\Lambda(1405)$  by a  $qqq$ -dominated state seems contradict recent results which suggest it is an antikaon-nucleon molecular state [47] [48]. In fact, this result seems to depend highly on the pion mass. The evidence for  $\bar{K}N$ -content is given in [47] and concerns the vanishing of the strange magnetic moment, and the evidence given in [48] concerns the structure of an effective Hamiltonian. In the former case, we can see from their plot, reproduced below as Figure 8.13, that these magnetic moments are sensitive to the pion mass and the conclusion applies to the *physical point*. Likewise, for unphysically heavy pions the effective Hamiltonian seems to require a bare three-quark state even though this seems unnecessary near the physical point.

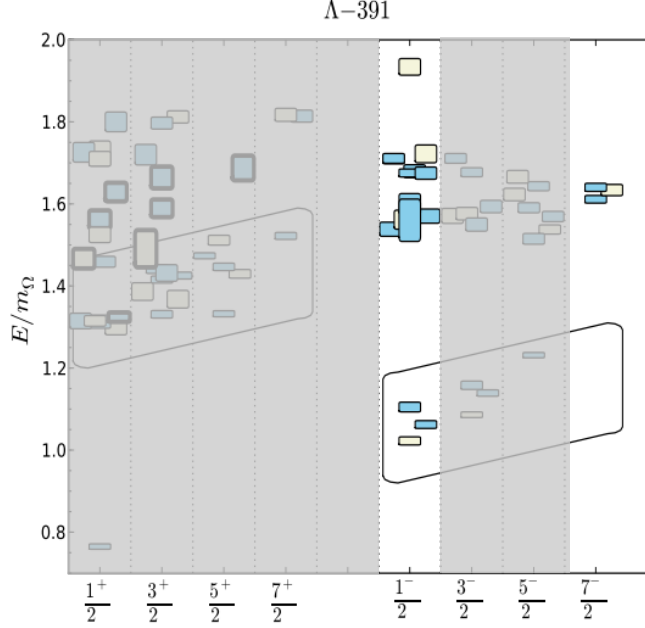


Figure 8.12: Observed baryonic states on a  $16^3$  lattice with a heavy 391 MeV pion [46]. The colors indicate  $SU(3)$ -flavor irrep, which we did not identify. Levels are labeled by  $J^P$ .

## 8.4 $H_g$ Spectrum on $32^3 \times 256$

The isosinglet strange  $H_g$  channel (at rest) is parity-plus and consists of spins  $\frac{3}{2}$ ,  $\frac{5}{2}$ ,  $\frac{7}{2}$ , and so on. It contains several resonances:  $\Lambda(1820)$  of spin  $\frac{5}{2}$ ,  $\Lambda(1890)$  of spin  $\frac{3}{2}$ ,  $\Lambda(2110)$  of spin  $\frac{5}{2}$ ,  $\Lambda(2350)$  of spin  $\frac{9}{2}$ .

The two-particle content consists of particular meson-baryon pairings. Remembering that our meson- and baryon-operators are labeled for flavor structure only, we see that the the following two-particle operators excite states in this channel:

$\Lambda\eta$	Isospin	$0 + 0$	Strangeness	$-1 + 0$	Spin	$\frac{1}{2} + 0$
$N\bar{K}$	Isospin	$\frac{1}{2} + \frac{1}{2}$	Strangeness	$0 - 1$	Spin	$\frac{1}{2} + 0$
$\Sigma\pi$	Isospin	$1 + 1$	Strangeness	$-1 + 0$	Spin	$\frac{1}{2} + 0$
$\Xi K$	Isospin	$\frac{1}{2} + \frac{1}{2}$	Strangeness	$-2 + 1$	Spin	$\frac{1}{2} + 0$

This is the same content as the  $G_{1g/u}$  channels, except that here the total spin must be supplemented by additional angular momentum to lie in the channel. Therefore, any two-particle operator with both particles at rest appears here must represent excited states rather than the ground state for which these operators are named. For

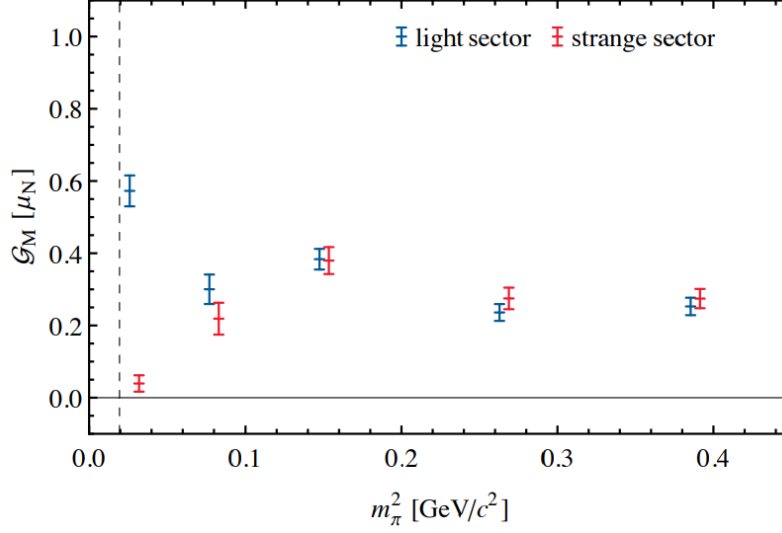


Figure 8.13: The light and strange quark contributions to the magnetic form factor of the  $\Lambda(1405)$  at  $Q^2 \approx 0.16 \text{ GeV}^2/c^2$  are presented as a function of the light quark masses, indicated by the squared pion mass,  $m_\pi^2$ . The vertical dashed line indicates the physical pion mass.

example,  $\pi[0]\Sigma[0]$  could not refer to the physical sigma, but rather the  $\Sigma(1670)$ . A list of some low-lying “expected” levels is given in Table 8.5.

In addition to the above two-particle operators, we also have the single-baryon operators. A large set of 12 operators was pruned down to just three, by removing noisy operators as well as operators found to be linearly dependent with others in the set. The final single hadron operators are:

$$\begin{aligned} \Lambda & H_g \quad \text{SD42} \\ \Lambda & H_g \quad \text{SS0} \\ \Lambda & H_g \quad \text{TDT134} \end{aligned}$$

As in the  $G_{1g}$  channel, these operators are pre-rotated, to find “optimized” single hadron operators, labeled as 0 through 2, to be used in the calculation of overlap factors.

For this channel, a diagonalization time of 7 and a metric time of 4 were found to be sufficient for off-diagonal elements to be consistent with zero. As with  $G_{1g}$ , operators were pruned such that the correlator matrix itself was not ill-conditioned, having no negative or zero eigenvalues.

We have preferred single-exponential fits for every level in this channel. These fits are displayed in Table 8.6. For reference, we also give the effective mass plots for each

meson	baryon	operators
$\bar{K}[1]$	$N[1]$	$A_2 \text{ SS1} - G_1 \text{ SS0}$
$\pi[1]$	$\Sigma[1]$	$A_2^- \text{ SS1} - G_1 \text{ SS0}$
$\bar{K}[2]$	$N[2]$	$A_2 \text{ SS0} - G_1 \text{ SS0}$
$\pi[2]$	$\Sigma[2]$	$A_2^- \text{ SS0} - G \text{ SS1}$
$\eta[1]$	$\Lambda[1]$	$A_2^+ \text{ SS1} - G_1 \text{ SS1}$
$\pi[1]$	$\Sigma(1385)[1]$	$A_2^- \text{ SS1} - G_2 \text{ SS0}$
		$A_2^- \text{ SS1} - G_1 \text{ SS0}$
$\bar{K}[3]$	$N[3]$	$A_2 \text{ SS0} - G \text{ SS0}$
$\pi[0]$	$\Sigma(1670)[0]$	$A_{1u}^- \text{ SS0} - H_u \text{ SS2}$
$\eta[2]$	$\Lambda[2]$	none
$\pi[3]$	$\Sigma[3]$	$A_2^- \text{ SS0} - G \text{ SS4}$
$\bar{K}^*(892)[1]$	$N[1]$	$E \text{ SS2} - G_1 \text{ SS0}$
$K[1]$	$\Xi[1]$	$A_2 \text{ SS1} - G_1 \text{ SS0}$

Table 8.5: Some expected two-hadron levels in the  $H_g$  channel. We list operators that might excite, or couple strongly to, each level.

level in Figure 8.14, though these are illustrative only and the effective mass points are not used in any fit.

Level	Time Range	$a_t E$	$\chi^2/\text{dof}$	content
0	(8, 22)	.364(13)	1.12	$\bar{K}[2] - N[2]$
1	(5, 20)	.3780(49)	2.57	$\bar{K}[1] - N[1]$
2	(8, 22)	.383(13)	1.50	$\bar{K}[1] - \Xi[1]$
3	(5, 15)	.3849(47)	1.23	$\pi[1] - \Sigma[1]$
4	(6, 22)	.3852(93)	1.60	$\pi[1] - \Sigma(1385)[1]$
5	(6, 22)	.3857(72)	1.18	$\bar{K}[3] - N[3]$
6	(6, 22)	.3883(83)	0.82	
7	(6, 22)	.3926(90)	1.71	$qqq$
8	(8, 22)	.397(17)	0.55	$\pi[0] - \Sigma(1670)[0]$
9	(8, 22)	.400(20)	0.99	$\bar{K}^*(892)[1] - N[1]$
10	(7, 20)	.402(31)	0.79	$\eta[1] - \Lambda[1]$
11	(6, 22)	.407(12)	0.83	$qqq$
12	(6, 20)	.415(10)	1.86	
13	(6, 20)	.452(14)	0.88	$\pi[3] - \Sigma[3]$

Table 8.6: Results of non-periodic exponential fits to the 14 diagonal entries of a diagonalized correlator in the  $H_g$  channel. Last column indicates an operator which overlaps maximally with a given level. All fits are single exponentials.

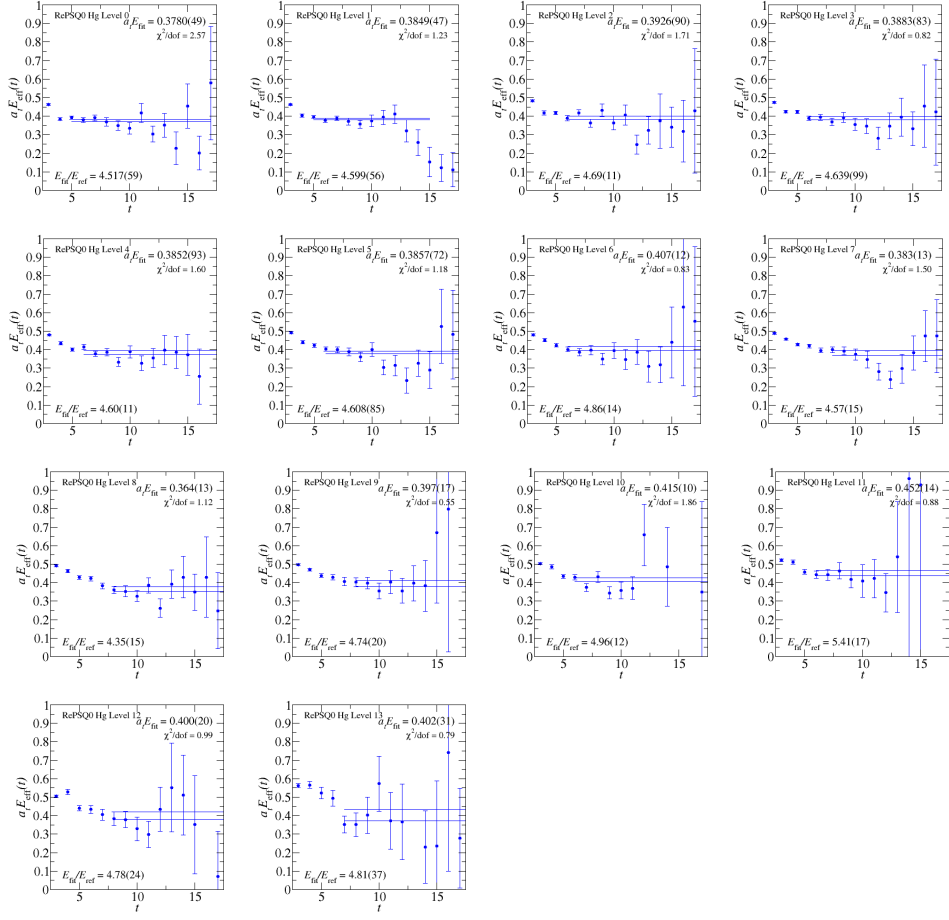


Figure 8.14: Effective energies of diagonal elements of a diagonalized correlator in the  $H_g$  channel. Horizontal lines display the upper and lower bounds for the final fit value. We use a time separation of  $\Delta t = 3$  in the discretized derivative.

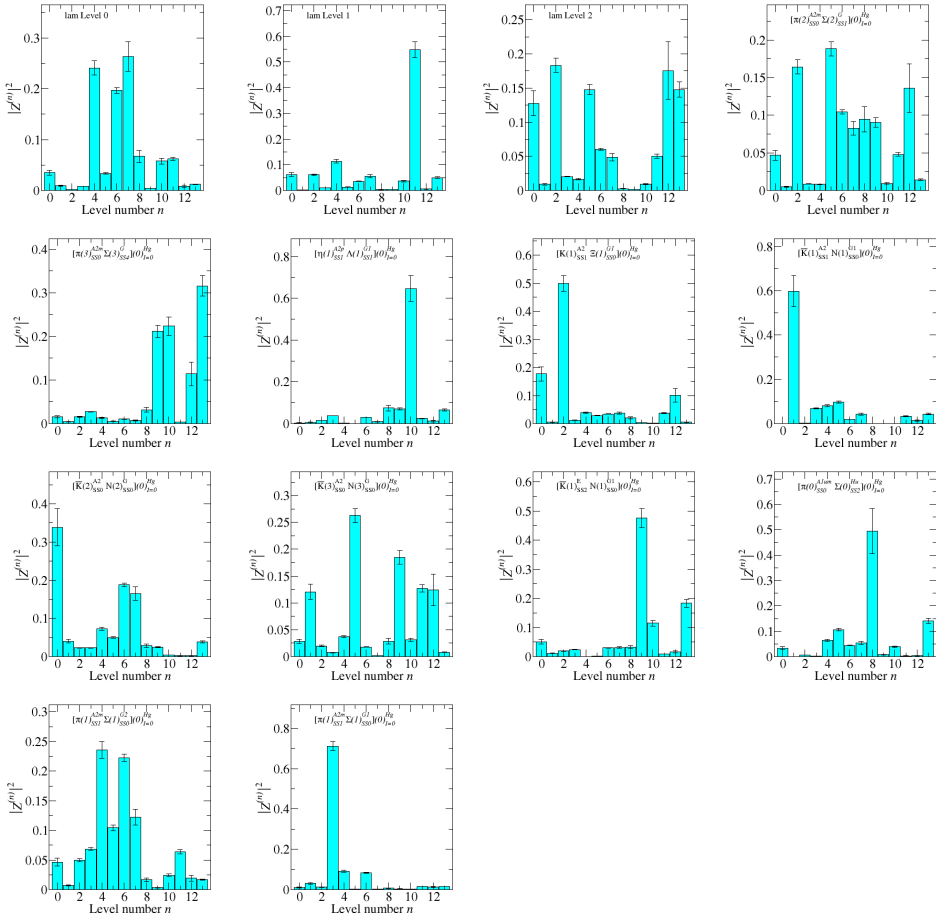


Figure 8.15: Overlap factors for each operator onto the extracted energy levels in the  $H_g$  channel. Each single hadron operator has been optimized by pre-diagonalizing in the single-hadron subspace. The maximum bar for each operator is used to identify the corresponding level. Bars within 75% of the maximum, for single hadrons, denote significant mixing.

As in  $G_{1g}$ , after fitting every level and finding the overlap factors, we can attempt an identification of the content of these states. Figure 8.15 contains the overlap factors for each operator, demonstrating to which state(s) a given operator predominately couples.

A summary of the spectrum is shown in Figure 8.16, colored in the same way as the  $G_{1g}$  spectrum. We again select  $qqq$ -dominated states to compare with experimental spectra. Because the highest few states are rarely reproduced well, we ignore these levels in the identification process. In the case of  $H_g$ , we ignore only the highest

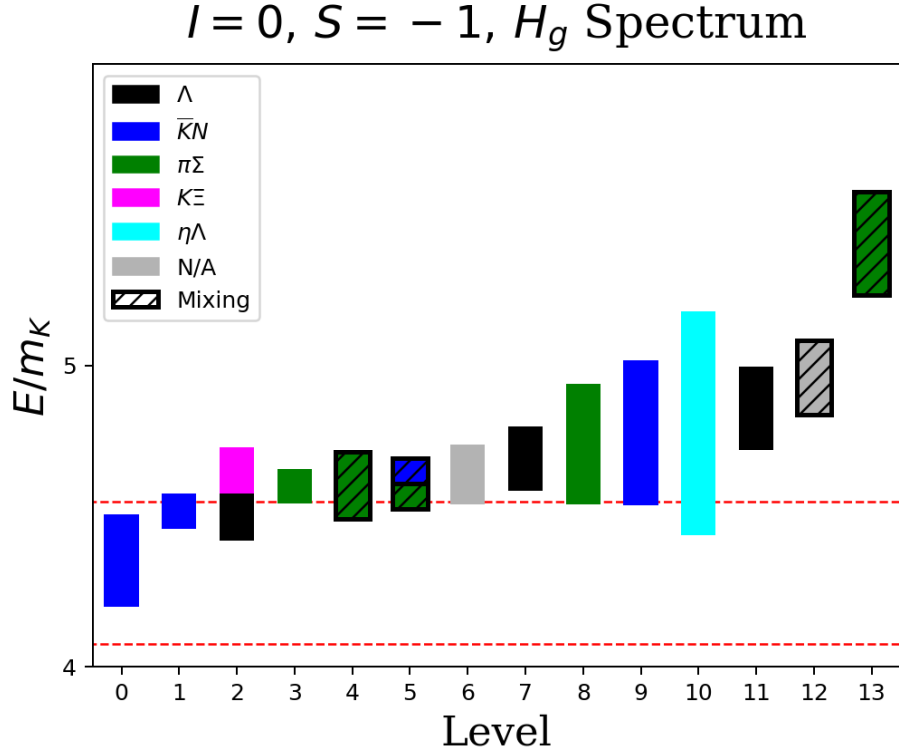


Figure 8.16: Full spectrum for isosinglet strange  $H_g$ . Levels colored by maximal overlaps, with large but non-maximal overlaps on single-hadron operators indicating significant mixing. Three ( $\bar{K}[1]N[1]\pi[0]$ ) and four ( $\bar{K}[1]N[1]\pi[0]\pi[0]$ ) particle thresholds are displayed.

single-hadron-dominated state.

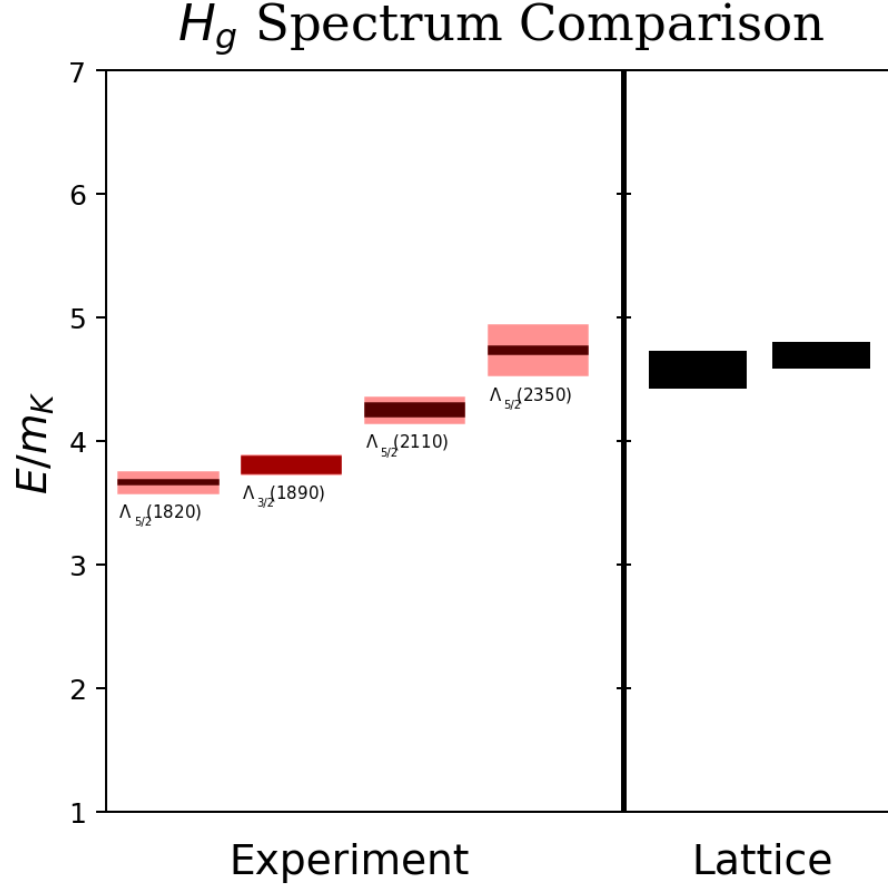


Figure 8.17: Experimentally observed resonances compared with our finite-volume single-hadron-dominated states. On the left, dark bands indicate experimental uncertainty, lighter bands indicate decay widths.

The  $H_g$  spectrum of single-hadron-dominated states given in Figure 8.17 does not compare terribly well with the experimental spectrum. By comparing with the nucleon (which is made unphysically heavy) as a reference instead of the kaon (which is set to its physical mass) we can observe better agreement, shown in Figure 8.18.

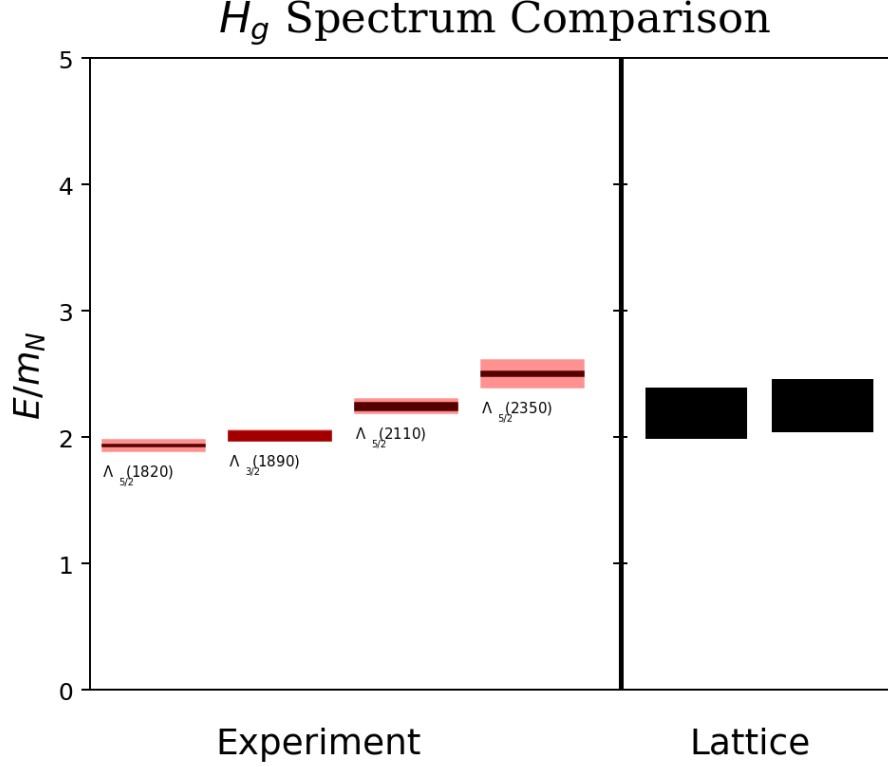


Figure 8.18: Experimentally observed resonances compared with our finite-volume single-hadron-dominated states. On the left, dark bands indicate experimental uncertainty, with lighter bands indicated decay widths.

Both our spectra in Figure 8.18 and previous lattice results in Figure 8.19 show a complete absence of very low-lying resonances, especially compared to other channels. The first resonances in this channel occur in the same energy regime as the multiply-excited resonances in the  $H_u$  channel, in Figures 8.24 and 8.25. We have extracted the lower-lying levels, and shown that they do not couple strongly to single hadron operators, with the first single-hadron-dominated state coming in at just above  $2m_N$ . We see fewer states, only two or three (if we include the highest single-hadron resonance, possibly reasonable in this case) compared to 8.19, but in every channel we have not gone high enough in energy to reliably extract states  $\approx 2.5 \text{ MeV}$ .

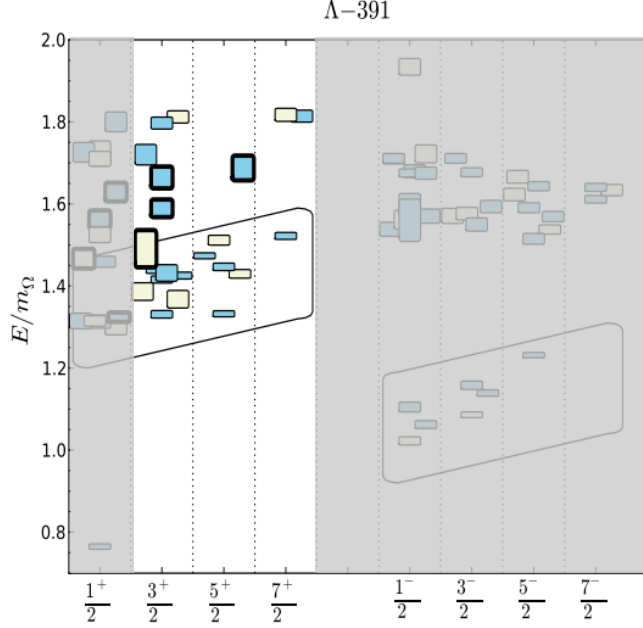


Figure 8.19: Observed baryonic states on a  $16^3$  lattice with a heavy 391 MeV pion [46]. The colors indicate  $SU(3)$ -flavor irrep, which we did not identify. Levels are labeled by  $J^P$ .

## 8.5 $H_u$ Spectrum on $32^3 \times 256$

The isosinglet strange  $H_u$  channel (at rest) is parity-minus and consists of spins  $\frac{3}{2}$ ,  $\frac{5}{2}$ ,  $\frac{7}{2}$ , and so on. It contains several resonances:  $\Lambda(1520)$  of spin  $\frac{3}{2}$ ,  $\Lambda(1690)$  of spin  $\frac{3}{2}$ ,  $\Lambda(1830)$  of spin  $\frac{5}{2}$  and  $\Lambda(2100)$  of spin  $\frac{7}{2}$ . A list of some low-lying “expected” levels is given in Table 8.7.

In addition to the above two-particle operators, we also have the single-baryon operators. A large set of 10 operators was pruned down to just five, by removing noisy operators as well as operators found to be linearly dependent with others in the set. The final single hadron operators are:

$\Lambda$	$H_u$	DDI16
$\Lambda$	$H_u$	DDL166
$\Lambda$	$H_u$	SD23
$\Lambda$	$H_u$	SD38
$\Lambda$	$H_u$	SS0

meson	baryon	operators
$K[1]$	$N[1]$	$A_2 \text{ SS1} - G_1 \text{ SS0}$
$\pi[0]$	$\Sigma(1385)[0]$	$A_{1u}^- \text{ SS0} - H_g \text{ SS0}$
$\pi[1]$	$\Sigma[1]$	$A_2 \text{ SS1} - G_1 \text{ SS2}$
$K[2]$	$N[2]$	$A_2 \text{ SS0} - G \text{ SS0}$
$\pi[2]$	$\Sigma[2]$	$A_2^- \text{ SS0} - G \text{ SS1}$
$\eta[1]$	$\Lambda[1]$	$A_2^+ \text{ SS0} - G_1 \text{ SS1}$
$\pi[1]$	$\Sigma(1385)[1]$	$A_2^- \text{ SS1} - G_1 \text{ SS2}$
		$A_2^- \text{ SS1} - G_2 \text{ SS0}$
$K^*(892)[0]$	$N[0]$	$T_{1u} \text{ SS1} - G_{1g} \text{ SS0}$
$K[3]$	$N[3]$	$A_2 \text{ SS0} - G \text{ SS0}$
$\omega(782)[0]$	$\Lambda[0]$	$T_{1u}^- \text{ SS0} - G_{1g} \text{ SS0}$
$\eta[2]$	$\Lambda[2]$	none
$\pi[3]$	$\Sigma[3]$	none
$K^*(892)[1]$	$N[1]$	$A_1 \text{ SS2} - G_1 \text{ SS0}$
$K[1]$	$\Xi[1]$	$A_2 \text{ SS1} - G_1 \text{ SS0}$
$K[4]$	$N[4]$	$A_2 \text{ SS1} - G_1 \text{ SS0}$

Table 8.7: Some expected two-hadron levels in the  $H_u$  channel. We list operators that might excite, or couple strongly to, each level.

As in the  $G_{1g}$  channel, these operators are pre-rotated, to find “optimized” single-hadron operators, labeled as 0 through 4, to be used in the calculation of overlap factors.

For this channel, a diagonalization time of 7 and a metric time of 4 were found to be sufficient for off-diagonal elements to be consistent with zero. As with  $G_{1g}$ , operators were pruned such that the correlator matrix itself was not ill-conditioned, having no negative or zero eigenvalues.

We have preferred single-exponential fits for every level in this channel. These fits are displayed in Table 8.8. For reference, we also give the effective mass plots for each level in Figure 8.20, though these are illustrative only and the effective mass points are not used in any fit.

Level	Time Range	$a_t E$	$\chi^2/\text{dof}$	content
0	(8, 22)	.328(18)	1.14	$\Lambda$
1	(8, 22)	.333(11)	1.57	$\bar{K}[1] - N[1]$
2	(8, 22)	.338(19)	1.29	
3	(8, 22)	.3400(73)	1.41	$\pi[0] - \Sigma(1385)[0]$
4	(8, 22)	.352(11)	1.04	
5	(8, 22)	.368(14)	1.85	
6	(8, 22)	.376(35)	0.85	$qqq$
7	(8, 22)	.383(14)	1.18	$\omega(782)[0] - \Lambda[0]$
8	(6, 22)	.385(18)	2.01	$\bar{K}[4] - N[4]$
9	(8, 22)	.389(15)	0.92	$qqq$
10	(5, 22)	.3905(76)	1.64	$\pi[1] - \Sigma[1]$
11	(6, 22)	.398(13)	0.74	
12	(7, 22)	.400(14)	1.60	$\bar{K}[2] - N[2]$
13	(7, 22)	.410(11)	1.95	$\bar{K}[1] - \Xi[1]$
14	(6, 22)	.420(12)	0.98	
15	(5, 12)	.450(16)	4.06	$\bar{K}^*(892)[0] - N[0]$
16	(5, 12)	.505(33)	3.12	$\bar{K}^*(892)[1] - N[1]$
17	(6, 15)	.575(59)	1.20	$\eta[1] - \Lambda[1]$

Table 8.8: Results of non-periodic exponential fits to the 18 diagonal entries of a diagonalized correlator in the  $H_u$  channel. Last column indicates an operator which overlaps maximally with a given level. All fits are single exponentials.

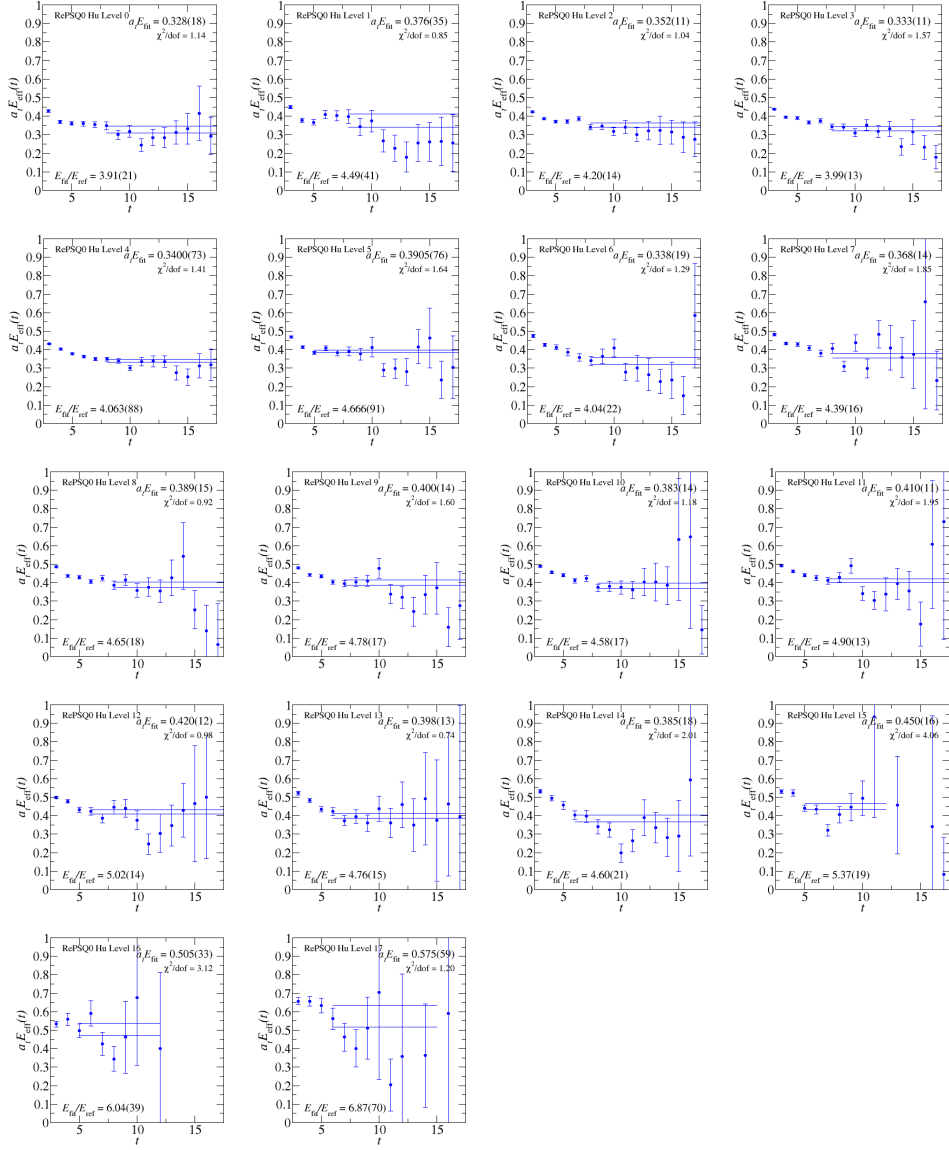


Figure 8.20: Effective energies of diagonal elements of a diagonalized correlator in the  $H_u$  channel. Horizontal lines display the upper and lower bounds for the final fit value. We use a time separation of  $\Delta t = 3$  in the discretized derivative.

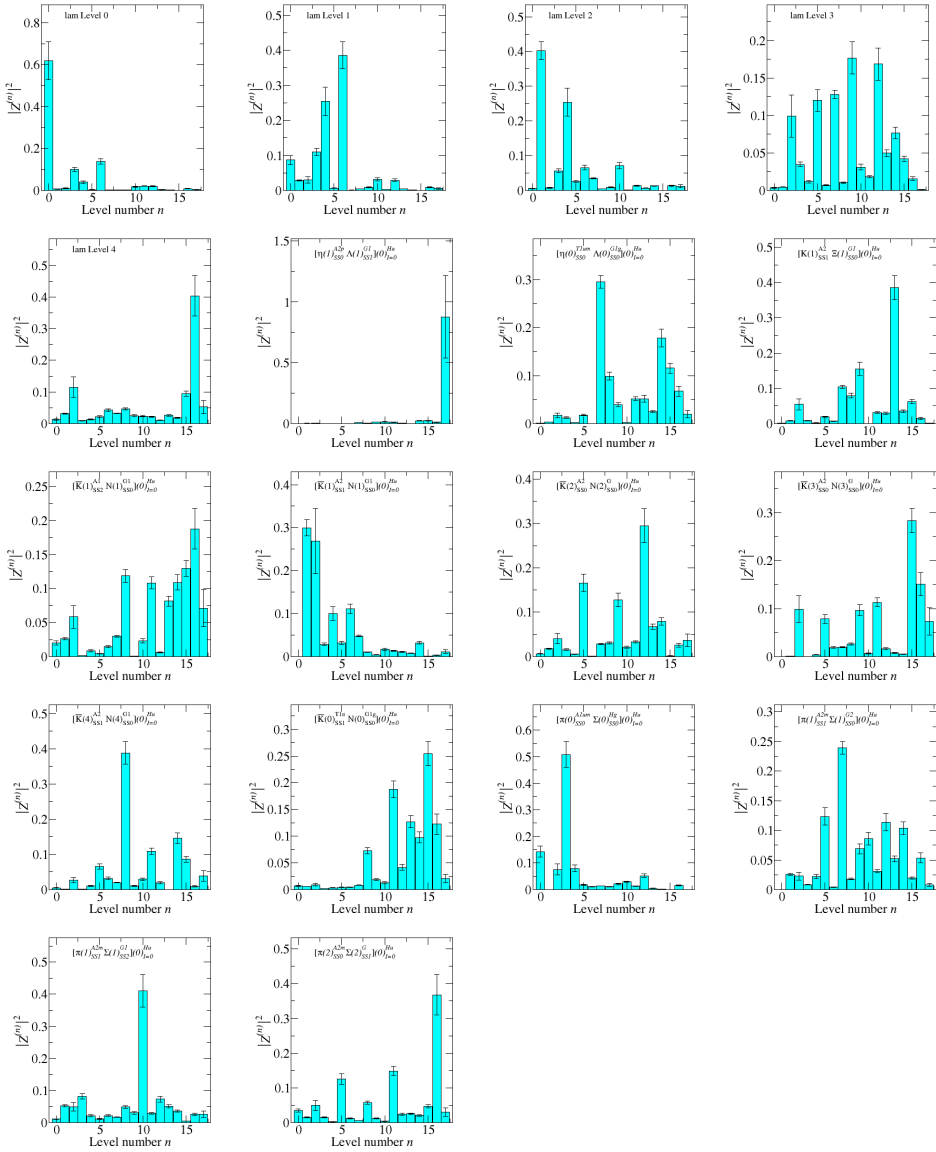


Figure 8.21: Overlap factors for each operator onto the extracted energy levels in the  $H_u$  channel. Each single hadron operator has been optimized by pre-diagonalizing in the single-hadron subspace. The maximum bar for each operator is used to identify the corresponding level. Bars within 75% of the maximum, for single hadrons, denote significant mixing.

As in  $G_{1g}$ , after fitting every level and finding the overlap factors, we can attempt an identification of the content of these states. Figure 8.21 contains the overlap factors for each operator, demonstrating to which state(s) a given operator predominately

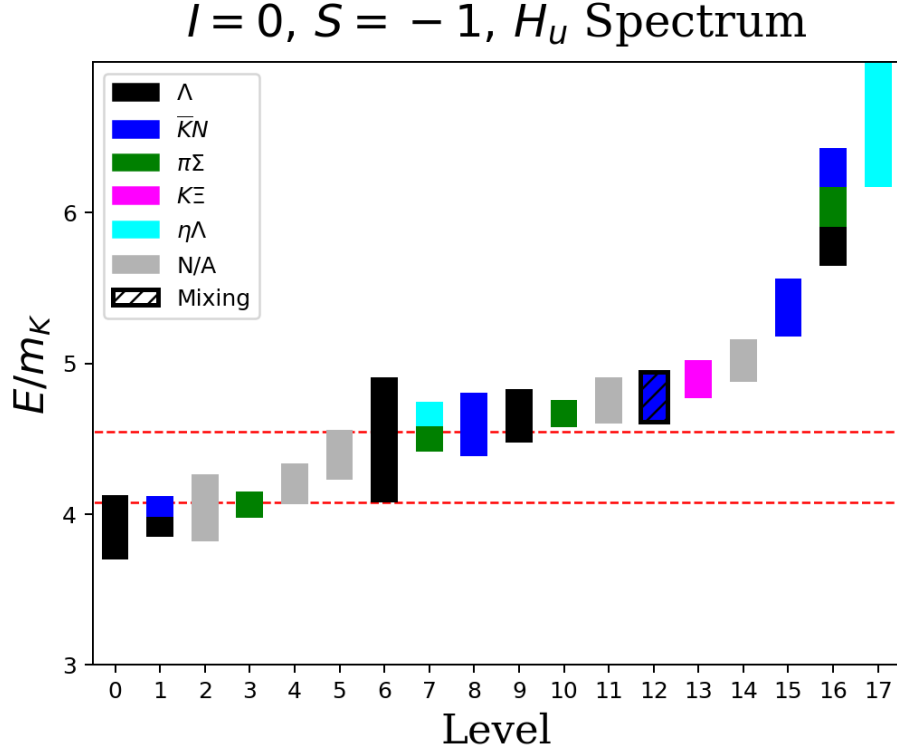


Figure 8.22: Full spectrum for isosinglet strange  $H_u$ . Levels colored by maximal overlaps, with large but non-maximal overlaps on single-hadron operators indicating significant mixing. Three ( $\bar{K}[1]N[1]\pi[0]$ ) and four ( $\bar{K}[1]N[1]\pi[0]\pi[0]$ ) particle thresholds are displayed.

couples.

A summary of the spectrum is shown in Figure 8.22, colored in the same way as the  $G_{1g}$  spectrum. We again select  $qqq$ -dominated states to compare with experimental spectra. Because the highest few states are rarely reproduced well, we ignore these levels in the identification process. In the case of  $H_u$ , we ignore only the highest single-hadron-dominated state.

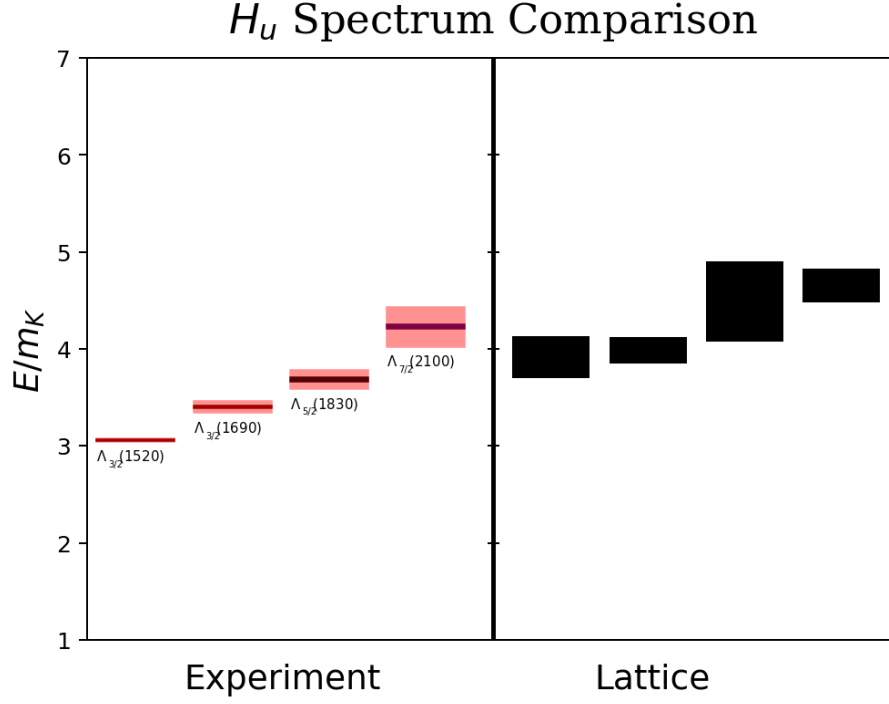


Figure 8.23: Experimentally observed resonances compared with our finite-volume single-hadron-dominated states. Dark bands indicate experimental uncertainty, lighter bands indicate decay widths.

The  $H_u$  spectrum of single-hadron-dominated states given in Figure 8.23 does not compare terribly well with the experimental spectrum. By comparing with the nucleon (which is made unphysically heavy) as a reference instead of the kaon (which is set to its physical mass) we can observe better agreement, shown in Figure 8.24.

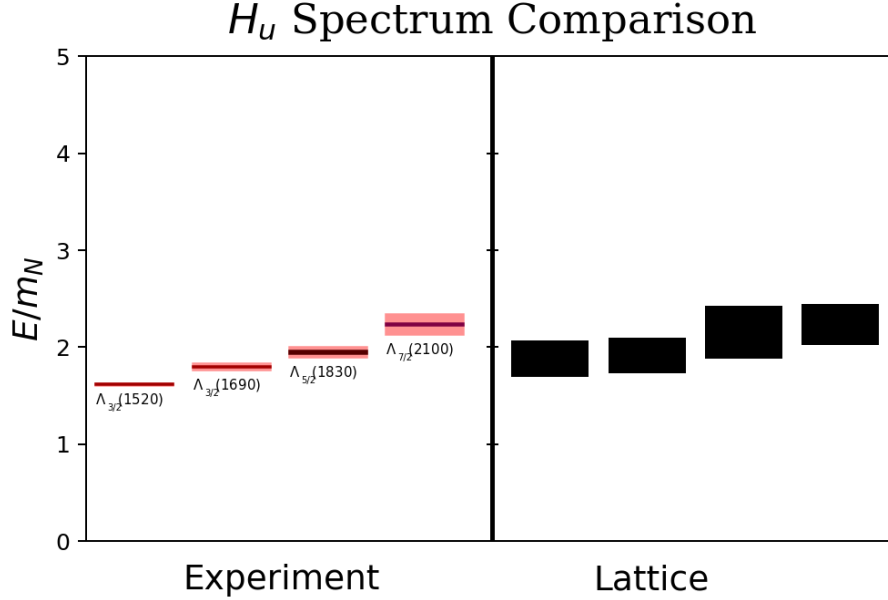


Figure 8.24: Experimentally observed resonances compared with our finite-volume single-hadron-dominated states. Dark bands indicate experimental uncertainty, with lighter bands indicated decay widths.

The overall structure compares well to past results on  $\Lambda$  baryons [46], shown in Figure 8.25. We have reproduced a group of four closely spaced levels at the bottom of the spectrum. However, the previous results indicate a larger spacing between the levels than we have observed; the experimental separation is much smaller as well. We remark that lowering the pion mass seems to have brought these levels closer together, and indeed closer to what is seen experimentally.

## 8.6 $\pi\pi$ Scattering Results

So far, we have identified  $\Lambda$ -resonances with finite-volume stationary-state energies. Such identifications are natural for QCD-stable particles, such as the long-lived  $\Lambda$ , but associating these stationary-states with unstable resonances, like the  $\Lambda(1405)$ , is problematic, preventing a precise correspondence. Fortunately, there is a method that relates finite-volume energies to scattering processes, in infinite volume. The Lüscher method is difficult to implement, especially for multiple decay channels and several partial waves. Before attempting the especially difficult task of applying this method

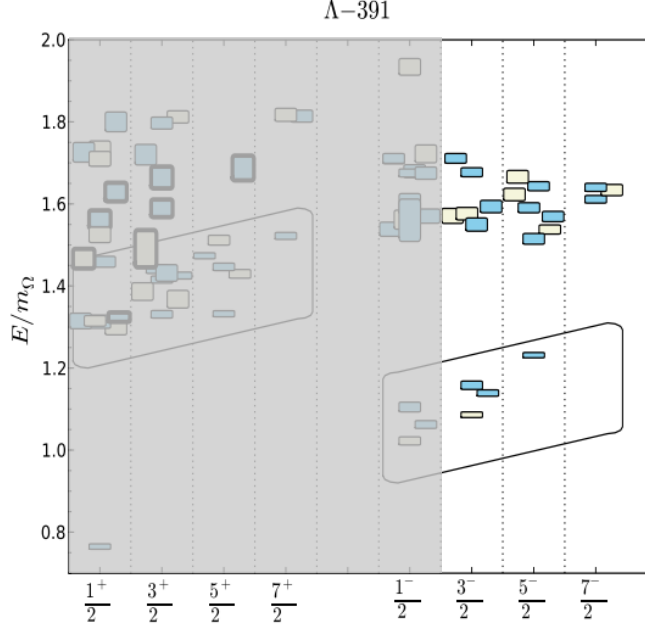


Figure 8.25: Observed baryonic states on a  $16^3$  lattice with a heavy 391 MeV pion [46]. The colors indicate  $SU(3)$ -flavor irrep, which we did not identify. Levels are labeled by  $J^P$ .

to  $\Lambda$  resonances, we first need to test it with a simpler system. Thus, we consider the decay of the rho meson to two pions. The goal is to show how the Luscher method can incorporate higher partial waves. Success for these mesons will lead to similar calculations for any baryonic resonance, whether above or below elastic thresholds and regardless of partial wave mixing.

The  $\rho(770)$  is seen as a resonance in  $\pi\pi$ -scattering, which at higher energies can mix with  $\bar{K}K$ . To simplify the analysis, we stay below the  $\bar{K}K$  threshold but this is not necessary for the formalism. In fact, the higher partial waves extracted for  $\pi\pi$  scattering,  $\ell = 1, 3$  and 5 are implemented in the same way as an additional  $\bar{K}K$  scattering channel. If we assume a single resonance in the  $P$ -wave and none in the  $L = 3$  or 5 partial waves, in our energy region, then the  $K$ -matrix is parametrized according to

$$K = \begin{pmatrix} (q_{\text{cm}})^3 \frac{1}{6\pi E} \frac{g_1^2}{E^2 - m_\rho^2} & 0 & 0 \\ 0 & \left(\frac{q_{\text{cm}}}{m_\pi}\right)^7 g_3^2 & 0 \\ 0 & 0 & \left(\frac{q_{\text{cm}}}{m_\pi}\right)^{11} g_5^2 \end{pmatrix}, \quad (8.1)$$

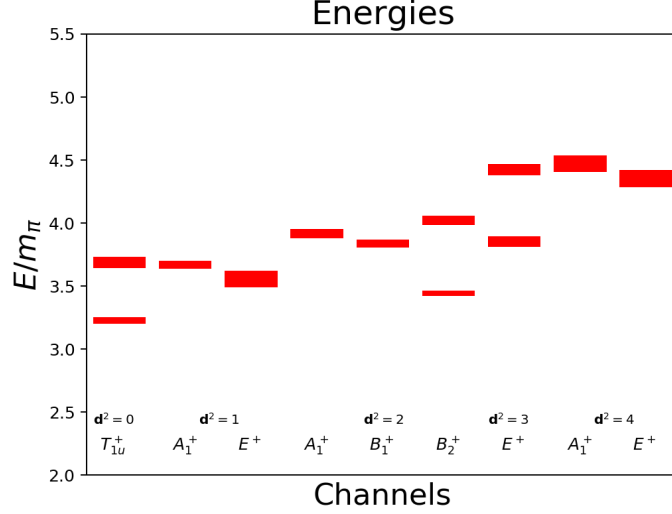


Figure 8.26: Lab energies of stationary states used for  $\pi\pi$  scattering.

where the resonance occurs near  $E = m_\rho$ . We use a coupling factor for the  $L = 3$  and 5 entries to allow for the possibility of additional partial waves. From the final fit values of the couplings  $g_3$  and  $g_5$ , we can show that these partial waves are negligible.

Because we are after the  $\rho(770)$ , we examine the  $T_{1u}^+$  isovector nonstrange channel. Boosting to nonzero total momenta, this subduces to  $A_1^+$ ,  $E^+$ ,  $B_1^+$  and  $B_2^+$ . The lowest few energies in each channel are used, and reported in Figure 8.26 and Table 8.9.

First, we perform fits utilizing a  $1 \times 1$   $K$ -matrix. Here the determinant condition  $\det(K^{-1} - B) = 0$  can be solved exactly, giving  $B = K^{-1}$ . We can plot  $B$ , and functions of  $B$ , for each energy, and various fits using our parametrization of  $K^{-1}$  give us the resonance parameters. For example, a plot of  $B$  features a zero at the resonance-mass, and features a slope roughly corresponding to its coupling factor, or width. In the case of the phase shift itself, the resonance-mass is where it rapidly precesses through  $\frac{\pi}{2}$  radians, while the width is related to the slope at this point. Plots of  $\cot\delta$ ,  $\delta$  and  $S$  display the typical resonance features, in Figures 8.27, 8.28 and 8.29, respectively.

We can solve the quantization condition to find  $B = K^{-1}$ , with  $B$  explicitly calculated in terms of our energies  $E$ , and parametrize  $K$  with

$$K = (q_{\text{cm}})^3 \frac{1}{6\pi E_{\text{cm}}} \frac{g^2}{E_{\text{cm}}^2 - m_\rho^2}. \quad (8.2)$$

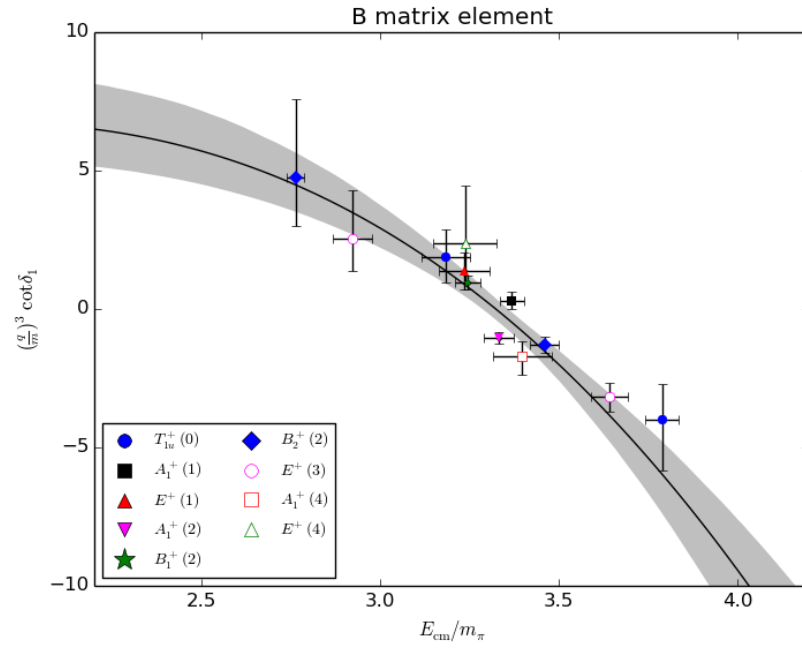


Figure 8.27: Plot of the  $B$ -matrix element times a normalization factor,  $(2\pi/m_\pi L)^3$ , assuming only the  $L = 1$  partial wave is present. With this assumption,  $B$  is proportional to  $q_{\text{cm}}^3 \cot \delta$ . The resonance location is where this plot crosses zero, with the width controlling the inverse of the slope. A higher decay width means a larger  $g$ , which makes the plot more shallow; a smaller decay width increases the curvature of this plot. Bands are  $\pm 85\%$  confidence intervals.

irrep	level	$\mathbf{d}^2$	$E_{\text{lab}}/m_\pi$	$\Delta E/m_\pi$	$E_{\text{cm}}/m_\pi$	$\mathbf{q}_{\text{cm}}^2/m_\pi^2$
$T_{1u}^+$	0	0	3.184(66)	-0.316(67)	3.184(66)	1.54(10)
$T_{1u}^+$	1	0	3.789(46)	0.289(46)	3.789(46)	2.590(86)
$A_1^+$	1	1	3.667(30)	-0.354(30)	3.369(33)	1.838(55)
$E^+$	0	1	3.545(63)	-0.477(64)	3.235(70)	1.62(11)
$A_1^+$	1	2	3.910(35)	-0.550(36)	3.331(41)	1.774(68)
$B_1^+$	0	2	3.837(28)	-0.623(30)	3.244(33)	1.632(53)
$B_2^+$	0	2	3.440(20)	-0.061(19)	2.763(25)	0.910(33)
$B_2^+$	1	2	4.021(33)	0.521(33)	3.460(38)	1.994(66)
$E^+$	0	3	3.851(42)	-0.170(42)	2.922(56)	1.136(80)
$E^+$	1	3	4.423(41)	0.401(41)	3.643(50)	2.318(91)
$A_1^+$	1	4	4.464(63)	0.395(63)	3.397(83)	1.89(14)
$E^+$	0	4	4.344(65)	0.275(67)	3.238(87)	1.62(14)

Table 8.9: Lab energies, interaction energies, and center-of-momentum-frame energies of stationary states used for  $\pi\pi$  scattering. We also display the constituent momenta for the center-of-momentum-frame two-particle states.

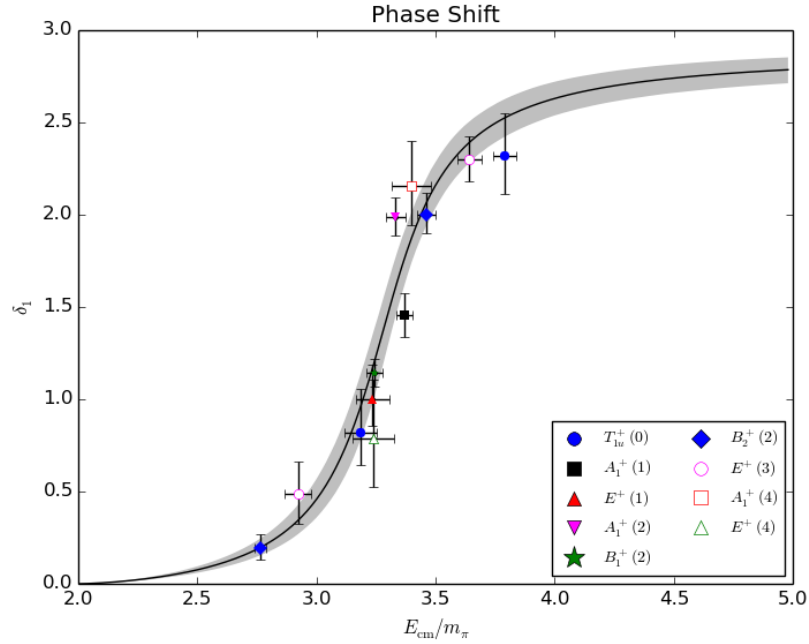


Figure 8.28: Plot of phase shift  $\delta_1$ , as determined by the  $B$ -matrix assuming only an  $L = 1$  partial wave. The resonance location is where this plot briefly shoots upward, with the width controlling the slope in this region. This displays the typical resonance phenomena of rapidly precessing through  $\pi$ . Bands are  $\pm 85\%$  confidence intervals.

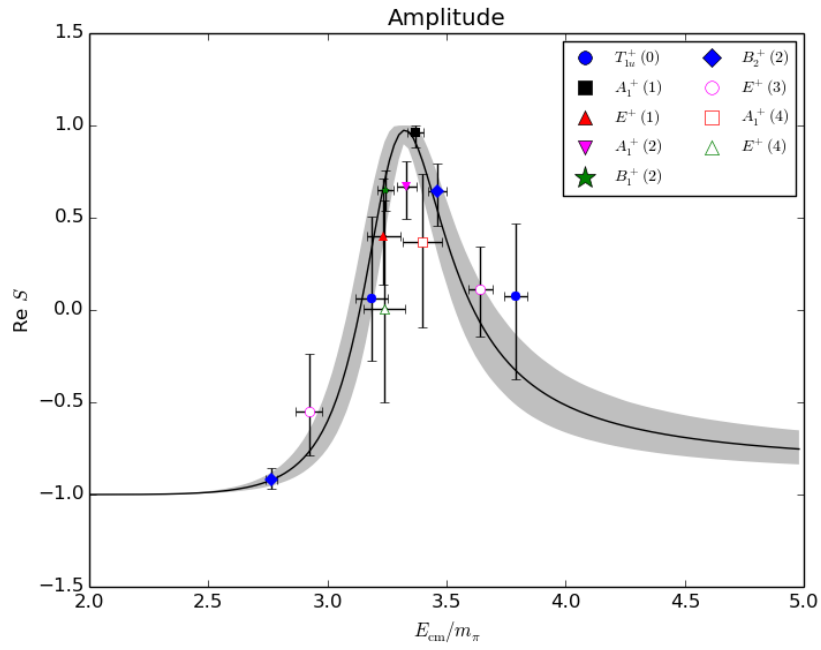


Figure 8.29: Plot of  $S$ -matrix  $e^{2i\delta_1}$ , as determined by the  $B$ -matrix assuming only an  $L = 1$  partial wave. The resonance location is where this plot peaks, with the width readily apparent. Purely finite-volume data can precisely predict a physical particle, necessarily in infinite-volume, in terms of a peaked cross-section — just like an experiment!

Performing the fit procedure detailed in [44], we find the values:

$$\frac{m_\rho}{m_\pi} = 3.323 \pm 0.027 \quad g = 6.35 \pm 0.49 \quad \chi^2/\text{dof} = 0.69 \quad (8.3)$$

which compares favorably to experiment. The resonance-mass-ratio we report is unphysical, thanks to the heavy pion, but the coupling we extract nearly agrees with the physical value of 6. The relationship between the parameter  $g$  and the actual decay width is given by

$$\Gamma = \frac{g_1^2}{48\pi} m_\rho \left[ 1 - \left( \frac{2m_\pi}{m_\rho} \right)^2 \right]^{\frac{3}{2}} \quad (8.4)$$

$$\frac{\Gamma}{m_\pi} = 0.439 \pm 0.093$$

and does not compare nearly as well as the  $g$ -coupling; the experimental  $\Gamma$  value is found to be about  $1.08 m_\pi$ . However, the decay width and resonance-mass are much closer to experimental values if we report them in units of the kaon instead, which might have interesting implications in chiral perturbation theory. Even after putting these in units of the kaon, the width is not expected to agree, given that the phase space of the decay is sensitive to the unphysical  $m_\pi$  value. The resonance value is also in line with the corresponding lattice state in  $T_{1u}^+$ , which reinforces the connection between these single-hadron dominated stationary states and the infinite-volume resonances.

By using a one-dimensional  $K$ -matrix we have neglected higher partial waves. We can use a larger matrix to include other phase shifts, but by doing so we trade one unknown,  $\delta$ , for more; because the quantization condition is only one equation, we cannot solve exactly for these additional phase shifts. We are forced to minimize the determinant condition with a parameterized  $K$ . So, for  $L = 3$  we use

$$K = \begin{pmatrix} (q_{\text{cm}})^3 \frac{1}{6\pi E_{\text{cm}}} \frac{g^2}{E_{\text{cm}}^2 - m_\rho^2} & 0 \\ 0 & \left( \frac{q_{\text{cm}}}{m_\pi} \right)^7 g_3^2 \end{pmatrix} \quad (8.5)$$

and minimize  $\Omega(\mu, K^{-1} - B)$ , defined in Equation 7.14.

The same process can be repeated, adding another row/column for  $L = 5$ . We

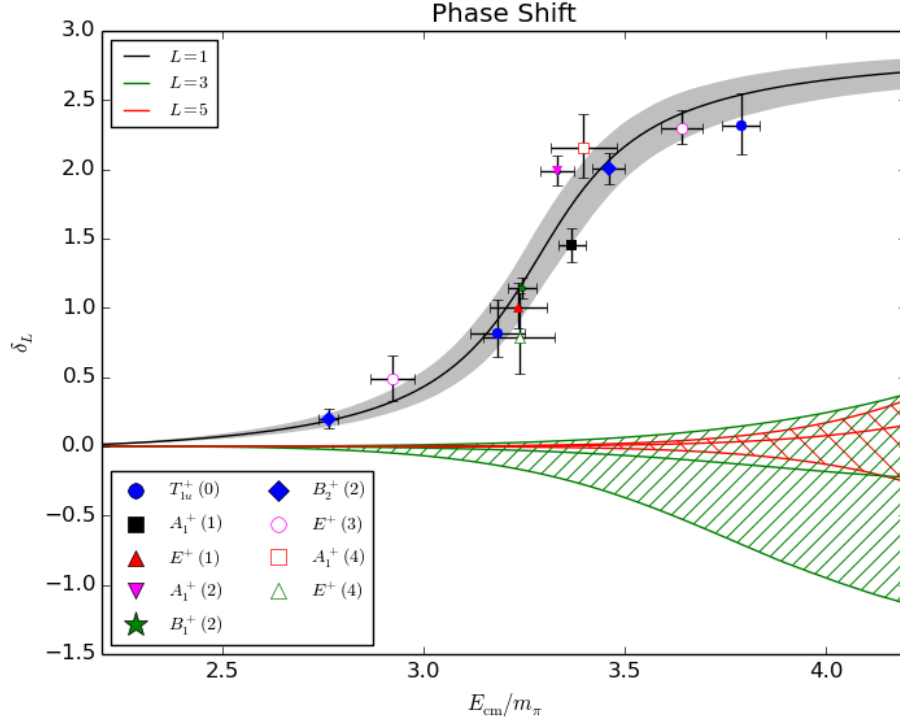


Figure 8.30: Plot of phase shift  $\delta_L$ , for  $L = 1, 3$  and  $5$ . The resonance location is where  $\delta_1$  briefly shoots upward, with the width controlling the slope in this region. This displays the typical resonance phenomena of rapidly precessing through  $\pi$ . Bands are  $\pm 85\%$  confidence intervals. Data points are identical to previous plots, curves are not fit to this data. Curve results come from fitting the quantization condition including  $L = 1, 3$  and  $5$  partial waves. However, we still see agreement.

parametrize with

$$K = \begin{pmatrix} (q_{\text{cm}})^3 \frac{1}{6\pi E_{\text{cm}}} \frac{g^2}{E_{\text{cm}}^2 - m_\rho^2} & 0 & 0 \\ 0 & \left(\frac{q_{\text{cm}}}{m_\pi}\right)^7 g_3^2 & 0 \\ 0 & 0 & \left(\frac{q_{\text{cm}}}{m_\pi}\right)^{11} g_5^2 \end{pmatrix} \quad (8.6)$$

and minimize  $\Omega(\mu, K^{-1} - B)$ . Doing this, we find our  $L = 1, 3$  results

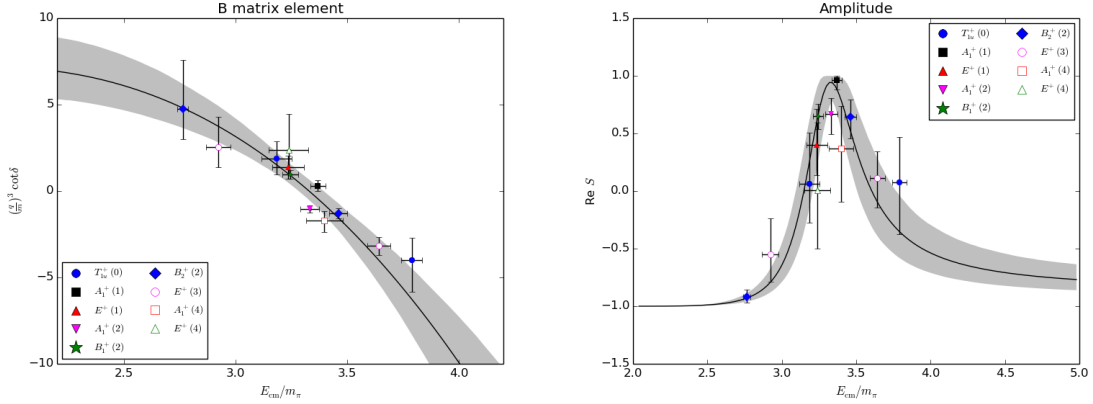


Figure 8.31: Plot of  $q^3 \cot \delta_1$  and the  $S$ -matrix element  $e^{2i\delta_1}$ , after minimizing  $\Omega$  including  $L = 1, 3$  and  $5$  partial waves. Data points are identical to previous plots, curves are not fit to this data. However, we still see agreement.

$$\begin{aligned}
 \frac{m_\rho}{m_\pi} &= 3.319 \pm 0.029 & g &= 6.09 \pm 0.48 \\
 g_3^2 &= -2.9 \pm 3.7 \times 10^{-3} & \chi^2/\text{dof} &= 0.62
 \end{aligned} \tag{8.7}$$

and the  $L = 1, 3, 5$  results

$$\begin{aligned}
 \frac{m_\rho}{m_\pi} &= 3.330 \pm 0.042 & g &= 6.20 \pm 0.60 \\
 g_3^2 &= 0.5 \pm 1.2 \times 10^{-3} \\
 g_5^2 &= -1.8 \pm 2.3 \times 10^{-4} \\
 \chi^2/\text{dof} &= 0.72.
 \end{aligned} \tag{8.8}$$

The phase shifts for the higher partial waves are consistent with zero, and the data points (extracted by neglecting higher partial waves) still compare well to our new  $L = 1$  parametrization (which includes these higher partial waves). That is, the grey bands of Figures 8.30 and 8.31 still agree well with the data from Figures 8.27, 8.28 and 8.29. The value of  $m_\rho$  is relatively insensitive to the different parametrizations. Technically, these results depend on the parametrization of the  $K$ -matrix; parametrization-dependent techniques are inescapable for resonances that lie near or above inelastic thresholds, as well as for non-negligible partial wave mixing.

The fit results are consistent with our published work [44] [43], and previous lat-

tice results compare relatively well [49] [50] [51]; previous works use different values for the light quark mass, and thus pion mass, so demanding agreement within  $1\sigma$  is less meaningful.

In spite of the rigorous justification that the lattice provides to quantum field theory, many quantities seem inaccessible. For example, the scattering and decay processes of a resonance seem to irreconcilable with the restrictions imposed by a Wick-rotated periodic finite box. Nonetheless, techniques have been developed and applied to extract true physical – meaning real-time, infinite volume – data from lattice calculations. We can apply the technique for particles of any spin, with and without partial-wave mixing, and above or below inelastic thresholds. The only caveat is that we have only included two-particle effects in the Bethe-Salpeter kernel<sup>1</sup>.

This work allows the first computation of the  $L = 5$  scattering phase shift for isovector  $\pi\pi$  scattering with a technique that generalizes to include multiple decay channels and arbitrary spins. This means, in particular, the technique should work well for baryon resonances on large lattices using noise dilution to achieve high precision.

---

<sup>1</sup>Work on including three-particles has been explored in [52] [53] [54]

# Chapter 9

## Conclusion

The spectra of three-quark excitations for four symmetry channels in the  $\Lambda$  baryon sector were studied using state-of-the-art lattice QCD techniques. As a step towards studying unstable resonances, we further developed a computational strategy that relates finite-volume energies to the  $S$ -matrix. This technology was tested using the  $\rho(770)$  decaying into two pions, incorporating the  $L = 1, 3$  and 5 partial waves for the first time. The main results are summarized in Figures 8.5, 8.11, 8.18, 8.24 and 8.30. All calculations are performed on a set of 412 gauge configurations of an anisotropic  $32^3 \times 256$  grid, at an unphysically heavy pion mass of  $\approx 240$  MeV using Wilson fermions.

In order to extract excited states on the lattice and relate them to infinite-volume resonances, it is crucial to use a large number of single- and multi-hadron operators. We detail the algorithmic procedure for creating a plethora of single- and multi-hadron operators for any symmetry sector, by using LapH-smearred covariantly displaced quark fields in chapter 4. These operators are used to define correlators which are evaluated using Monte Carlo methods, as detailed in chapter 5. Stochastic LapH with noise dilution, also discussed in chapter 5, is the critical ingredient enabling efficient evaluation of the quark lines in each correlator, in particular same-slice lines. The temporal fall-off of these correlators is related to the energy of various stationary states; the single-rotation method, discussed in chapter 6, can be used robustly for energy extraction, performing well despite the inherent noise of baryons.

In chapter 8 we applied these methods to four of the isosinglet strange baryon channels,  $G_{1g}, G_{1u}, H_g$  and  $H_u$ , which contain the  $\Lambda$  and some of its excitations. Around 20 operators for each channel were used to analyze the energy spectra, with

$qqq$ -dominated states identified via overlap factors onto optimized single-hadron operators. We expect these  $qqq$ -dominated states to become the actual resonance states as the volume increases. In this instance, the experimental comparisons are generally made better by reporting energies as a ratio of quantities that are affected by the unphysically heavy pion. The qualitative structure of these isosinglet strange baryons compares favorably, but not exactly, with similar calculations on smaller lattices with a heavier pion [46].

We also can relate the finite-volume energies to infinite-volume resonances using the Luscher method, discussed in chapter 7. In chapter 8 we demonstrate how this method can incorporate multiple partial waves, in the simple case of  $\pi\pi$  scattering. Our results demonstrate that the techniques we use to extract the mass and width of the  $\rho(770)$  should also work well for the study of baryonic resonances, such as the  $\Lambda(1405)$ .

Increasing computing power and improved Monte Carlo procedures have enabled lattice calculations on larger lattices at lower pion masses, making the experimental comparisons more direct. The techniques explored here allow us to connect these finite-volume spectra both qualitatively and quantitatively to infinite-volume resonances, with the ultimate goal of understanding the nature of these unstable particles.

# Bibliography

- [1] K. A. Olive *et al.*, “Review of Particle Physics,” *Chin. Phys.*, vol. C38, p. 090001, 2014.
- [2] D. J. Gross and F. Wilczek, “Ultraviolet behavior of non-abelian gauge theories,” *Phys. Rev. Lett.*, vol. 30, pp. 1343–1346, Jun 1973.
- [3] H. D. Politzer, “Reliable perturbative results for strong interactions?,” *Phys. Rev. Lett.*, vol. 30, pp. 1346–1349, Jun 1973.
- [4] M. G. Alford, T. Klassen, and P. Lepage, “The D234 action for light quarks,” *Nucl. Phys. Proc. Suppl.*, vol. 47, pp. 370–373, 1996.
- [5] C. Morningstar, J. Bulava, J. Foley, K. J. Juge, D. Lenkner, M. Peardon, and C. H. Wong, “Improved stochastic estimation of quark propagation with laplacian heaviside smearing in lattice qcd,” *Phys. Rev. D*, vol. 83, p. 114505, Jun 2011.
- [6] H. Fritzsch, M. Gell-Mann, and H. Leutwyler, “Advantages of the Color Octet Gluon Picture,” *Phys. Lett.*, vol. 47B, pp. 365–368, 1973.
- [7] M. Gell-Mann, “A Schematic Model of Baryons and Mesons,” *Phys. Lett.*, vol. 8, pp. 214–215, 1964.
- [8] G. Zweig, “An SU(3) model for strong interaction symmetry and its breaking. Version 1,” 1964.
- [9] M. Lüscher, “Volume dependence of the energy spectrum in massive quantum field theories,” *Communications in Mathematical Physics*, vol. 105, pp. 153–188, Jun 1986.

- [10] M. Lüscher, “Volume dependence of the energy spectrum in massive quantum field theories,” *Communications in Mathematical Physics*, vol. 104, pp. 177–206, Jun 1986.
- [11] M. Luscher, “Two particle states on a torus and their relation to the scattering matrix,” *Nucl. Phys.*, vol. B354, pp. 531–578, 1991.
- [12] K. Wilson, “Confinement of Quarks,” *Physical Review D*, vol. 10, 1974.
- [13] T. Reisz, “Lattice Gauge Theory: Renormalization to All Orders in the Loop Expansion,” *Nuclear Physics B*, vol. 318, 1989.
- [14] K. G. Wilson, *Quarks and Strings on a Lattice*, pp. 69–142. Boston, MA: Springer US, 1977.
- [15] H. B. Nielsen, “A no-go theorem for regularizing chiral fermions,” *Phys. Lett. B*, vol. 105, 1981.
- [16] L. H. Karsten and J. Smit, “Lattice Fermions: Species Doubling, Chiral Invariance, and the Triangle Anomaly,” *Nucl. Phys.*, vol. B183, p. 103, 1981. [,495(1980)].
- [17] K. Symanzik, “Continuum Limit and Improved Action in Lattice Theories: 1. Principles and  $\phi^4$  Theory,” *Nuclear Physics B*, vol. B226, 1983.
- [18] B. Sheikholeslami and R. Wohlert, “Improved continuum limit lattice action for qcd with wilson fermions,” *Nuclear Physics B*, vol. 259, no. 4, pp. 572 – 596, 1985.
- [19] T. DeGrand, A. Hasenfratz, and T. G. Kovács, “Improving the chiral properties of lattice fermions,” *Phys. Rev. D*, vol. 67, p. 054501, Mar 2003.
- [20] M. Luscher and P. Weisz, “On-Shell Improved Lattice Gauge Theories,” *Communications in Mathematical Physics*, vol. 97, 1985.
- [21] G. P. Lepage and P. B. Mackenzie, “On the viability of lattice perturbation theory,” *Phys. Rev.*, vol. D48, 1993.
- [22] R. G. Edwards, B. Joo, and H.-W. Lin, “Tuning for three flavors of anisotropic clover fermions with stout-link smearing,” *Phys. Rev. D*, vol. 78, 2008.

- [23] C. Morningstar and M. Peardon, “Analytic smearing of SU(3) link variables in lattice qcd,” *Phys. Rev. D*, vol. 69, p. 054501, Mar 2004.
- [24] H. S. Collab, “First results from 2+1 dynamical quark flavors on an anisotropic lattice: Light-hadron spectroscopy and setting the strange-quark mass,” *Phys. Rev. D*, vol. 79, 2009.
- [25] C. J. Morningstar and M. Peardon, “Glueball spectrum from an anisotropic lattice study,” *Phys. Rev. D*, vol. 60, p. 034509, Jul 1999.
- [26] S. Basak, R. G. Edwards, G. T. Fleming, U. M. Heller, C. Morningstar, D. Richards, I. Sato, and S. Wallace, “Group-theoretical construction of extended baryon operators in lattice qcd,” *Phys. Rev. D*, vol. 72, p. 094506, Nov 2005.
- [27] M. Peardon, J. Bulava, J. Foley, C. Morningstar, J. Dudek, R. G. Edwards, B. Joó, H.-W. Lin, D. G. Richards, and K. J. Juge, “Novel quark-field creation operator construction for hadronic physics in lattice qcd,” *Phys. Rev. D*, vol. 80, p. 054506, Sep 2009.
- [28] C. Morningstar, B. Fahy, Y.-C. Jhang, K. J. Juge, D. Lenkner, and C. H. Wong, “Excited isovector mesons using the stochastic LapH method,” *PoS*, vol. LATTICE2014, p. 101, 2014.
- [29] W. Weinberg, *The Quantum Theory of Fields: Foundations*. Cambridge University Press, 1995.
- [30] C. Morningstar, “The Monte Carlo method in quantum field theory,” 2007.
- [31] W. Hastings, “Monte carlo sampling methods using markov chains and their applications,” *Biometrika*, vol. 57, 1970.
- [32] M. Creutz, “Monte Carlo Study of Quantized SU(2) Gauge Theory,” *Phys. Rev.*, vol. D21, pp. 2308–2315, 1980.
- [33] S. L. Adler, “An Overrelaxation Method for the Monte Carlo Evaluation of the Partition Function for Multiquadratic Actions,” *Phys. Rev.*, vol. D23, p. 2901, 1981.

- [34] S. Duane, A. Kennedy, B. J. Pendleton, and D. Roweth, “Hybrid monte carlo,” *Physics Letters B*, vol. 195, no. 2, pp. 216 – 222, 1987.
- [35] R. Morrin, A. Ó Cais, M. Peardon, S. M. Ryan, and J.-I. Skullerud, “Dynamical qcd simulations on anisotropic lattices,” *Phys. Rev. D*, vol. 74, p. 014505, Jul 2006.
- [36] M. Clark, “The Rational Hybrid Monte Carlo Algorithm,” 2006.
- [37] L. Maiani and M. Testa, “Final state interactions from euclidean correlation functions,” *Physics Letters B*, vol. 245, no. 3, pp. 585 – 590, 1990.
- [38] K. Rummukainen and S. Gottlieb, “Resonance scattering phase shifts on a non-rest-frame lattice,” *Nuclear Physics B*, vol. 450, no. 1, pp. 397 – 436, 1995.
- [39] Z. Fu, “Rummukainen-gottlieb formula on a two-particle system with different masses,” *Phys. Rev. D*, vol. 85, p. 014506, Jan 2012.
- [40] R. A. Briceño, “Two-particle multichannel systems in a finite volume with arbitrary spin,” *Phys. Rev. D*, vol. 89, p. 074507, Apr 2014.
- [41] C. Kim, C. Sachrajda, and S. R. Sharpe, “Finite-volume effects for two-hadron states in moving frames,” *Nuclear Physics B*, vol. 727, no. 1, pp. 218 – 243, 2005.
- [42] M. T. Hansen and S. R. Sharpe, “Multiple-channel generalization of lellouch-lüscher formula,” *Phys. Rev. D*, vol. 86, p. 016007, Jul 2012.
- [43] J. Bulava, B. Fahy, B. Hrz, K. J. Juge, C. Morningstar, and C. H. Wong, “ $I=1$  and  $i=2$  scattering phase shifts from nf=2+1 lattice qcd,” *Nuclear Physics B*, vol. 910, pp. 842 – 867, 2016.
- [44] C. Morningstar, J. Bulava, B. Singha, R. Brett, J. Fallica, A. Hanlon, and B. Hrz, “Estimating the two-particle  $K$ -matrix for multiple partial waves and decay channels from finite-volume energies,” 2017.
- [45] R. G. Edwards and B. Jo, “The chroma software system for lattice qcd,” *Nuclear Physics B - Proceedings Supplements*, vol. 140, pp. 832 – 834, 2005. LATTICE 2004.

- [46] R. G. Edwards, N. Mathur, D. G. Richards, and S. J. Wallace, “Flavor structure of the excited baryon spectra from lattice QCD,” *Phys. Rev.*, vol. D87, no. 5, p. 054506, 2013.
- [47] J. M. M. Hall, W. Kamleh, D. B. Leinweber, B. J. Menadue, B. J. Owen, A. W. Thomas, and R. D. Young, “Lattice QCD Evidence that the (1405) Resonance is an Antikaon-Nucleon Molecule,” *Phys. Rev. Lett.*, vol. 114, no. 13, p. 132002, 2015.
- [48] Z.-W. Liu, J. M. M. Hall, D. B. Leinweber, A. W. Thomas, and J.-J. Wu, “Structure of the  $\Lambda(1405)$  from Hamiltonian effective field theory,” *Phys. Rev.*, vol. D95, no. 1, p. 014506, 2017.
- [49] C. B. Lang, D. Mohler, S. Prelovsek, and M. Vidmar, “Coupled channel analysis of the  $\rho$  meson decay in lattice qcd,” *Phys. Rev. D*, vol. 84, p. 054503, Sep 2011.
- [50] J. J. Dudek, R. G. Edwards, and C. E. Thomas, “Energy dependence of the  $\rho$  resonance in  $\pi\pi$  elastic scattering from lattice qcd,” *Phys. Rev. D*, vol. 87, p. 034505, Feb 2013.
- [51] X. Feng, K. Jansen, and D. B. Renner, “Resonance parameters of the  $\rho$  meson from lattice qcd,” *Phys. Rev. D*, vol. 83, p. 094505, May 2011.
- [52] M. T. Hansen and S. R. Sharpe, “Relativistic, model-independent, three-particle quantization condition,” *PoS*, vol. LATTICE2013, p. 221, 2014.
- [53] P. Guo, “The three-particle system on a torus,” 2013.
- [54] K. Polejaeva and A. Rusetsky, “Three particles in a finite volume,” *The European Physical Journal A*, vol. 48, p. 67, May 2012.
- [55] C. Gattringer and C. Lang, *Quantum Chromodynamics on the Lattice: An Introductory Presentation*. Springer, 2010.
- [56] A. Wipf, *Statistical Approach to Quantum Field Theory: An Introduction*. Springer, 2013.
- [57] A. Wightman, “Quantum Field Theory in terms of Vacuum Expectation Values,” *Physical Review*, vol. 101, 1956.

- [58] J. E. Kim and G. Carosi, “Axions and the Strong CP Problem,” *Rev. Mod. Phys.*, vol. 82, 2010.
- [59] J. Foley, K. J. Juge, A. . Cais, M. Peardon, S. M. Ryan, and J.-I. Skullerud, “Practical all-to-all propagators for lattice qcd,” *Computer Physics Communications*, vol. 172, no. 3, pp. 145 – 162, 2005.
- [60] J. Foley, C. H. Wong, J. Bulava, K. J. Juge, D. Lenkner, C. Morningstar, and M. Peardon, “A novel method for evaluating correlation functions in lattice hadron spectroscopy,” *PoS*, vol. Lattice2010, p. 098, 2014.
- [61] C. Pelissier and A. Alexandru, “Resonance parameters of the rho-meson from asymmetrical lattices,” *Phys. Rev. D*, vol. 87, p. 014503, Jan 2013.
- [62] F. James and M. Roos, “Minuit - a system for function minimization and analysis of the parameter errors and correlations,” *Computer Physics Communications*, vol. 10, no. 6, pp. 343 – 367, 1975.
- [63] Z. Davoudi and M. J. Savage, “Improving the volume dependence of two-body binding energies calculated with lattice qcd,” *Phys. Rev. D*, vol. 84, p. 114502, Dec 2011.
- [64] A. Reifman, B. S. DeWitt, and R. G. Newton, “Relations between bound-state problems and scattering theory,” *Phys. Rev.*, vol. 101, pp. 877–879, Jan 1956.